SENSITIVITY IMPROVEMENT STRATEGIES AND APPLICATIONS FOR
FLEXIBLE AND WEARABLE CAPACITIVE PRESSURE SENSORS

A THESIS SUBMITTED TO
THE GRADUATE SCHOOL OF NATURAL AND APPLIED SCIENCES
OF
MIDDLE EAST TECHNICAL UNIVERSITY

BY

MELİH ÖGEDAY ÇİÇEK

IN PARTIAL FULFILLMENT OF THE REQUIREMENTS
FOR
THE DEGREE OF MASTER OF SCIENCE
IN
METALLURGICAL AND MATERIALS ENGINEERING

AUGUST 2022

Approval of the thesis:

**SENSITIVITY IMPROVEMENT STRATEGIES AND APPLICATIONS
FOR FLEXIBLE AND WEARABLE CAPACITIVE PRESSURE SENSORS**

submitted by **MELİH ÖGEDAY ÇİÇEK** in partial fulfillment of the requirements
for the degree of **Master of Science** in **Metallurgical and Materials Engineering,
Middle East Technical University** by,

Prof. Dr. Halil Kalıpçılar
Dean, Graduate School of **Natural and Applied Sciences**   _____

Prof. Dr. Ali Kalkınlı
Head of the Department, **Metallurgical and Materials Eng.**   _____

Prof. Dr. Hüsnü Emrah Ünalan
Supervisor, **Metallurgical and Materials Eng., METU**   _____

Assoc. Prof. Dr. Simge Çınar Aygün
Co-Supervisor, **Metallurgical and Materials Eng., METU**   _____

Examining Committee Members:

Assist. Prof. Dr. Murat Perit Çakır
Department of Cognitive Science, METU   _____

Prof Dr. Hüsnü Emrah Ünalan
Metallurgical and Materials Eng., METU   _____

Assoc. Prof. Dr. Simge Çınar Aygün
Metallurgical and Materials Eng., METU   _____

Assist. Prof. Dr. Yusuf Keleştemur
Metallurgical and Materials Eng., METU   _____

Assist. Prof. Dr. Emre Ozan Polat
Mechatronic Eng., Kadir Has University   _____

Date: 23.08.2022

I hereby declare that all information in this document has been obtained and presented in accordance with academic rules and ethical conduct. I also declare that, as required by these rules and conduct, I have fully cited and referenced all material and results that are not original to this work.

Name Last name :

Signature :

ABSTRACT

SENSITIVITY IMPROVEMENT STRATEGIES AND APPLICATIONS FOR FLEXIBLE AND WEARABLE CAPACITIVE PRESSURE SENSORS

Çiçek, Melih Ögeday
Master of Science, Metallurgical and Materials Engineering
Supervisor : Prof. Dr. Hüsnü Emrah Ünalan
Co-Supervisor: Assist. Prof. Dr. Simge Çınar Aygün

August 2022, 109 pages

Pressure sensors have attracted great interest in parallel with developments in wearable electronics, robotics, human-machine interface devices, and electronic skin. In this field, capacitive pressure sensors are gaining increasing research attention due to their high sensitivity, high stability, fast response/recovery times, and simple manufacturing routes. While capacitive pressure sensors have prominent features, there is still a long way to go before they become more common in wearable technology. Increasing the sensitivity of today's capacitive pressure sensors is one of the most critical priorities in this field.

In the first chapter of this work, sensitivities of the capacitive pressure sensors were improved by employing facile fabrication methods and rational sensor designs. In that regard, the first part of the thesis proposes a low-cost, lightweight, parallel plate capacitive sensor with a unique monolithic design. This design allows the sensors to significantly improve their sensitivity. The monolithic capacitive sensor (MCS) with a density of as low as 10.78 mg/cm^3 was fabricated using 3-D masking technique on a commercially available melamine sponge with silver nanowire electrodes and a protective thin layer of polydimethylsiloxane coating. In addition to its unique design, the MCSs showed high sensitivity (up to 1.28 kPa^{-1}), fast response/recovery

time (18 ms/54 ms), very low-pressure sensing ability (0.5 Pa) with ultra-high mechanical (42 000 cycles) and washing stabilities (10 cycles) along with high air permeability. Moreover, finite element analysis simulations were conducted to reveal deformation mechanism differences between the monolithic and classical design. Finally, in order to demonstrate their true potential, fabricated MCSs were utilized in real-time body motion monitoring, word and proximity detection.

In the second part, a cellulose-based supramolecular bio-polymer gel that possesses high ionic conductivity (9.85×10^{-4} S cm^{-4} at 25 $^{\circ}$C) and exceptional structural integrity was developed. An iontronic pressure sensor was fabricated with record sensitivity (1 475 000 kPa^{-1}) using the supramolecular bio-polymer gel as a dielectric layer. The combination of in-situ 3D Bode and 3D areal capacitance analyses allowed a deep understanding of the record sensitivity and detection mechanism of the iontronic pressure sensors. A prototype smart glove was fabricated for object recognition from the tactile feedback of the sensors and an object classification accuracy of 90% is demonstrated with only 8 sensors.

.

Keywords: Capacitive Pressure Sensors, Wearable Electronics, Human-Machine Interface Devices, Flexible Electronics, Object Recognition

ÖZ

ESNEK VE GİYİLEBİLİR KAPASİTİF BASINÇ SENSÖRLERİ İÇİN HASSASİYET İYİLEŞTİRME STRATEJİLERİ VE UYGULAMALARI

Çiçek, Melih Ögeday
Yüksek Lisans, Metalurji ve Malzeme Mühendisliği
Tez Yöneticisi: Prof. Dr. Hüsnü Emrah Ünalan
Ortak Tez Yöneticisi: Dr.Öğr. Simge Çınar

Ağustos 2022, 109 sayfa

Giyilebilir elektronik, robotik, insan-makine arayüz cihazları ve elektronik ciltteki gelişmelere paralel olarak basınç sensörleri büyük ilgi görmüştür. Bu alanda, kapasitif basınç sensörleri, yüksek hassasiyetleri, yüksek kararlılıkları, hızlı tepki/kurtarma süreleri ve basit üretim yolları nedeniyle artan araştırma ilgisini çekmektedir. Kapasitif basınç sensörleri öne çıkan özelliklere sahip olsa da, giyilebilir teknolojide daha yaygın hale gelmeden önce daha kat edilmesi gereken uzun bir yol var. Günümüz kapasitif basınç sensörlerinin hassasiyetinin arttırılması bu alandaki en kritik önceliklerden biridir.

Bu çalışmanın ilk bölümünde, kapasitif basınç sensörlerinin duyarlılıkları, kolay imalat yöntemleri ve rasyonel sensör tasarımları kullanılarak iyileştirildi. Bu bağlamda, tezin ilk kısmı, benzersiz bir monolitik tasarıma sahip, düşük maliyetli, hafif, paralel plaka kapasitif bir sensör önermektedir. Bu tasarım, sensörlerin hassasiyetlerini önemli ölçüde geliştirmesine olanak tanır. Yoğunluğu 10.78 mg/cm3 kadar düşük olan monolitik kapasitif sensör (MCS), gümüş nanotel elektrotlu ve koruyucu ince bir polidimetilsiloksan kaplamalı, ticari olarak temin edilebilen bir melamin sünger üzerinde 3-D maskeleme tekniği kullanılarak üretildi. Eşsiz tasarımına ek olarak, MCS'ler yüksek hassasiyet (1,28 kPa^{-1} 'e kadar), hızlı tepki/kurtarma süresi (18 ms/54 ms), çok düşük basınçları algılama yeteneği (0,5

Pa), yüksek hava geçirgenliği, ultra yüksek mekanik (42 000 döngü) ve yıkama stabiliteleri (10 döngü) gösterdi. Ayrıca, monolitik ve klasik tasarım arasındaki deformasyon mekanizması farklılıklarını ortaya çıkarmak için sonlu eleman analizi simülasyonları yapılmıştır. Son olarak, gerçek potansiyellerini göstermek için, gerçek zamanlı vücut hareketi izleme, kelime ve yakınlık algılamada üretilen MCS'ler kullanıldı.

İkinci bölümde, yüksek iyonik iletkenliğe (9.85 x 10^{-4} S cm^{-4} 25 ºC 'de) ve olağanüstü yapısal bütünlüğe sahip selüloz bazlı supramoleküler biyo-polimer jel geliştirilmiştir. Dielektrik katman olarak supramoleküler biyo-polimer jel kullanılarak rekor hassasiyette (1 475 000 kPa-1) bir iyontronik basınç sensörü üretildi. 3D Bode ve 3D alansal kapasitans analizlerinin kombinasyonu, iyontronik basınç sensörlerinin kayıt hassasiyeti ve algılama mekanizmasının derinlemesine incelenmesini sağladı. Sensörlerin dokunsal geri bildiriminden nesne tanıma için prototip bir akıllı eldiven üretildi ve yalnızca 8 sensörle %90'lık bir nesne sınıflandırma doğruluğu gösterildi.

Anahtar Kelimeler: Kapasitif Basınç Sensörleri, Giyilebilir Elektronikler, İnsan-Makine Arayüz Cihazlar, Bükülebilir Elektronikler, Obje Tanıma

Dedicated to my dearest sister and mom…

ACKNOWLEDGMENTS

TABLE OF CONTENTS

LIST OF TABLES

TABLES

LIST OF FIGURES

FIGURES

CHAPTER 1

INTRODUCTION

1.1 Flexible and Wearable Pressure Sensors

The key to modern technological advances is efficiently and effectively transforming environmental inputs into the digital output from various sources. Among these environmental sources, processing information from mechanical sources, including pressure, strain, distortion, and acceleration, is crucial. In general, pressure sensing has a wide range of applications. They have been used for medical and industrial applications. Still, they garner significant research interest due to advances in wearable electronics, human-machine interface devices, robotics, and electronic skins.

The discovery of the pressure sensor goes back to 1954, based on the discovery of the pressure resistance variation of germanium (Ge) and silicon (Si) [1]. Depending on the rapid growth of robotics and wearable technology, different flexible pressure sensors have been developed. Up to date, the main research interest in pressure sensors focuses on enhancing the sensitivity, signal-to-noise ratio and response time. In addition, the sensor's response under static and dynamic conditions are crucial factor for many applications.

According to market needs different types of sensing mechanism have been developed for flexible pressure sensors. These sensing mechanisms can be classified as resistivity, piezoelectricity, triboelectricity and capacitance. The comparison of the different sensing mechanisms is compared in Table 1.1 and following sections summarize the characteristic features of the pressure sensor types.

Table 1.1. Comparison of different pressure sensing mechanisms.

Sensing Mechanism	*Resistive*	*Piezoresistive*	*Triboelectric*	*Capacitive*
Sensitivity	Moderate	Low	Low	High
Signal-to-Noise Ratio	Moderate	Low	Low	High
Response Time	Moderate	High	Moderate	Moderate
Dynamic Response	Moderate	High	Moderate	Moderate
Static Response	High	None	None	High

1.1.1 Flexible and Wearable Resistive Pressure Sensors

Resistive pressure sensors have been studied for decades and are actively used in many fields in today's electronics [2]. The sensing mechanism of the resistive pressure sensors is based on the resistance change of a conductive composite under pressure [1]. Applied pressure changes positions and the contact conditions of the conductive fillers. Therefore, a complex sensor structure is not necessary for sensitive resistive pressure sensors. Low power consumption, wide pressure sensing range, tunable sensitivity, and simple manufacturing methods make resistive pressure sensors attractive for engineering purposes. They can be used in many fields, including medical examination, body motion monitoring, soft robotics and so on [2,3]. In recent years, high-performance resistive pressure sensors have been developed based on novel materials. The commonly used conductive materials are metallic nanowires, carbon-based materials, and MXenes (two dimensional inorganic compounds of transition metal carbides, nitrides, or carbonitrides)[1].

Kim et al. developed a resistive pressure sensor based on vertically aligned carbon nanotubes (VACNTs) and embedded these into the polydimethylsiloxane (PDMS) matrix as demonstrated in Figure 1.1 (a) [4]. The photograph of the sensor can be also seen Figure 1.1 (b). Under applied pressure upper and lower VACNT/PDMS composite contact area between electrodes increases and contact resistance decreases

gradually. Addition to increase of the contact area, formation of new pathways for electrons to flow from one electrode to another brings about gradual decrease in contact resistance. The sensor showed a considerable sensitivity of 0.3 kPa^{-1} and a response time of 162 ms. Finally, the developed sensor was used for body motion monitoring. Lo et al. presented an inkjet-printed resistive pressure sensor based on silver nanoparticles (AgNPs) directly printed on PDMS substrate and encapsulated with a commercial tape [5]. Pressure-induced strain forms microcracks inside the AgNP film. These microcracks lead to an increase in film resistance. The sensor showed a decent sensitivity of 0.48 kPa^{-1}. The fabricated resistive pressure sensor was used for real-time monitoring of the atrial pulse when it was placed over the wrist (Figure 1.1 (c) and (d)). A periodic pulse can be recorded with the help of the sensor as shown in Figure 1e.
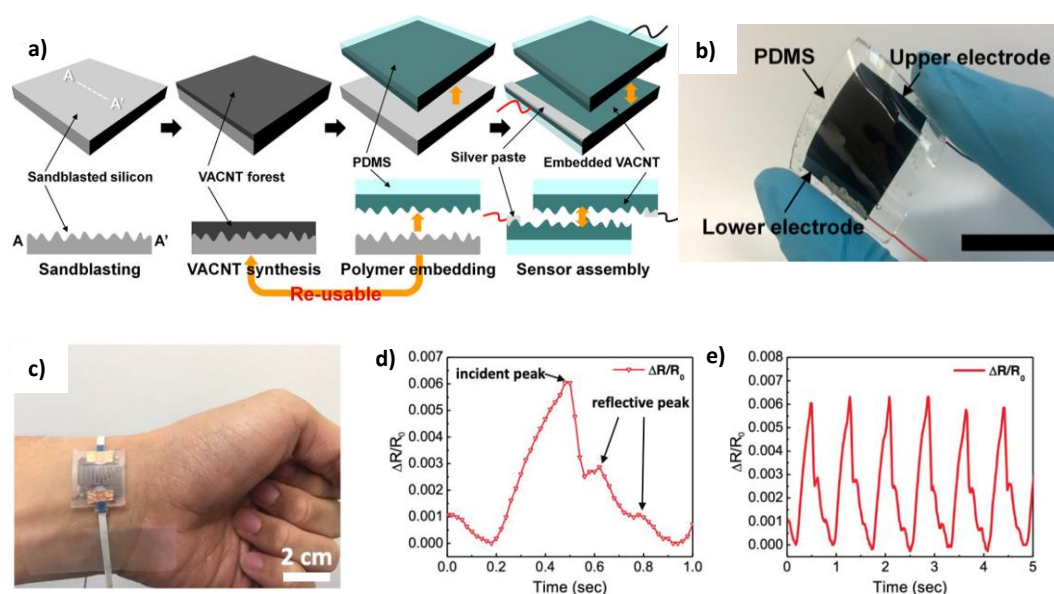
Figure 1.1. Flexible and wearable resistive pressure sensors. a) Fabrication route of the VACNT/PDMS composite based resistive pressure sensor. b) Photograph of the fabricated pressure sensor [4]. c) Photograph of the inkjet printed resistive pressure sensor on wrist. d) Artial pulse measurement of data take form the inkjet printed sensor. e) Periodic pulse record measured by the inkjet printed resistive pressure sensor [5].

1.1.2   Flexible and Wearable Piezoelectric Pressure Sensors

Piezoelectricity is another concept used for pressure sensors. Under applied mechanical stresses, certain types of crystals and ceramics generate electrical charges [2]. On the surface of the piezoelectric materials, positive and negative charges are arranged in opposite directions, and a potential difference occurs. This potential difference is employed to determine the pressure applied to the structure. Piezoelectricity provides an opportunity to fabricate low-power consumption or self-powered pressure sensors. However, limited number of materials can be used for flexible and wearable piezoelectric pressure sensors. Lead zirconate-titanate (PZT), barium titanate ($BaTiO_3$), zinc oxide (ZnO) and poly(vinylidenefluoride-trifluoroethylene) (P(VDF-TrFE)) are the main examples of these materials [1]. Even though piezoelectric pressure sensors can be favorable for lower power consumption for sensor pairs used in internet-of-things (IoT), insufficient sensitivity and limited number of sensing material variations are the main disadvantages of these type of sensors.

Persano et al. developed a flexible piezoelectric pressure sensor based on electrospun P(VDF-TrFe) fibers and photograph of the sensor can be seen in Figure 1.2 (a) [6]. The fabricated device exhibits high resolution in the high pressure range that can sense 0.1 Pa as shown in Figure 1.2 (b). Tan et al. proposed a wearable, flexible textile-based, hierarchically structured piezoelectric pressure sensor [7]. Single-crystalline ZnO nanorods and poly(vinylidene fluoride) (PVDF) membrane were selected as piezoelectric materials, and conductive reduced graphene oxide (rGO) polyester fabrics were used as top and bottom electrodes and structure was encapsulated between polyimide (PI) tape and the PDMS mold as demonstrated in Figure 1.2 (c). The sensor's sensitivity is measured as 0.62 kPa^{-1} (Figure 1.2 (d)). Finally, the fabricated sensor showed a promising practical application capability for self-powered wearable smart clothing. It can detect bending of the the finger and the wrist movements as can be seen in Figure 2 (e) and (f).
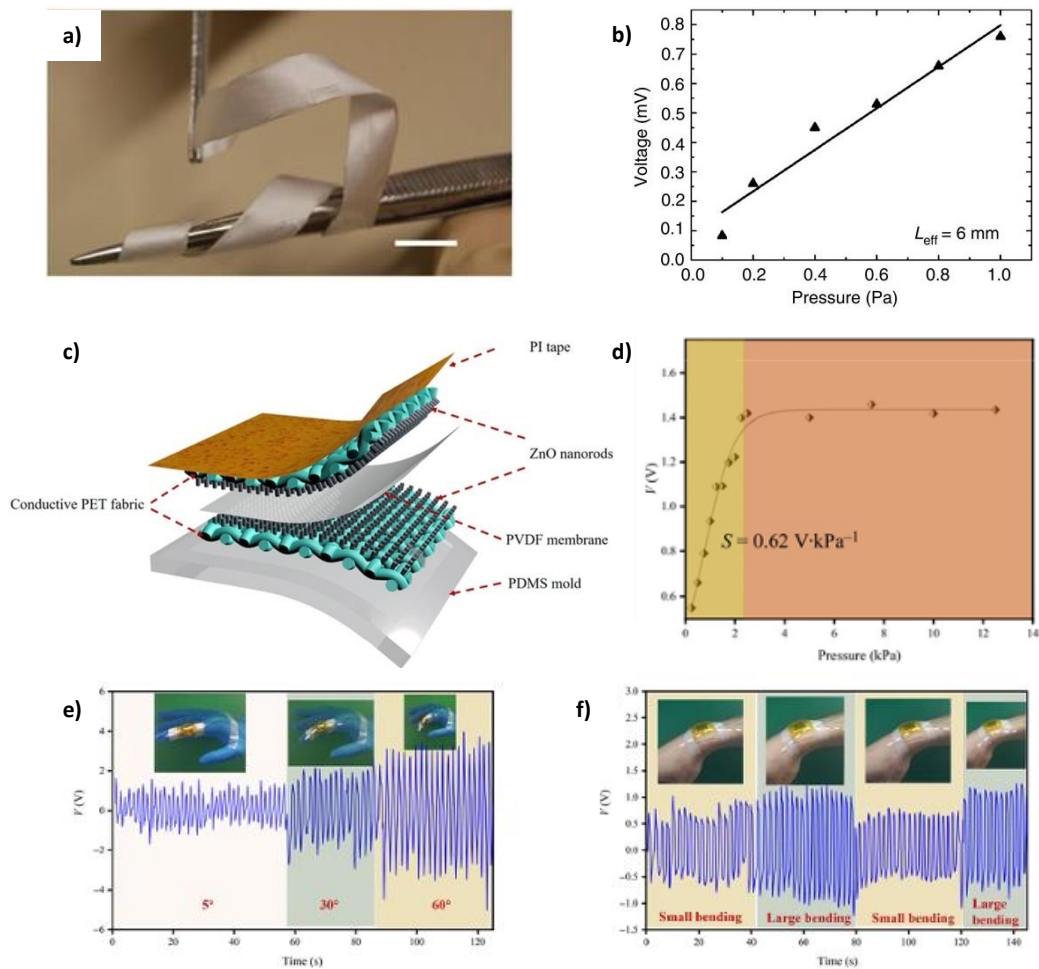
Figure 1.2. Flexible and wearable piezoelectric pressure sensors. a) Photograph of the on electrospun P(VDF-TrFe) fibers based piezoelectric pressure sensor. b) Response to various pressure and the minimum pressure detection limit of the pressure sensor [6]. c) Schematic of the single crystalline ZnO nanorods and PVDF membrane based piezoelectric pressure sensor. d) Sensitivity measurement of the fabricated pressure sensor. e) Finger bending measurements taken by the fabricated piezoelectric pressure sensor. f) Response of the sensor under various wrist bending conditions [7].

1.1.3 Flexible and Wearable Triboelectric Pressure Sensors

The triboelectric effect was known for centuries [8]. However, the idea of generating power from the triboelectric effect was first proposed by Wang et al. in 2012 [9]. In the triboelectrification process, after contact formation between two adjacent surfaces, the surfaces of the contact materials are charged electrically [10]. The created charges form a potential difference between electrodes, and electrons flow from one to the other with the help of external circuitry. Produced current depends on many factors, including triboelectric pairs, the geometry of the triboelectric and the electrode layers, contact/separation frequency, and the applied pressure. By regulating the above-mentioned parameters, the signal-to-noise ratio and the sensitivity of the pressure sensors utilizing triboelectric effect can be improved. Therefore, triboelectric sensors can be a potential alternative for flexible and wearable pressure sensing [11]. However, the performance of the triboelectric generators strongly depend on environmental conditions. In brief, temperature and the relative humidity of the environment change the output performance of the devices. Moreover, the triboelectric pairs' chemical and thermal backgrounds can change the generators' behavior [12]. Consequently, these issues must be addressed before actively using triboelectric pressure sensors.

To date, several flexible and wearable triboelectric pressure sensors have been reported in the literature [10,11,21,22,13–20]. In 2013 Wang's group firstly proposed a high-sensitivity self-power triboelectric pressure sensor [14]. They reported a self-powered pressure mapping approach based on triboelectric effect between the PDMS membrane modified with micropatterned pyramid structure and Ag NWs. Gold (Au) and aluminum (Al) electrodes were used as current collectros for micropatterned PDMS and Ag NW, respectively. Schematic of the fabricated triboelectric pressure sensor can be seen in Figure 1.3 (a). Inset of the figure shows the photograph of the fabricated sensor. As shown in Figure 1.3 (b) with the help of the voltage output of the sensor different applied pressures can be resolved. The highest sensitivity of the triboelectric pressure sensor was recorded as 0.31 kPa^{-1} (Figure 1.3 (c)).

Vivekananthan et al. fabricated a triboelectric pressure sensor based on sandpaper patterned silicone elastomer and nickel (Ni) foam as triboelectrification layers [18]. Schematic and the photograph of the sensor is shown in Figure 1.3 (d). Al electrode was used as current collector for silicone eleastomer and the structure was attached to polyethylene terephthalate (PET) sheet to finalize the sensor structure (Figure 3d). As a pressure sensor, the fabricated device showed a linear sensing behavior with a sensitivity of 0.492 µA kPa^{-1} (Figure 1.3 (e)).
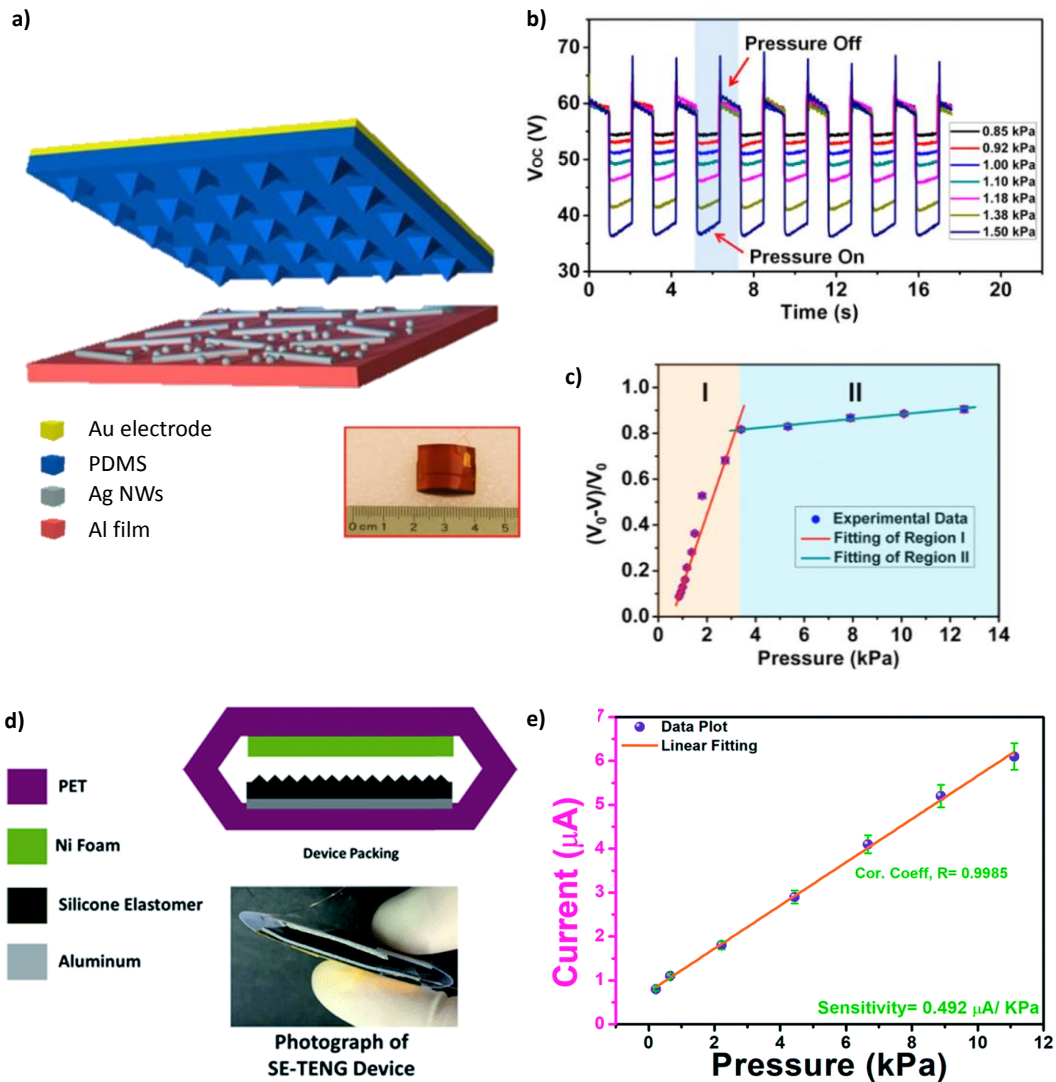
Figure 1.3. Flexible and wearable triboelectric pressure sensors. a) Schematic of the triboelectric pressure sensor based on micropatterned PDMS and Ag NWs. Photograph of the sensor was provided in the inset of the figure. b) Voltage response of the pressure sensor under various applied pressures. c) Sensitivity measurement of the pressure sensor [14]. d) Schematic and the photograph of the triboelectric pressure sensor meade up of silicone eleastomer and the Ni foam triboelectric layers. e) Sensitivity measurement of the triboelectric pressure sensor [18].

1.1.4 Flexible and Wearable Capacitive Pressure Sensors

Capacitive pressure sensors can be described as parallel plate capacitors. They consist of two electrode layers placed parallelly and a dielectric layer between them. Applied pressure is sensed based on the capacitance change of the device. The following equation explains their behavior:

$$C = \frac{q}{V} \quad (1.1)$$

,where q is the stored charge (in coulombs, C), V is the potential difference across the parallel electrodes (in volts, V) and C is the capacitance (in farads, F). Charge will accumulate in the system when a potential is applied across it. During this process a current (displacement current) flows through the system [23]. Therefore, the current magnitude depends on the system's resistance.
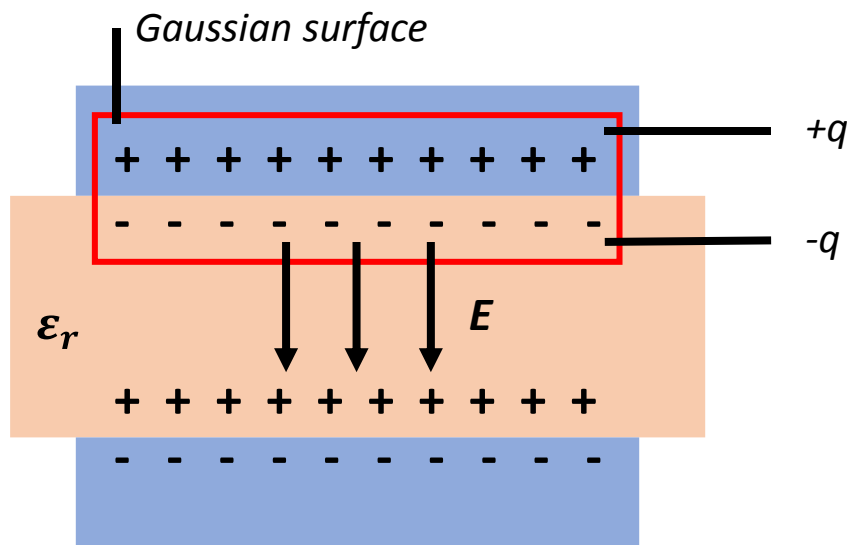
Figure 1.4. Schematic distribution of electric field (E), charges (q) on electrode and the dielectric layer for a parallel plate capacitor with a dielectric layer whose dielectric constant is ε_r .

According to Gauss' law, charge q enclosed by a Gaussian surface surrounding one of the parallel plates with a dielectric medium in Figure 1.4 is calculated as follows:

9

$$q = \varepsilon_0\, \varepsilon_r\, EA \quad (1.2)$$

,where E is the electric field across the parallel plates, ε_r is the relative permittivity of the dielectric layer, ε_0 is the vacuum permittivity, and A denotes the active sensing area of the parallel plates. It is known that:

$$V = Ed \quad (1.3)$$

,where d is the separation distance of the parallel plates. If q from Equation (1.2) and V from Equation (1.3) is submitted into Equation (1.1), we get

$$C = \frac{\varepsilon_r \varepsilon_0 A}{d} \quad (1.4)$$

,where C is the measured capacitance, and d is the thickness of the dielectric layer. The primary capacitance of the parallel plate capacitive pressure sensors is calculated with Equation (1.4). The device's capacitance change is related to the alteration of one of the parameters mentioned above. According to the given equations, capacitive pressure sensors' capacitance solely depends on the geometrical and electrical properties of the components and independent of the applied voltage [23]. However, it should be noted that the electrical double layer (EDL) and pseudocapacitive effects are not included in Equation (1.4).

The EDL formation at the electrode/electrolyte interface has been known since 1879 [24]. The electrode and electrolyte interface experimentally behaves like a capacitor [23]. At an applied voltage, the charges and the dipoles exist on the electrode and electrolyte surfaces. In general, EDL gives the characteristics of the dipoles and the charged species at the electrode/electrolyte interface. The EDL is characterized by a double layer capacitance typically at the level of μF [23].

Capacitive pressure sensors have several advantages over the other types of pressure sensors. They have a simple structure, lower power consumption, and fast response time. Additionally, the skin-like sensing behavior of the capacitive pressure sensors make them more convenient for the next generation electronics to be used as electronic skin. However, the capacitive pressure sensors suffer from low initial

capacitance, making them highly sensitive to external noise sources. Moreover, the sensitivity of the capacitive pressure sensors should be further improved to be used more frequently in many fields: human-motion monitoring and human-machine interactions. With the help of the enhanced sensitivity, pressure resolution increases, allowing to sense small changes in the corresponding environment. Thanks to those, the capacitive pressure sensors can be an unalterable part of the next generation of electronics. Therefore, it is crucial to select the appropriate sensor design and material selection to improve their endurance to the environmental noise and enhance their sensitivity. There are several strategies to increase the performance of capacitive pressure sensors in the literature.

1.1.4.1   Sensitivity Improvement Strategies in Capacitive Pressure Sensors

1.1.4.1.1   Porous Dielectrics

Usage of the porous dielectric layers has become a popular approach to increasing the sensitivity of the capacitive pressure sensors [1]. The main advantage of using a porous dielectric layer is decreasing stiffness, making it highly compressible. This resulted in a more significant change in the dielectric thickness under compressive load, higher capacitance, and higher sensitivity. The more considerable deformation was demonstrated by employing indentation depth profiles of the nonporous and porous dielectric layers. The indentation depth of the porous layer was higher than that of the nonporous layer for applied pressure. Also, these results are further supported by the stiffness of the porous and the nonporous layer. The former has lower stiffness than the nonporous layer [25].

As mentioned in Equation (1.4), capacitance is directly related to the structure's dielectric constant. Therefore, alteration of the dielectric constant under applied pressure is another important parameter for higher sensitivity to form a parallel plate capacitive pressure sensor. Air voids in the porous layer decrease the initial dielectric constant. When pressure is applied to the capacitive pressure sensor with a porous

11

dielectric layer, air in the voids squeezes out. It fills with the layer's skeleton, which increases the structure's effective dielectric constant. Since the dielectric constant of the skeleton medium is typically higher than that of air ($\varepsilon_{air} \sim 1$). As a result, a greater capacitance change is observed for an applied pressure, leading to improved sensitivity [26].

Kwon et al. compared the effects of using 3D porous dielectric elastomer and a non-patterned dielectric layer[26]. The schematic of the capacitive pressure sensor with 3D porous dielctric is provided in Figure 1.5 (a). Thanks to the obtained microporous structure, even small pressures made the dielectric layer highly deformable. Microporous structure of the dielectric layer with loaded and unloaded conditions can be observed in the SEM images provided in Figure 1.5 (a). The fabricated capacitive pressure sensor can resolve pressures as small as 0.16 Pa. Additionally, they improved sensitivity more than 40 times compared to the non-patterned dielectric elastomer thanks to the high deformability of the dielectric layer and the change in the effective dielectric constant with the applied pressure (Figure 1.5 (b)). Tay et al. fabricated superelastic hexagonal-boron nitride (h-BN)/ PDMS foam and used it as a dielectric layer for a capacitive pressure sensor [27]. As a supporting framework of the porous structure, 3D interconnected network of few-layer h-BN was utilized for h-BN/PDMS composite porous structure with a very low unpressed dielectric constant close to the air and very low density (15 mg/cm^3). Thanks to the very low unpressed dielectric constant and density, the fabricated capacitive pressure sensor showed a high sensitivity of 0.854 kPa^{-1} and could resolve pressures as low as 0.58 Pa.

1.1.4.1.2   Nano-Micropatterned Dielectrics

Nano-micropatterning is the formation of controlled micron-sized patterns on a dielectric layer using different methods, including molding, engraving, and classical lithography. [28] Various structures can be employed in nano-micropatterning. Pillars,

bumps, pyramids, and random patterns are the most commonly used nano-micropatterns for high sensitivity capacitive pressure sensors. [29]

Nano-micropatterned dielectrics work in a similar way to porous dielectrics. Nano-micropatterning introduces air gap between electrodes and the dielectric layer. Therefore, the stiffness of the structure decreases considerably. Under an applied load change, the capacitance thickness becomes more prominent compared to the un-patterned structure, which brings about greater capacitance change. Additionally, with the addition of the air gaps, initial dielectric constant of the structure gets a remarkably low value. After applying a load to the sensor, the effective dielectric constant increases due to the removal of the air gaps, which causes an additional increase in the capacitance and the sensitivity of the capacitive pressure sensor.

A capacitive pressure sensor fabricated with interlocked asymmetric nano-cones based on P(VDF-TrFE) as dielectric layer with copper (Cu) foil electrode was demonstrated by Niu et al[30]. Cone-shaped structures were obtained from the anodized aluminum oxide template in a highly ordered and controllable manner. Benefiting from this, the fabricated capacitive pressure sensor showed a high sensitivity (6.583 kPa^{-1}). Thanks to micropatterning of the dielectric layer sensitivity of the pressure sensor has been enhanced more than 10 times. Yang et al. combined two approaches (nano-microstructure dielectric and porous dielectrics) in order to get higher sensitivity [31]. Device schematic is provided in Figure 1.5 (c). An ultrahigh sensitivity is utilized by using a porous micro-pyramid dielectric layer for the capacitive pressure sensor. The device exhibited a sensitivity of 44.5 kPa^{-1} and could resolve pressures as low as 0.14 Pa. compared to the solid micro-pyramid shaped dielectric, porous micro-pyramid shaped dielectric demonstrated up 15 times higher sensitivity. Sensitivities of these two sensor structure is given in Figure 1.5 (d). Also, sensitivities in different pressure regimes can be observed in Figure 1.5 (e). This difference in sensitivity was explained by the difference in the rate of change in the effective dielectric constant and the compressive modulus between micro-pyramid dielectric and porous micro-pyramid dielectric layers.

Employing wrinkled dielectrics to get micron-sized features is another extensively used method to improve the sensitivity of the capacitive pressure sensors. [32–34] The wrinkled dielectrics are fabricated by releasing a pre-stretched elastomer film after curing. Baek et al. fabricated a double-sided wrinkled structure using EcoFlex as elastomer and enhanced the sensitivity of the capacitive pressure sensor from 4.8 x 10^{-6} kPa^{-1} to 0.013 kPa^{-1} [32]. The sensitivity enhancement is directly related to the two mechanisms mentioned in previous sections, which are decreasing stiffness and the dielectric constant of the structure.

1.1.4.1.3 Ionically Conductive Dielectrics

The capacitive pressure sensors' sensitivity has been improved significantly with the formerly mentioned strategies. However, they are still limited by the effective dielectric constant and the thickness change of the dielectric layer. In addition to these limitations, they are prone to parasitic noise due to pF level capacitance obtained from the non-ionic dielectric-based capacitive pressure sensors. These limitations and drawbacks were overcome with the introduction of the EDL to the capacitive pressure sensors due to the nF/µF level measured capacitance.

When an ionically conductive dielectric layer is used, sensing mainly relies on the formation of the EDL and the change in the electrode/electrolyte interfacial area [35]. Using ionically conductive dielectrics eliminates the limitations and drawbacks of non-ionic dielectrics thanks to the 1000-fold increment in the capacitance values. As mentioned above, these types of capacitive pressure sensors depend on the formation of the EDL layer at the electrode/electrolyte interface and its areal dependency to the applied pressure. Therefore, for these types of capacitive pressure sensors, the primary consideration is the control of the interfacial properties in a mechanically reversible way to get repeatable and controllable results. Additionally, these types of capacitive pressure sensors are also known as iontronic pressure sensors in the literature [35].

In 2011, Pan et al. proposed the use of electrolytes to form an electrode-electrolyte interface to get high sensitivity (1.58 µF kPa^{-1}) [36]. This type of sensing relies on both the liquid droplet's EDL formation and interfacial deformability. However, the droplet-based capacitive pressure sensors suffered from a lack of mechanical control and leakage problems. Solid polymer electrolyte-based capacitive pressure sensors have been developed to solve the addressed problems. Li et al. demonstrated the first examples of solid polymer electrolyte usage in capacitive pressure sensors. [37] They used P(VDF-HFP) and 1-Ethyl- 3-methylimidazolium bis(trifluoromethylsulfonyl)imide ([EMIM][TFSI]) fibers as ionically conductive dielectric layer and sandwiched between two conductive fabrics. They get a considerable sensitivity (114 nF kPa^{-1}) and a decent pressure resolution (2.4 Pa). Liu et al. demonstrated a susceptible capacitive pressure sensor with a polyurethane (PU) foam that was coated with 1-Butyl-3-methylimidazolium tetrafluoroborate ([BMIM]BF4) ionic liquid (IL). [38] Schematic of the sensor structrure is provided in Figure 1.5 (f). The high porosity of the PU foam lead dielectric layer to possess a very low modulus and very small electrode-electrolyte contact area at the unloaded condition. This brings about a small initial capacitance related to that very high sensitivity (9280 kPa^{-1}) (Figure 1.5 (g)).
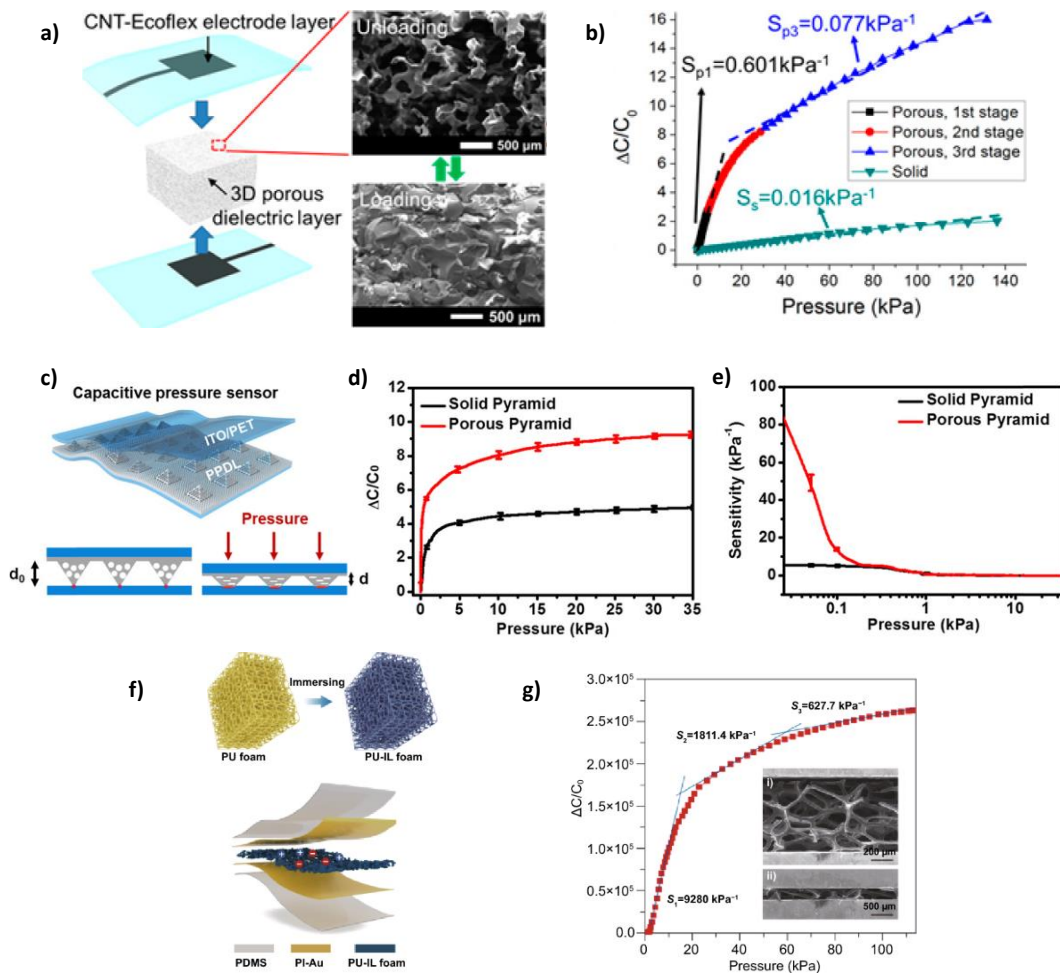
Figure 1.5. Flexible and wearable capacitive pressure sensors. a) Schematic of the capacitive pressure sensor with 3D porous dielctric layer. SEM images of the dielectric layer under loaded and unloaded conditions are also provided. b) Sensitivity of measurements and the comparison of the capacitive pressure sensors with 3D porous dielectric and flat dielctric layer [26]. c) Schematic of the capacitive pressure sensor with porous micropatterned dielctric. d) Sensitivities of the devices with porous pyramid dielectric structure and solid pyramid dielctric structure. e) Sensitivity comparison of the sensors with different dielectric structures [31]. f) Schematic of the IL coated PU foam to be used as dielctric layer for the capacitive pressure sensor. g) Sensitivity measurement of the fabricated sensor [38].

1.1.4.1.4   Effects of Electrode Materials

Morphology and materials of the electrodes are other important parameters that considerably improve capacitive pressure sensor's sensitivity. Even though main research focuses on the dielectric layer's morphology to improve sensitivity of the capacitive pressure sensors, researchers are working on electrode materials and morphology. [39–45]

1.1.4.1.4.1 Effects of Electrode Morphology

Electrode morphology work in the same way with the effect of the dielectric morphology on the sensitivity. The sensitivity enhancement is based on contact area increment and the effective dielectric constant with the applied pressure increase. Joo et al. fabricated buckled electrode layer and coated the electrode layer with Ag NWs [42]. Schematic of the sensor structure is provided in Figure 1.6 (a). An un-patterned dielectric layer made up of polyvinyl pyrrolidone (PVP) was used as the dielectric layer. Under the applied pressure, the Ag NW embedded bent electrode layer is deformed, the air gaps between the dielectric layer and the bent electrode are eliminated, increasing the effective dielectric constant and electrode-dielectric contact area. Thanks to this method, the device's sensitivity is dramatically increased to 3.8 kPa^{-1} (Figure 1.6 (b)). Similarly, Qiu et al. coated PU foam with graphene nanoplates (GNPs), carboxyl-functionalized multiwalled carbon nanotubes (MWCNTs) and silicon rubber (SR) to get a 3D electrode structure [43]. The capacitive pressure sensor consists of the 3D porous upper electrode, a flat dielectric layer, and the flat Au bottom electrode. Under compression addition to the formerly mentioned mechanisms, decrease of the electrode resistance contributed to the improvement of the sensitivity of the capacitive pressure sensor.

17

1.1.4.1.4.2 Effects of Electrode Materials

The importance of the electrode material for a capacitive pressure sensor becomes significantly prominent when an ionically conductive dielectric layer is used. Although the importance of the electrode materials on the performance of the supercapacitors and batteries have been known for years, there are few examples in the literature about the effects of electrode materials on the performance of the capacitive pressure sensors with an ionically conductive dielectric layer [40,44]. Gao et al. developed a capacitive pressure sensor based on $Ti_3C_2T_x$ MXene top floating electrode and a microstructured dielectric layer based on poly(vinyl alcohol) (PVA) and potassium hydroxide (KOH) [44]. Photograph oıf the sensor is given in Figure 1.6 (c). Intercalation of K^+ ions to the galleries of the MXene layers under high pressure allowed sensor to show very high sensitivity (46 730 kPa^{-1}). The sensitivity measurements demonstrated that using an intercalative electrode significanlty improves the pressure sensor's sensitivity. It was reported that the sensitivity of the MXene-based sensor was much higher than that of the metal electrode-based sensor (Figure 1.6 (d)). Wang et al. proposed a capacitive pressure senor based on poly(3,4-ethyl enedioxythiophene):poly(styrenesulfonate) (PEDOT:PSS) as pseudocapacitive electrodes and porous PU/NaCl/PVA composite as an ionically conductive dielectric layer [40]. Finally, the sensor structure enriched with poly(methylmethacrylate) (PMMA) microspheres, which acts as spacer, were placed between the electrodes and electrolyte interfaces. A very promising sensitivity (162.9 kPa^{-1}) was obtained from the structure with a very fast response time (25 ms).
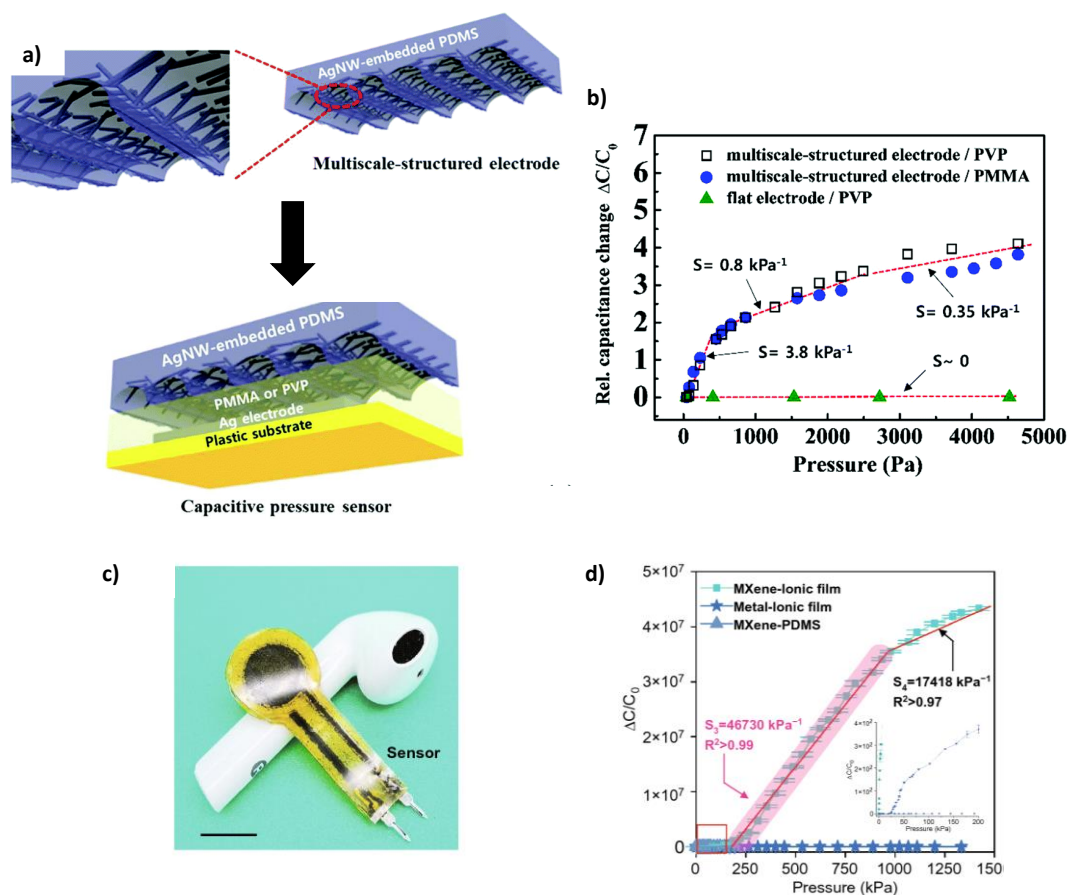
Figure 1.6. Effects of electrode structure and materials on the sensitivity of the capacitive pressure sensors. a) Schematic of the sensor structure with buckled electrode layer and unpatterned dielectric layer. b) Sensitivity comparison of the capacitive pressure sensors with buckled and flat electrode layers [42]. c) Photograph of the sensor with MXene electrodes. d) Sensitivity comparison of the capacitive pressure sensors with MXene electrodes and metal electrodes.

1.1.4.2   Applications of the Capacitive Pressure Sensors

As mentioned earlier, capacitive pressure sensors have numerous advantages. Their high and tunable sensitivity, rapid response/recovery times and stabilities allow them to be used in numerous applications. This section discusses two main application areas: which are motion – signal monitoring and human-machine interactions.

The reported wearable pressure sensors mainly focus on monitoring physiological signals. The artery pulses provide essential physiological information. Thanks to this information, one can interpret the cardiological health conditions of humans. Lin et al. developed an ionically conductive capacitive pressure sensor for fingertip pulse monitoring [46]. The developed sensor can detect stable and high-resolution pulses under static and dynamic conditions. This work also demonstrated that fingertip pulse measurements could be used as a standard method for pulse detection because the measured pulses show similar behavior to that of the radial artery. Chen et al. showed the use of a capacitive pressure sensor to detect blink reflexes [47]. A prototype smart glove was fabricated based on the pressure sensors and continuously monitor ocular muscular movements. The blink patterns were captured with more than 96% accuracy and used to distinguish blinking properties. Xu et al. employed 6x6 capacitive pressure sensor arrays for deep learning aided knee joint rehabilitation [48]. Meniscus injuries can be encountered during clinical rehabilitation due to over-flexed or extended states of the knees. The primary detection points of these injuries are the inherent pressure levels and position of the knees. The fabricated sensor array was employed to monitor these parameters in real-time through rehabilitation. Pressure map distribution of the sensor arrays gave information about pressure distribution and the knee position and effectively predicted them with the help of deep learning.

With the improvement in technology, capacitive pressure sensors have been widely employed for human-machine interactions. Kim et al. fabricated a transparent capacitive pressure sensor with 95% transparency[49]. A prototype full-size transparent keyboard was fabricated to demonstrate the sensors' potential (Figure 1.7 (a)). The prototype transparent keyboard includes 28 sensing units in which 26 were assigned to the alphabet, and others were assigned to a space bar and a dot. A data acquisition unit was used to collect data from the sensing units and transmitted these data to a computer. Moreover, hard and the soft touches were determined with the help of the capacitance change which demonstrated the keyboards capability for 3D touching. Thanks to this property, the soft and hard touches distinguished lower and

upper cases in real time and allowed to be used as a keyboard (Figure 1.7 (b)). Lu et al. demonstrated use of capacitive pressure sensors by laminating them on an artificial limb and measure the pressure distribution of a tennis ball[50]. Figure 1.7 (c) shows the distribution of the sensor on the artificial hand. The results showed that applied pressure on the fingers is higher than that of palm (Figure 1.7 (d)). The capacitive pressure sensors were also employed in the field of flexible robotics. Gao et al. mounted capacitive pressure sensors on the surface of sift gripper (Figure 1.7 (e)) [44]. The gripper was directed to hold an orange, and the sensor measured the grasping force in real time throughout this procedure as shown in Figure 1.7 (f).
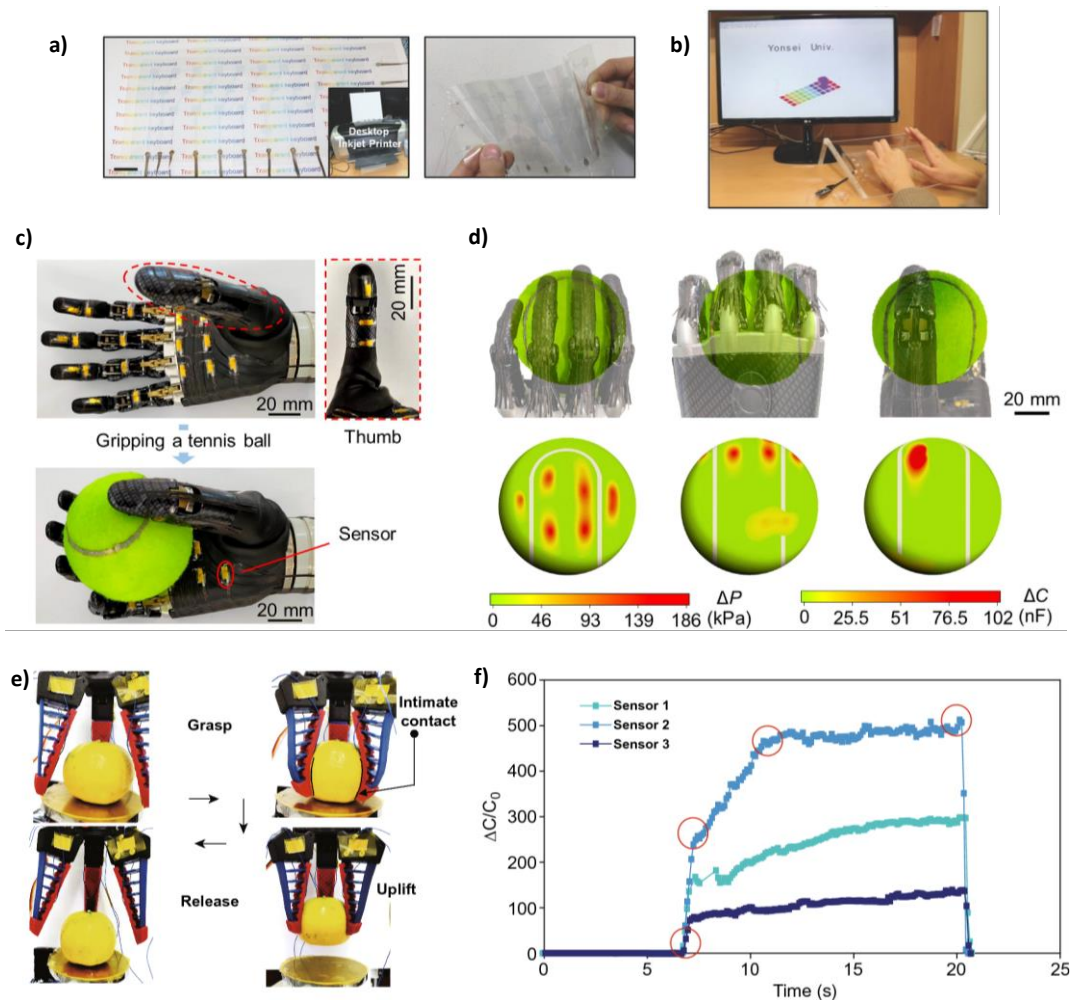
Figure 1.7. Applications of the capacitive pressure sensors. a) Photograph of the keyboard made up of transparent capacitive pressure sensor array. b) Letters written by the transparent capacitive pressure sensor arrays. c) Distribution of the capacitive pressure sensors over the artificial hand. d) Pressure distribution while holding the tennis ball [50]. e) Holding position of the soft gripper. f) Time dependent pressure distribution over the fabricated capacitive pressure sensor while holding an orange [44].

CHAPTER 2

SEAMLESS MONOLITHIC DESIGN FOR FOAM BASED FLEXIBLE PARALLEL PLATE CAPACITIVE SENSORS

2.1   Introduction

Over the last decade, highly sensitive, flexible, lightweight and wearable electronic devices gathered considerable interest due to their numerous applications in electronic skins for robotics [51–54], real-time healthcare monitoring devices[55–58], tactile information systems[59–61] and so on. Significant efforts have been spent on pressure sensors for their use in wearable devices. Mechanical inputs from environment are converted to real-time electrical signals by many types of pressure sensors, including capacitive [62–65], piezoelectric [66,67], triboelectric [68–70] and piezoresistive sensors[71–73] . Although sensitivities of the piezoresistive sensors are higher[24-26], long linear response range, low power consumption, cycling stability and fast response make capacitive sensors promising candidates for wearable electronics. It was demonstrated that the capacitive pressure sensors can be attached or carried by the human body for human-machine interface or collecting physiological signals for real-time healthcare monitoring. However, commercialized or recently developed capacitive pressure sensors are mainly composed of planar separate electrodes[31,32] , which lead to user movement restriction and aesthetic loss. In addition, by having a rigid planar structure, the breathability of the body is restricted, and it disrupts comfort during long periods of use. Wearable capacitive pressure sensors are desired to be designed as a comfortable platform while providing high sensitivity with a low-pressure detection ability and long-term durability to minimize additional weight and physical constraints on the human body in motion.

Improvement of the sensitivity of capacitive pressure sensors is achieved by various strategies. These include the use of micropatterned dielectric layers or electrode surfaces [30], nanofibrous membrane, dielectric layers with microspheres[74,75] and ionic-liquid active dielectric layers[76–78]. The capacitive pressure sensors based on micro/nano patterned or ion-liquid activated structures show promising sensitivity and quick response to external stimuli. These methods are time consuming, expensive and involve complicated production steps, such as electrospinning, etching and photolithography. Alternatively, foam-like structures with a wide variety of polymeric materials like polyelefin[79], polyurethane[80], ecoflex[41] and PDMS[81] can be used in wearable electronics. They are cost-effective, commercially available and can be used for large scale-fabrication. Porous structure of these dielectric layers allows capacitive pressure sensors to be highly sensitive and detect low-pressures. For example, Teo and co-workers have demonstrated a capacitive pressure sensor with a dielectric layer made by boron nitride/polydimethylsiloxane foam and verified that three-dimensional network structure can detect very low-pressures (<1 Pa)[42]. Park and co-workers have showed a capacitive pressure sensor from three dimensional microporous dielectric layer sandwiched between carbon nanotube – ecoflex electrode layers with a sensitivity of 0.601 kPa[-126]. However, both devices with foam-like dielectrics contain rigid, planar electrode layers. Separate planar electrode layer means different mechanical properties of the electrode and the dielectric layer. Insufficient interface between the dielectric material and electrode hampers the mechanical response, decreasing pressure sensing performance of the capacitive sensors[82]. Also, under repeated mechanical stimuli, cracking and delamination can lead to sensor failure. For mechanical stability, additional assembling processes may be required. Yet, these processes usually involve complex physical and chemical procedures, that are time-consuming and costly. In addition to production difficulties, most of the separate planar electrodes are not air permeable and increase the weight of the sensor. Therefore, instead of separately producing dielectric and electrode layers, constructing them on top of a foam enables the sensors to be mechanically stable and truly wearable. The proposed seamless

monolithic design allows sensors to make use of porous structure of the foam effectively. Moreover, high porosity of the foam and the seamless monolithic design allow parallel plate capacitive pressure sensors to possess high sensitivity, ability to detect low-pressures, breathability, flexibility, soft structure and user comfort, all of which are the highly desirable features for human friendly wearable electronics.

In this work, a pioneer manufacturing technique and design for the fabrication of seamless monolithic parallel plate capacitive pressure sensors using commercially available foam was proposed. The seamless monolithic structure containing both electrode and dielectric layers are produced using a rational three-dimensional masking technique. Electrode layers are produced by coating the outermost layers of the foam with Ag NWs using simple and cost-effective dip-dry method. Ag NWs allowed sensors to preserve their flexibility while maintaining excellent conductivity[83]. Remaining parts of the foam act as a dielectric layer for the capacitive pressure sensor and overall structure is coated with a thin layer of PDMS to increase mechanical and washing stabilities. The fabricated seamless monolithic parallel plate capacitive sensor with a user-friendly structure showed excellent performance in real-time physiological signal monitoring, voice and proximity detection.

2.2   Experimental Procedure

Synthesis of Ag NWs: All glassware were cleaned using acetone (99.8%, Sigma-Aldrich), ethanol (99.85%, Sigma-Aldrich) and finally with deionized water (18.3 MΩ). All chemicals used for Ag NW synthesis and purification were purchased from Sigma-Aldrich and used without further purification. Ag NWs were synthesized according to our previous recipe with some modifications[65]. In a typical synthesis, 1.8 gr of polyvinylpyrolidone (PVP, monomer-based calculation MW = 55000) and 5 mg of sodium chloride (NaCl, 99.5 %) was dissolved in 80 ml of Ethylene glycol (EG, anhydrous, 99.88 %) at 120 ºC, then cooled to room temperature. In another flask, 680 mg of silver nitrate ($AgNO_3$, ACS reagent ≥99.0%) was dissolved in 40 ml of EG at room temperature. Then, $AgNO_3$/EG solution was placed into silicon oil

bath at 120°C. After that, PVP/NaCl/EG solution was added into $AgNO_3$/EG solution with a plastic pipette. Once the addition was completed, the temperature was raised to 160 °C and reaction lasted 80 minutes. Following synthesis, NWs were purified by washing several times with ethanol. The final product was dispersed in ethanol for further processing and characterization.

Fabrication the Sensors: Commercially available melamine foam (Basotect®, BASF) possessing high porosity was washed several times with alcohol and deionized (DI) water. Cleaned foam were dip-coated in molten paraffin (Balmumcu Kimya) to form a 3-D mask. To reveal 250 μm thick electrode layers, paraffin coated melamine foams were immersed into n-hexane (95% Sigma-Aldrich) for 40 seconds. Ag NWs were coated onto the revealed part of the melamine foam using dip-dry method. In brief, melamine pieces were immersed into Ag NW solution for 1 min, taken out and dried at room temperature for 30 mins. The procedure was repeated until sheet resistance of the sample was measured as 10 Ω. For the complete dissolution of paraffin, the melamine foams were immersed into n-hexane for 2 days. After completely dissolving paraffin, copper cable contacts were attached using silver paste. For a protective PDMS overcoat, 5-20 wt.% of PDMS (Sylgard 184 Silicon elastomer, Dow Corning) solution in n-hexane was prepared using PDMS base part A and curing agent part B in a ratio of 10:1 and with certain amount of n-hexane. Prepared solution was mixed with magnetic stirrer for 30 mins at 500 rpm. As-prepared melamine pieces were immersed into the protective over coat solution for 2 hours and cured at 90°C for 1 hour.

To prepare capacitive sensor with classical design, pre-cleaned melamine foams were cut so that the thickness was equal to 2.5 mm, which was equal to the dielectric thickness of the sensors in monolithic design. Ag NW coated PET films were used as conducting electrodes. Copper wires were attached to the conductive film using silver paste. The dielectric layer was sandwiched between two electrode layers and fastened up using Kapton tape. Written consent was obtained from the user, who attached the fabricated sensors to his body and used them.

Characterization: Morphological characterization of the melamine foam and the fabricated sensors were carried out by the SEM (FEI NOVA NANO SEM 430). SEM was operated under an accelerating voltage of 20 kV following a thin gold layer deposition onto the samples. To investigate paraffin residue and possible interaction between PDMS and the melamine foam attenuated total reflectance (ATR) unit of FTIR spectrometer (Bruker ALPHA) with a resolution of 4 cm^{-1} was used within a wavenumber range of 400-4000 cm^{-1}. Compression tests of the fabricated sensors were conducted with Zwick/Roel Z250 tester with 0.05 N preload and 2 mm/min test speed. Cyclic compression and tensile strain tests were made using a hand-made test machine. The capacitance values of the fabricated sensors were measured using Twintex LCR-7200 precision LCR meter. The resistance values of the electrodes were measured with a Keithley 2400 Source meter. The response and the recovery times were evaluated using OriginLab Pro, Rise Time Gadget. To eliminate any irregularities at the transition corner of the signals, the response/recovery times were determined as the time between 10% and 90% of the amplitude.

2.3   Results and Discussions

2.3.1   Sensor Fabrication and Characterization

Overall production steps of the MCSs are schematically shown in Figure 2.1. The MCSs were constructed on a commercially available melamine foam (Figure 2.1-i). The pre-cleaned melamine foam was dipped into molten paraffin and dried at room temperature to form a 3-D mask, completely covering the structure (Figure 2.1-ii). The paraffin coated foam was then immersed into n-hexane to dissolve outermost region of the paraffin and reveal the foam skeleton (Figure 2.1-iii). The revealed regions were coated with Ag NWs using simple dip and dry method to form upper and lower electrode layers of the MCS (Figure 2.1-iv). Upon consecutive dip and dry cycles, revealed foam skeleton was conformally coated with the Ag NWs, as presented in Figure 2.2 (a). Resistance of the Ag NW coated region was measured as 10 Ω. The paraffin mask prevented penetration of Ag NWs towards the interior

region of the foam (Figure 2.1-iv). The uncoated interior regions of the foam served as the dielectric layer of the MCS, by separating the upper and the lower electrodes both electrically and physically. Remaining paraffin mask was dissolved by n-hexane to reveal the seamless monolithic structure as demonstrated in Figure 2.1-v. As electrical contacts, copper wires were attached to the structure with the help of silver paste. Finally, resulting structure was immersed into a PDMS solution diluted with n-hexane to increase the mechanical and washing stabilities of the capacitive sensors (Figure 2.1-vi).
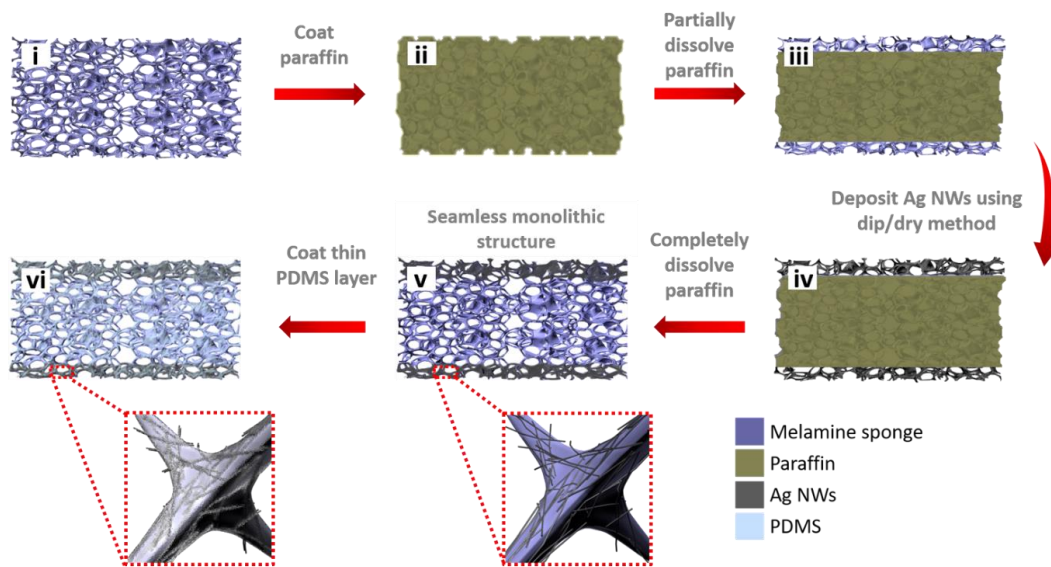
Figure 2.1. Schematic fabrication process of the MCSs.

Four different types of the MCSs were fabricated with different thicknesses of protective PDMS layers. MCS 0 indicates the sensor without a protective PDMS layer. MCS 5, MCS 10 and MCS 20 signify the sensors with different protective PDMS layer thicknesses, achieved through increased PDMS concentrations in the coating solutions. The corresponding PDMS concentrations in the PMDS/n-hexane solutions were 5, 10, 20 wt.%, respectively. As expected, PDMS deposition was the highest at MCS 20 and the lowest at MCS 5. SEM images of MCS 5, MCS 10 and MCS 20 are provided in Figure 2.2 a-d, respectively.
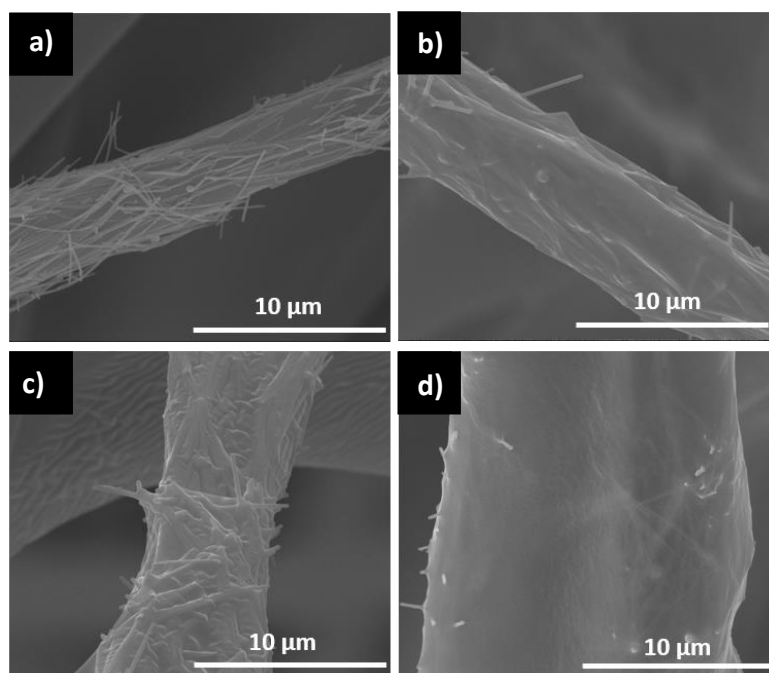
Figure 2.2. SEM images of the melamine sponge. a) SEM image of the skeleton of the sponge coated with Ag NWs using dip-dry method. SEM images of the Ag NW coated melamine sponges with PDMS overcoat of b) MCS 5, c) MCS 10 and d) MCS 20.

Densities of MCS 0, MCS 5, MCS 10 and MCS 20 were measured as 10.78 ± 0.34, 16.15 ± 0.57, 20.65 ± 0.45 and 34.77 ± 0.54 mg/cm^3, respectively. The SEM image of the seamless monolithic capacitive sensor with PDMS overcoat and its corresponding energy dispersive X-ray (EDX) elemental maps are provided in Figure 2.3 (a). It was observed from the EDX map that Ag signal come from surface of the melamine foam, which means that Ag NWs were coated only on the outer layer of the foam skeleton (Figure 2.3 (a-ii)). In addition, while the C signals came from both melamine foam and the PDMS overcoat, Si signal came only from the PDMS layer as provided in Figure 2.3 (a-iii) and (a-iv), respectively. Si signal showed homogeneous distribution of the PDMS overcoat along the skeleton of the foam. A photograph of the fabricated MCS is provided in Figure 2.3 (b). The fabricated MCSs have very low weight and reside on a dandelion flower without any disturbance (Figure 2.3 (c)). The proposed sensor also showed excellent flexibility

and mechanical robustness under various mechanical deformations such as twisting and bending as demonstrated in Figure 2.3 (d-i)-(d-ii). Following each mechanical deformation, sensor was capable of returning to its original form without any permanent deformation.
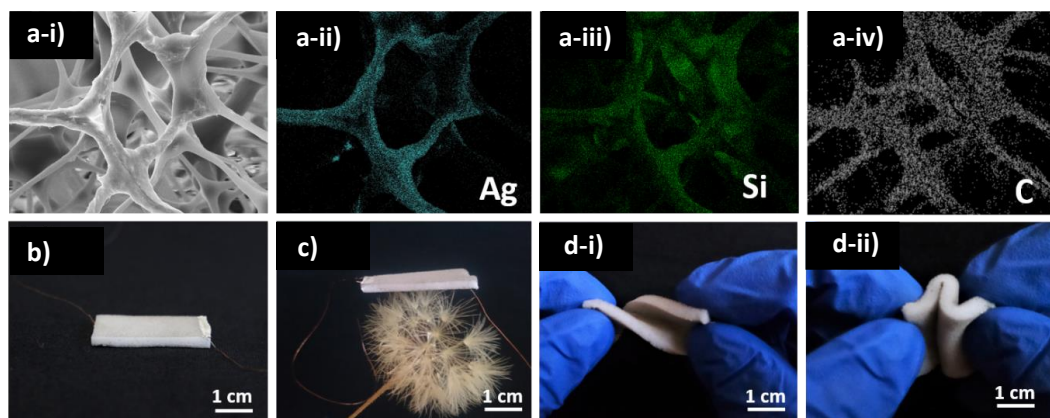
Figure 2.3. (a) (i-iv) SEM images of the MCSs and the corresponding EDX elemental maps. (b) A photograph of the fabricated MCS. (c) Photograph of the fabricated MCS on a dandelion flower. (d) (i-ii) Photographs of MCS under twisting and bending.

2.3.2   Pressure Sensing Mechanism and Device Performance

Capacitance change of the capacitive pressure sensors strongly depend on the stiffness of the structure. This change increases with decreased stiffness. One of the advantages of porous structures is their low stiffness. Applied compressive load on the sensor can easily decrease the distance between two parallel electrodes and thus the capacitance increases. Moreover, in the presence of the compressive loads, air in the pores of the system is replaced easily with the neighboring melamine skeleton. Therefore, in addition to a decrease in the distance between two parallel electrodes of the capacitive sensor, air with a low relative permittivity, is replaced with the high relative permittivity melamine. Decreased stiffness and increased relative permittivity of the porous structure, further increases the sensitivity of the sensor. In addition to advantages of the porous dielectric layer in terms of sensitivity, using

porous electrode layers further enhance the sensitivity of the fabricated sensors. When a compressive load was applied onto the MCSs, pores between Ag NW coated foam skeleton was closed. In conjunction, the distance between the two parallel electrodes further decreased and an increase in the measured capacitance value was observed. Moreover, the air gaps between the skeleton of the foam shrink, which resulted in an additional increase in relative permittivity. In addition to increased relative permittivity under compressive strain, surface resistance of the electrode layers was found to decrease as shown in Figure 2.4. Squeezing out air in the gaps of the structure led to an increase in the contact area between the NWs of the electrode layers changing the surface resistance of the electrode layers. The capacitance characteristics of the capacitive sensors are closely related with the surface resistance of the electrodes. Capacitance of the capacitive sensor was found to increase with decreasing surface resistance under compression. Therefore, porous electrode layers further boosted the change in capacitance. The monolithic design allowed both electrodes and dielectric layers to actively take part in the capacitive pressure sensing through the change in effective relative permittivity and the surface resistance of the electrode layers. On the other hand, in the classical design (a design that use separate dielectric layer and planar solid electrodes), electrodes play a passive role in the sensing of the applied compressive load. Therefore, sensitivity in monolithic design outperforms the classical design by simultaneously utilizing the electrodes and the dielectric layer.
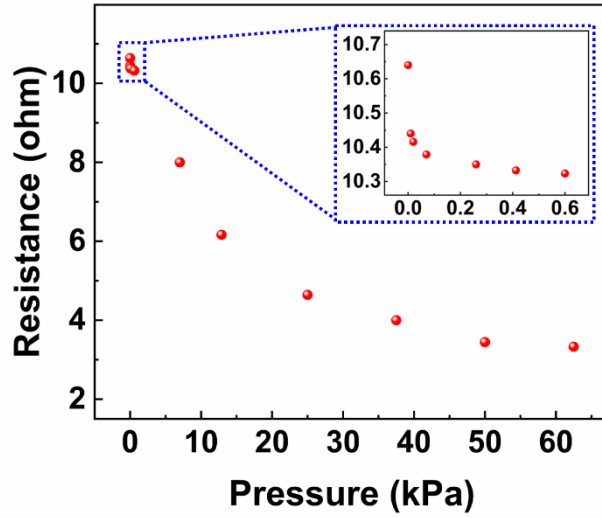
Figure 2.4. Resistance change of the MCS electrode when subjected up to 63 kPa of pressure. Inset shows the resistance change in the electrode subjected up to 600 Pa of pressure.

To simulate mechanical behavior of both the monolithic and classical design under compressive loads, Solid Mechanics module of the COMSOL Multiphysics was used. Applied pressures were defined as boundary loads and the melamine foam under test was taken as hyperelastic material. As shown in Figure 2.5, the nonlinear behavior of the melamine foam under compressive load was described by second order Ogden hyperelastic model in which the uniaxial stress is expressed in terms of the principle stretch (λ):

$$\sigma = \sum_{p=1}^{N} \mu_p \left(\lambda^{\alpha_p - 1} - \lambda^{\frac{\alpha_p}{2} - 1} \right)$$

,where N, μ_p and α_p are the material properties. From the simulation and experimental data (Figure 2.5), material properties of melamine foam μ_1, μ_2 and α_1, α_2 were calculated as 29.46 kPa, 21.82 kPa and -2.383, 5.655, respectively.

In finite element analysis (FEA), PET was considered as a linear elastic material. Young's modulus, Poisson's ratio and the density of the PET layers were taken as, 2.8 GPa, 0.382 and 1.29 x 10^3 kg/m^3, respectively.
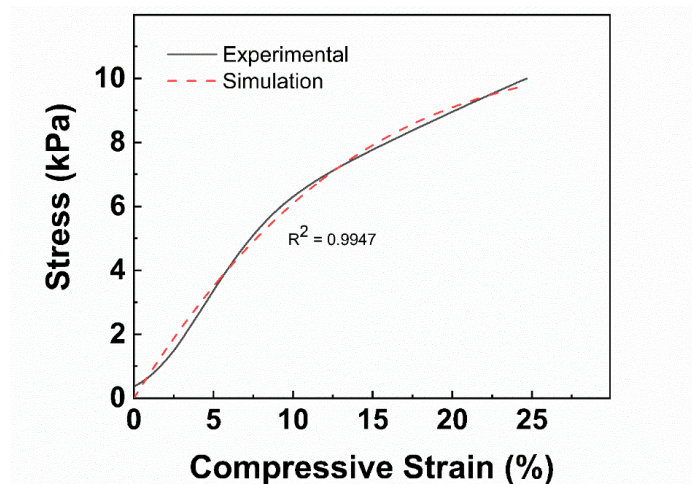
Figure 2.5. Experimental (black line) and simulation (red dots) curves of the compressive strain – pressure curves of the melamine foam with an r-square value of 0.9947.

In the analysis, responses of the sensors with the monolithic design and the classical design were compared in terms of von Mises stress distribution. While the monolithic design contained a single layer of melamine foam with thickness of 3 mm, classical design contained additional two PET layers with 250 μm thickness. Since, purpose of the FEA was to show effect of additional solid planar layers on stress distribution of the sensing layer, porosity of the body was neglected. Also, to show stress distribution on the melamine foam more clearly, resultant stress on the PET layers were ignored on the figure. Abovementioned structures were exposed to pressures of 500, 600, 700 and 800 Pa as presented in Figure 2.6. Difference in the von Misses stress distribution is related with the multiplanar and single-planar structures[43,50,51]. In the classical design, a local increase of the stress was observed at the edges of the body, whereas in the monolithic design, stress was distributed through the body more homogeneously. Moreover, the stress experienced by the body in monolithic design is higher than that in the classical design, as shown in Figure 2. These effects led to better compression of the melamine foam in the monolithic design and removal of air from the open cell structure. On the other hand, in the classical design, localized stress led to only limited compression of the foam

33

and removal of limited amount of air form the structure. These differences in the stress distribution and exposed stress enabled MCSs to detect much lower pressures and have higher sensitivity.
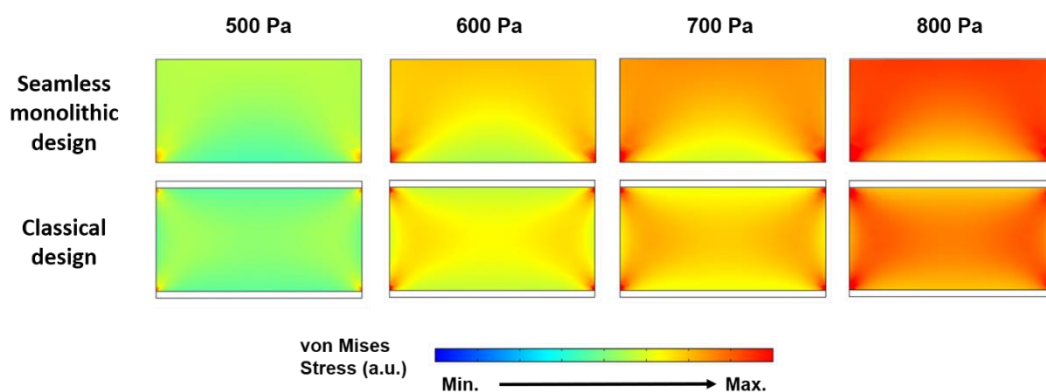
Figure 2.6. FEA simulation results of von Mises stress distribution results of the monolithic design (top) and classical design (bottom) under compressive loads of 500, 600, 700 and 800 Pa.

Sensitivity of a capacitive tactile sensor is defined as $S = (\Delta C/C_0)/\Delta P$, where C_0 is the initial capacitance of the sensor, ΔC is the capacitance change after compression and P is the applied pressure. Figure 2.7 (a) shows the sensitivity of the MCSs and the sensor with classical design. The capacitive sensors with classical design were constructed with a melamine sponge dielectric and separate PET/Ag NW planar electrodes layers with a 250 µm thickness. Sheet resistances of the electrodes of the MCS and the sensor with classical design was set at 10 Ω. Responses of the sensors to various applied pressures ranging from 0 to 10 kPa were measured using a LCR meter and additional loads. Sensitivity of the sensor with classical design was 0.24 kPa^{-1}, whereas, it was up to 1.28 kPa^{-1} (5.3 times higher than classical design) with monolithic design, when the applied pressure was less than 100 Pa. Sensitivity of the sensors were 0.03 kPa^{-1} and 0.10 kPa^{-1} with classical and monolithic designs, respectively, when the pressure was applied up to 10 kPa. The monolithic capacitive sensors with PDMS overcoats were also tested as shown in Figure 2.7 (b). Capacitance change of the capacitive sensor under compressive stress was directly

related with the stiffness of the structure. Stiffness of the melamine sponge was found to increase with increasing PDMS overcoat amount as evidenced by the compression test results provided in Figure 2.8. Therefore, sensitivities of the fabricated sensors tend to decrease with increasing PDMS amount, yet still higher than that of the classical design.
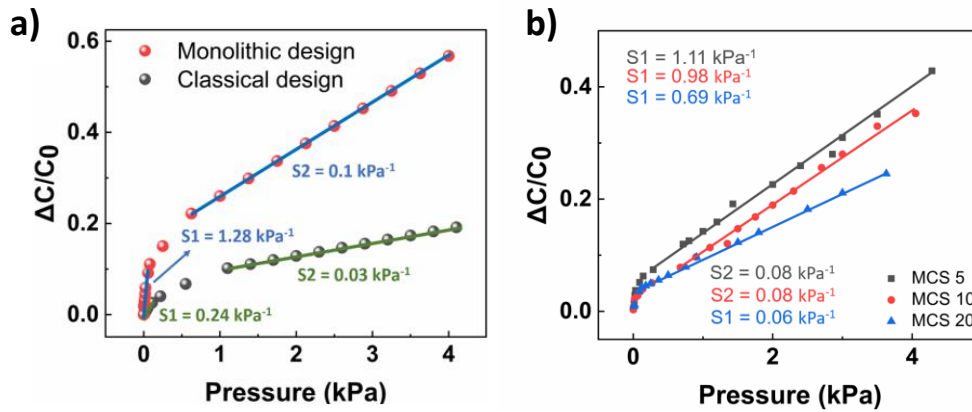
Figure 2.7. Sensitivities of the fabricated capacitive pressure sensors. a) Sensitivity comparison of the monolithic design (MCS 0) and sensor with a classical design. b) Sensitivities of MCS 5, MCS 10 and MCS 20.
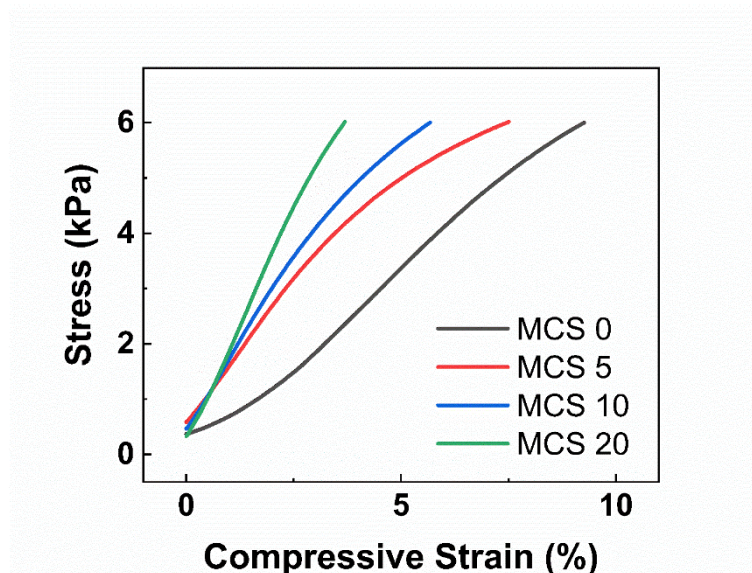
Figure 2.8. Compression test results for the fabricated MCSs.

Small weights were sequentially placed onto the fabricated sensors and capacitive responses of MCSs were measured and provided in Figure 2.9 (a). A reduction in the relative capacitance was observed just before the weights were placed onto the sensors. These reductions were due to the fringed electric fields as the hands approach. A remarkable change in capacitance (0.5%) was observed when a pressure of 0.5 Pa was applied to the MCSs. Additional weights placed on the fabricated sensors caused further increase in the relative capacitance. The MCSs successfully detected pressures of 0.5 Pa, 0.75 Pa, 1.13 Pa, 1.38 Pa and 3 Pa. Response/recovery times are also important parameters for the pressure sensors. As shown in Figure 2.9 (b), a 110 Pa of load was applied carefully to the MCSs to measure the response/recovery times, which were obtained as 18 ms and 53 ms, respectively. These were highly comparable to the response time of the human skin (between 30 – 50 ms)[87]. Foam-like materials necessitate some time to recover their original shape upon pressure application. This eventually leads to differences in response and recovery times. Recovery ability of a foam depends on several factors including degree of crosslinking, foam cellular structure (open or closed cell) and interconnection of the skeleton [53,54]. It is known that foams with closed cell structure recover back quickly due to squeezed air bubbles [54]. In contrast, melamine foam has an open cell structure. Under compressive loads, air squeezes out from the structure and does not make any contribution to recovery process. Therefore, recovery time of the melamine foam with open cell structure was expected to be slower. The performance of the fabricated MCS and the sensors with porous dielectric layers obtained from the literature were compared in Figure 2.9 (c) in terms of sensing performance. Fabricated MCSs in this work clearly outperform the others with its sensitivity and response time.

Although the sensitivities of the fabricated monolithic sensors slightly decrease upon PDMS overcoating, their stabilities under cyclic mechanical stimuli improved significantly. PDMS was cross-linked on the Ag NWs and the melamine foam, which resulted in a strong physical bonding amongst them. Effects of the PDMS overcoat on the stability performance of the fabricated sensors were tested upon repeated

compressive force cycles. MCS 0 (without PDMS overcoat) and MCS 5 (the lowest amount of the PDMS overcoat) were exposed to 1 kPa cyclic compression. The MCS 5 maintained excellent stability through 42 000 cycles as shown in Figure 2.9 (d).

The PDMS overcoat on the melamine foam showed a wrinkled structure. It was demonstrated in literature that melamine foam a with PDMS overcoat shows hydrophobic behavior due to wrinkled structure of the overcoat[45]. The fabricated MCSs with the PDMS overcoat cannot be wetted by water and in fact they float over the water. Therefore, additional weights were attached to the MCSs with PDMS overcoat to immerse them into water for the washing test. The washing stability of the fabricated MCSs was tested in water under a mechanical agitation of 400 rpm for 30 minutes at room temperature. The MCSs were dried after each washing cycle and subjected to capacitance measurements. Washing stabilities of the sensors were demonstrated as relative capacitance change. Capacitance values of the corresponding sensors before washing cycles were taken as base capacitance values. The measured capacitance values after each washing cycle were subtracted from the base capacitance value and the output was divided by the base capacitance value to observe change in capacitance characteristics of the tested sensors. The change in capacitance upon washing for MCS 0, MCS 5, MCS 10 and MCS 20 are shown in Figure 2.9 (e). The measured change in capacitance for the MCS 0 began to decline immediately after the first washing cycle. This was due to the release of Ag NWs from the melamine foam, which resulted in an increase in the surface resistance of the electrode. On the other hand, MCSs with PDMS overcoat showed excellent washing stability. No change in the relative capacitance values were registered for the mentioned sensors after 10 washing cycles. This was due to strong physical bonding between the Ag NWs, melamine foam and the PDMS. As mentioned before, capacitance characteristics of the capacitive sensor was closely related with the surface resistance of the electrode layers. Therefore, any change in the electrode resistance can affect the device characteristics and any deterioration in the electrode structure degrades the capacitive response. Resistances of the PDMS overcoated

electrodes did not change remarkably even after 10 washing cycles, as shown in Figure A.1.

Wearable electronics are expected to be used for all day long. Therefore, air permeability is an important parameter for the user comfort. Seamless monolithic design of the sensor allowed structure to preserve its porosity and air permeability. Figure 2.9 (f) demonstrate the porosity of the MCS, where smoke uninterruptedly travels through the sensor. To test air permeability, parafilm, a cotton fabric and MCS 20 were employed to cover the water containers with 10 g DI water. One of the containers was un-sealed and used as the reference sample. During the test, average air temperature and relative humidity were noted as 25.6 °C and 25%, respectively. The weight of each sample was measured each day to detect the amount of evaporated water. As shown in Figure 2.9 (g), the container covered with the MCS demonstrated a very similar water evaporation rate as the reference sample and the fabric. However, for the container covered with the parafilm, the amount of water remained constant.
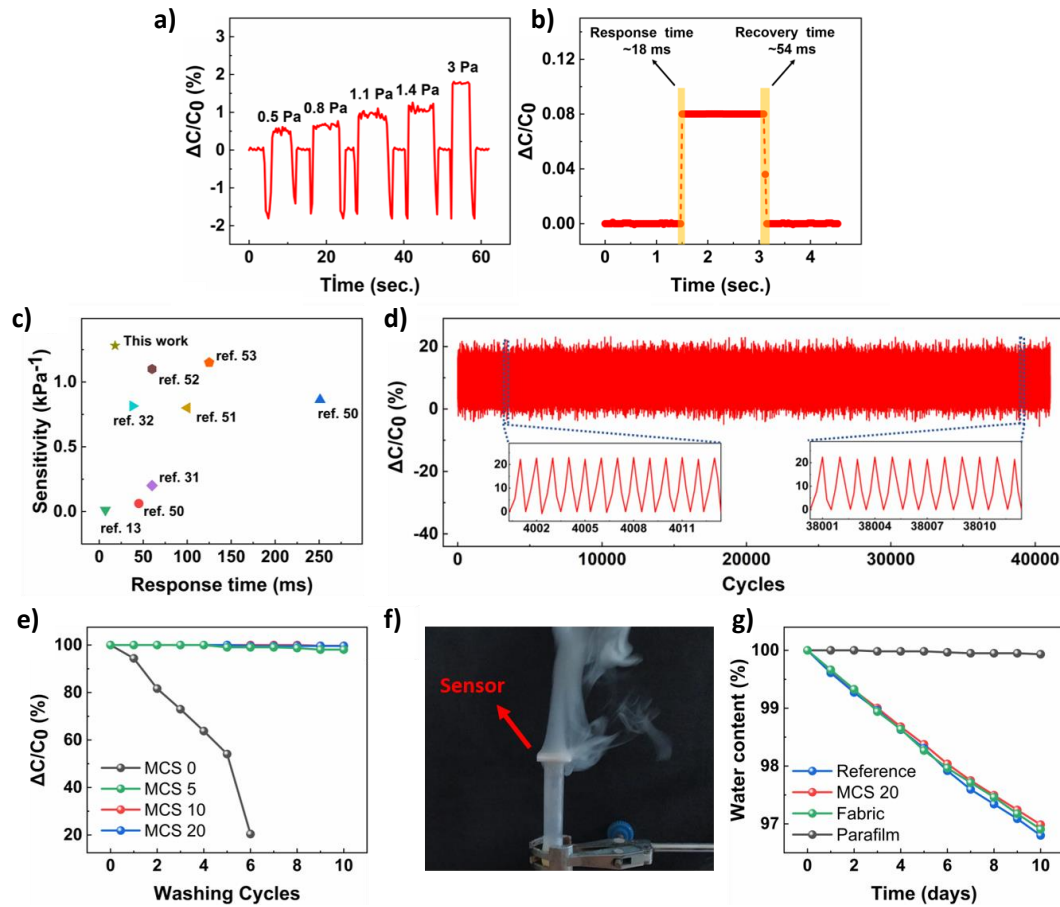
Figure 2.9. The performance of the fabricated capacitive sensors. (a) Responses of the MCS under small compressive stresses. b) Response of the MCS to 110 Pa pressure c) Comparison of the performance of recently published capacitive sensors having dielectric layers with randomly distributed pores. d) Response of the MCS 5 under 1 kPa cyclic compressive pressure for 42 000 times (the insets show the localized response of the MCS under cyclic compression test at the beginning and at the end of the test). e) Washing stability test of the MCSs. f) Photograph showing travel of smoke through a fabricated MCS sitting on a sealed tube. g) Relative mass change of the water in the container sealed with MCS 20, cotton fabric and parafilm at 25.6 °C and 25 % relative humidity.

2.3.3 Physiological Signal Monitoring

High sensitivity, mechanical durability, washing stability and excellent air permeability make MCSs a promising candidate to be used as real time physiological signal recognition. To demonstrate possible applications, MCSs were placed at different locations on human body to detect various physiological signals. A large muscle biceps, lies between the shoulder and the elbow on the front upper arm. Main function of the biceps is to flex the elbow and supinate the forearm. Figure 2.10 (a) shows that the real-time relative capacitance changes during the movement of biceps. Change in the muscle volume when biceps were partially contracted in supinated position and fully contracted in the supinated position were detected with the fabricated sensor by the relative capacitance change. The MCS was also attached above the wrist to detect the movement of the wrist, as shown in the Figure 2.10 (b). Bending of the wrist caused the capacitive sensor to be also bended and change the distance between the electrode layers. Relative change in the capacitance is totally dependent on the bending angle of the wrist. The wrist was bent around 30 °, 60 °, 90 °, 60 ° and 30 ° degrees, respectively. Before each bending, wrist turned back to its original un-bent condition. The MCS gave the same response to the same bending angles. These results imply that the proposed sensor can be used to precisely detect bending angles of the wrist by the relative capacitance change. The MCSs were placed on front arm to detect movement of a muscle group named forearm flexor, which is responsible for moving fingers. As shown in Figure 2.10 (c), the fabricated sensor can immediately respond to the muscle movement. The response of the sensor was found to depend on how hard the fist was clenched. In the hard clenched fist, contraction amount of the muscle is higher compared to that in gentle clenched fist. Therefore, relative capacitance change was higher in hard clenched fist.

In addition to aforementioned applications, fabricated sensors are suitable for detecting small changes in the body, due to its high sensitivity, fast response and low detection limit. Patients can suffer from complete motion loss, in case of diseases like amyotrophic lateral sclerosis (ALS) or paralysis. In such cases, communication

with the environment, which is a basic need, is one of the biggest difficulties of patients. The detection of eye blinking can be a solution to this problem. In order to demonstrate the potential, fabricated MCSs were placed to the corner of the eye to detect eye blinking. During eye closing the sensor was exposed to a compressive stress. The MCS gave a quick and sharp response to blinking as a result of this compressive stress. The signals of the repeated blinking were successively monitored and provided in Figure 2.10 (d). In addition, the MCS was attached to the cheek on the lateral pterygoid, which is the main muscle responsible for opening of the mouth. Our intention here was to monitor motions and vibrations of the mouth during speaking so that MCSs may be used for real-time speech detection. As can be seen from Figure 2.10 (e), the fabricated sensor detected various pronounced words. The change in the relative capacitance was recorded when the word sequence "middle east technical university" and the words "sensor", "breathable" repeated several times. The unique features in the response curves that occur during pronunciation can be used for the detection of various words.

The proposed sensor was also placed onto the knee joint to detect flexion of the leg, as shown in the Figure 2.10 (f). Extreme deformation was registered in the sensor during the flexion of the leg. A relative change around 12 times in the capacitance of the sensor was detected. After each flexion cycle, the capacitance of the sensor was found to recover. This means that the signals of the relative changes were highly reproducible under the continuous flexion and relaxation of the leg. This result also proved the extraordinary stability of the fabricated MCSs.

All these results imply that, the MCSs can be used in real time monitoring of the wide range of body motions in extreme conditions like excessive bending, compression and twisting. Thanks to high air permeability, very low weight and high washing stability, proposed sensor is suitable for long term use without disturbing the user comfort. In addition, due to high sensitivity, low detection limit and high response time the fabricated sensor can be used for early diagnosis of the diseases or helps people who suffer from several diseases like ALS or paralysis.
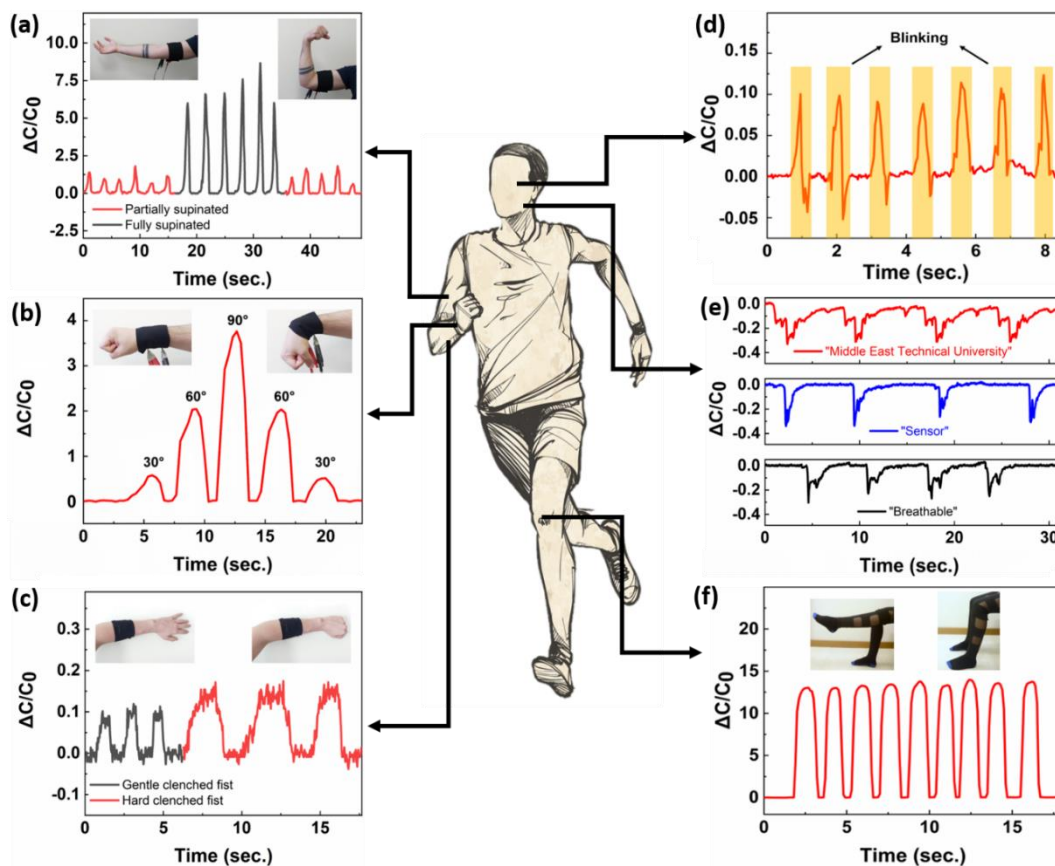
Figure 2.10. Physiological signal monitoring with the fabricated MCSs. a) Responses of the MCSs to movement of the muscle group named biceps. The different responses given by the muscle group under partially and fully supinated positions were detected by the fabricated MCS (the insets show the photograps of biceps in relaxed and fully supinated positions). b) Relative capacitance changes when then the wrist was bent 30, 60, 90, 60 and 30o, respectively (insets show the photographs of wrist in its normal and 90o bent positions). c) Response of the sensors to clenching of fist, when placed on the forearm flexor muscle group. Sensor gave different responses to gentle and hard clenched fist (insets shows the photograph of the hand in open and closed positions). d) Response of the MCS to blinking, when the sensor was placed at the eye corner. e) The MCS placed to the cheek and the sensor gave response to voice because of the created vibrations and muscle movements. f) Response of the MCS to flexion of the leg (the insets show the photographs of the leg in relaxed and flexed positions).

42

2.3.4   Proximity Detection

With the recent advancements, capacitive sensors started to be prominent members of the daily life. They have a wide range of application areas from gesture recognition to human machine interface[63,64]. In addition to tactile information systems, capacitive sensors can also be used as un-touched object or human position detection. There is a capacitive coupling between people, objects and electronic devices. Thanks to this capacitive coupling, it is possible to make an estimation about the relative positions of the objects. Electric field between the electrodes are fringed as a function of distance between approaching object and the electrodes when an object approaches the capacitive sensors. Approaching object acts as a grounded conductor and electric field lines complete their path through the object. Because of the fringing electric field, measured capacitance of the capacitive sensor decreases. Base capacitance of the sensor can be measured without proximity. The measured capacitance value of the MCS started to decrease when distance between approaching object and the MCS was below 20 cm. The hand was stopped 20, 15, 10, 5, 3 and 1 cm away from the MCS, respectively. As can be seen from Figure 2.11 (a), the shorter the distance between the hand and MCS, the smaller the measured capacitance value. Continuous hand movement in the proximity of the MCS was also performed and results are presented in Figure 2.11 (b). The MCSs demonstrated reversible change in the relative capacitance when the movement of the hand alternated between just above the detection limit to 1 cm away from the MCS.
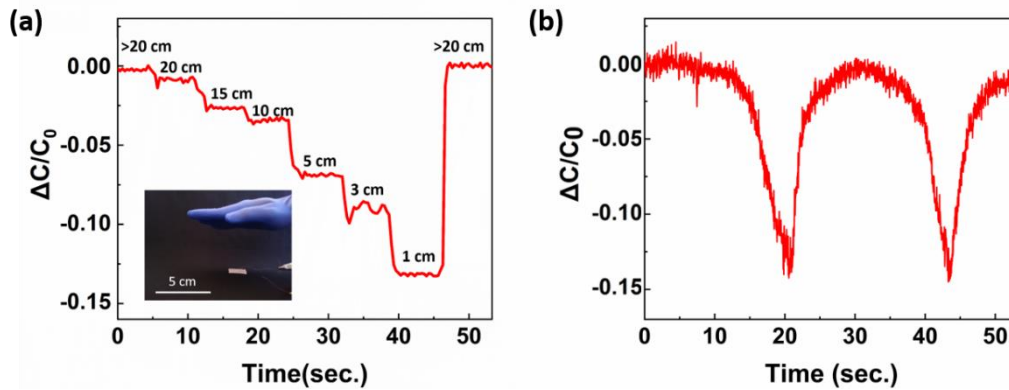
Figure 2.11. Proximity detection performace of the MCSs. a) Measured relative capacitance change when distance between the hand and the MCS was changed. The distances between hand and the MCS were 20,15, 10, 5, 3 and 1 cm, respectively (the inset shows the hand above the fabricated MCS). b) Response of the MCS when the hand continuously moved between just above detection limit and 1 cm.

2.4 Conclusions

Proposed method in this work, allowed fabrication of seamless monolithic structures on a highly porous foam using a cost effective and easy way. Overall density of the fabricated parallel plate capacitive sensors was extremely low due to the absence of the additional layers and bulk metals. Another advantage of the seamless monolithic structure is the elimination of interfacial problems between layers such as delamination and mechanical instability. In addition to foam-like materials, developed method can be used to obtain seamless monolithic structures on fabrics. Therefore, proposed method has a potential to bring a new perspective to the field of wearable electronics.

CHAPTER 3

SUPRAMOLECULAR BIO-POLYMER GEL BASED IONTRONIC SENSORS WITH RECORD BREAKING SENSITIVITY FOR OBJECT RECOGNITION FROM TACTILE FEEDBACK

3.1   Introduction

The rapidly developing robotic industry, human-machine interface devices, and wearable electronics necessitate pressure sensors to be more compact, sensitive, and flexible with a user-friendly design. [54,69,75,91,92]. Therefore, increasing the sensitivity of devices while maintaining flexibility and ease of use becomes the primary concern of today's pressure sensors. Many types of pressure sensors are developed to convert mechanical input from the environment to electrical signals, including triboelectric[93], capacitive [94], resistive [95], and iontronic pressure sensors [96]. Among them, iontronic pressure sensors received much attention for their extremely high sensitivity and fast response [35]. Electrode polarization-dependent electrical double layer (EDL) formation at the surface of electrodes allows iontronic pressure sensors to achieve very high areal capacitance values under applied pressure. Moreover, the high areal capacitance value in iontronic pressure sensors makes the parasitic effects of the environment negligible, improving the quality and resolution of the measured data. These aspects of the iontronic sensors make them ~10 000 times more sensitive than capacitive pressure sensors [44,97].

While iontronic pressure sensors hold great potential, further development and performance improvement requires a deep understanding of their working principles. To date, plenty of design strategies has been developed to enhance the sensitivity of the iontronic pressure sensors. Patterning of the electrodes and iontronic layers and the use of stacked iontronic layers are a few of these strategies [98–101]. Xiao et al. used micropatterned multilayer structure of poly(vinylidene fluoride-co-

hexafluoropropylene)(P(VDF-HFP))-gel as iontronic layer with Au electrode layers to acquire a pretty remarkable sensitivity over a long linear range. The effect of the multilayer structure on mechanical response was investigated [98]. Bai et al. employed an intrafillable architecture for poly(vinyl alcohol)/phosphoric acid (PVA/H_3PO_4) gel as iontronic layer with Au electrodes and obtained a high sensitivity (671.7 kPa^{-1}) and investigated the behavior of the intrafillable layer under mechanical deformation [99]. Moreover, a remarkable sensitivity (31.1 kPa^{-1}) for iontronic pressure sensors based on ionic liquid droplets stacked between the top floating graphene electrode and bottom graphene grid was reported by Kim et al. [101]. However, in-depth investigation of the iontronic sensors from an electrochemical perspective is limited in the literature [44,102–104].

The working mechanisms of the iontronic pressure sensors and the supercapacitors have some similarities [105]. The principles of obtaining high sensitivity from an iontronic pressure sensor and storing large amounts of charge in supercapacitors are similar. Their performances are determined by the electrochemical characteristics of the electrodes and electrolyte materials. On the other hand, the prospects for satisfactory performance are different for an iontronic pressure sensor and a supercapacitor. Supercapacitors are generally designed to work under static conditions. Their primary purpose is to store as much charge as possible without sacrificing fast charge/discharge kinetics [106]. Therefore, for conventional supercapacitor design, the mechanical performance of components under dynamic conditions is not among the leading design concerns. This allows the use of gel electrolytes or liquid electrolytes with various mechanical properties. [107]. On the other hand, an iontronic pressure sensor design is more complex. Besides electrochemical performance, high mechanical stability is another critical parameter that determines the performance of iontronic pressure sensors. Therefore, the active layers of the sensors should be designed accordingly.

A comprehensive study is conducted to develop and characterize a novel, ionically conductive supramolecular bio-polymer gel (SBPG) structure with structural integrity and state-of-art iontronic pressure sensors are fabricated. The sensing

behavior of iontronic pressure sensors is evaluated in detail from an electrochemical perspective. SBPG structure is developed based on hydroxyethyl cellulose (HEC), glycerol and sodium chloride (NaCl). Glycerol – HEC ratio is critical in determining the structural and electrochemical characteristics. The ideal gel composition for the iontronic pressure sensor is evaluated based on the electrochemical and mechanical properties of the gel. The developed supramolecular bio-polymer gel structure is microtextured using sandpaper and then used as a dielectric layer for the sensors. In addition, 3-D Bode and 3-D areal capacitance analyses are used to understand the sensing mechanism of the iontronic pressure sensors and the spatial relationship between the layers with the applied pressure. Fabricated sensors are then used to fabricate smart gloves with tactile object recognition, revealing their potential for the next-generation human-machine interface devices.

3.2   Experimental Procedure

Materials Characterizations

All characterizations are conducted at 25°C and 30% relative humidity, unless otherwise specified.

SEM (FEI NOVA NANO SEM 430) is used for the morphological characterization of the patterned SBPG layer and the carbon-based electrode layers at an operating voltage of 20 kV.

3D surface topography of the patterned SBPG layer is determined by Huvitz HRM 300 optical microscope.

For X-Ray diffraction (XRD) analysis of the SBPG layers, a Rigaku Ultima-IV system with Cu Kα radiation (0.154 nm) is used at a scan rate of $2°$ min^{-1}.

FTIR analyses are conducted via ATR unit of the spectrometer (Bruker Alpha Platinum spectrometer) with a resolution of 2 cm^{-1} and 64 scans in the range of 400-4000 cm^{-1}.

Thermogravimetric Analysis (TGA) is conducted via Exstar SII TG/DTA 7300 with a temperature increment rate of 10 °C min^{-1}.

Rheological characterization of as-prepared SBPGs is realized utilizing oscillatory tests. All the tests are performed with a rheometer (Anton Parr, MCR 102) equipped with a parallel plate geometry (diameter of 25 mm) with a gap of 0.4 mm. Frequency sweep tests are conducted to investigate the frequency dependency of storage (G') and loss modulus (G") under 1% strain at angular frequency values between 0.6 and 3140 rad.s^{-1}.

Surface resistance measurements of the carbon electrodes are conducted using a four-point probe station (Signatone Pro-4).

Electrochemical tests are conducted using symmetric stainless-steel electrodes within Swagelok cells. HP 4194a Impedance/Gain-Phase Analyzer is used to conduct electrochemical measurements between 100 Hz and 15 MHz. SBPG samples with a thickness and diameter of 400 μm and 8 mm are used for electrochemical characterizations, respectively.

Measurements are made with four different samples from different batches for each SBPG stoichiometry.

Sensor Characterization

Twintex LCR-7200 is used for the characterization of the sensors. Test frequency is set as 1 kHz for all measurements conducted under 25°C and 30% relative humidity conditions. PCE-DFG N digital dynamometer is used to detect the applied pressure to the sensor unless otherwise specified.

Measurements are made with four different sensor samples from different batches for each SBPG stoichiometry.

Fabrication of the Mold for Patterning

A sandpaper with the grit size of 188 is used. PDMS base and curing agent are mixed in a ratio of 10:1. The prepared solution is poured onto the sandpaper and cured at

90°C for 30 minutes. After curing, PDMS is carefully stripped from the sandpaper and used as a negative mold for patterning the SBPG layer.

Fabrication of the SBPG Layers

Hydroxyethyl cellulose (HEC, Sigma Aldrich, average molecular weight ~ 380 000) is added to DI water and stirred vigorously at 80°C. 2.6 ml of DI water is used to dissolve each 0.1 g of HEC. After obtaining a clear solution, the specified amount of NaCl (Merck) is added to the solution (if the layer contains NaCl) and stirred at 80°C for 30 minutes. Finally, a certain amount of glycerol is added to the solution and stirred vigorously for 6 hours to obtain a homogeneous mixture. Before pouring the solution into the molds, the solution is rested at room temperature for 1 hour to eliminate the air bubbles. Following the elimination of bubbles, a specified amount of the solution is poured into the molds and placed into a furnace at 90°C for 12 hours. At the end of the fabrication process, the thicknesses of the SBPG gels are determined as 400 μm.

SBPG solution is poured onto the previously prepared negative PDMS mold to get sandpaper textured SBPG layer for the iontronic pressure sensor. Afterwards, it is placed into a furnace at 90 °C for 12 hours.

Fabrication of Carbon-Based Electrodes

Carbon-cellulose electrodes are prepared via simple solution mixing and doctor blading methods. 1 g of HEC is added to 20 ml of DI water and dissolved under magnetic stirring at 80 °C. Once a clear solution is obtained, 0.5, 1, and 1.5 g of CB are added slowly to ensure a homogeneous mixing and left at stirring overnight to obtain a homogeneous suspension. Then, 1 g of glycerol is added to the suspension and further stirred at 80°C for at least 2 hours to obtain an ink-like suspension. Before casting, the prepared suspension is ultrasonicated for 1 hour to ensure a homogeneous casting. Afterwards, prepared ink-like suspension is cast onto glass substrates via the doctor blade method with a wet thickness of 300 μm. Glass substrates are previously washed with acetone, ethanol, and DI water and treated

with a high-frequency spark generator to obtain a hydrophilic surface. Casted films are dried under ambient conditions overnight and peeled off to obtain flexible, self-standing carbon-cellulose films as the electrodes. Finally, fabricated carbon electrode sheets are cut into the desired shapes using a marking laser (FiberLAST-NanoMark Energy Series (10 W, 1064 nm wavelength, 100 ns pulse length, speed: 100 mm s^{-1}).

Fabrication of the Iontronic Pressure Sensor

The fabricated sensors are composed of four main elements: substrates, carbon-based electrodes, SBPG iontronic layer, and spacers. PET substrates with a thickness of 70 µm and an area of 1.25 cm x 1.25 cm are used as the substrate for the sensor. The carbon-based electrodes with an area of 0.5 cm x 0.5 cm are glued onto the PET substrates using a PDMS-curing agent mixture. 1:10 ratio of PDMS-curing agent mixture is prepared, well-mixed, and applied onto the PET substrate. After curing the PDMS layer in an oven at 90°C for 30 minutes, electrode layers, PDMS, and the PET substrate are found to adhere firmly to each other. Prepared SBPG layer placed on the bottom electrode. 1.5 mm thick VHB tape is placed on the edges of the PET substrates, which served as a spacer.

Fabrication of the Smart Gloves

Previously fabricated, eight different t-C-1:10:0.1s are placed onto specific locations of the knitted glove. Conductive threads are used for the sensor connections.

3.3   Results and Discussions

Supramolecular polymer gels are used extensively in supercapacitors[108,109] and batteries[110,111]. These structures show great potential for electronics of the future. However, there are still ongoing debates on the supramolecular gels' structural integrity for proper shaping and ionic conductivity [112]. Consequently, there are limited number of studies on supramolecular gels for sensory units [113–115]. To demonstrate the potential of iontronic sensors, a fully biocompatible supramolecular

bio-polymer gel based on HEC, glycerol, and NaCl was developed. Detailed fabrication route of the SBPG is provided in the Experimental Procedure section.

Stoichiometry of the supramolecular bio-polymer gel directly affects its chemical, mechanical, and electrochemical properties, as shown in Figure 3.1. Complexation triggered by hydrogen bonding between the HEC chains, and the glycerol molecules occurs instantaneously upon mixing the solution. Excess HEC chains in the solution increase structural integrity and the number of conduction pathways. Yet, it decreases the segmental motion ability of the overall structure, meanwhile lowering the ionic conductivity. In contrast, excess glycerol increases the chain mobility, resulting in a very low structural integrity and reduction of conduction pathways, adversely affecting the ionic conductivity. Ultimately, the "ideal" structure offers admirable structural integrity to be used under dynamic conditions and possesses high ionic conductivity due to the ions' adequate number of conduction pathways.
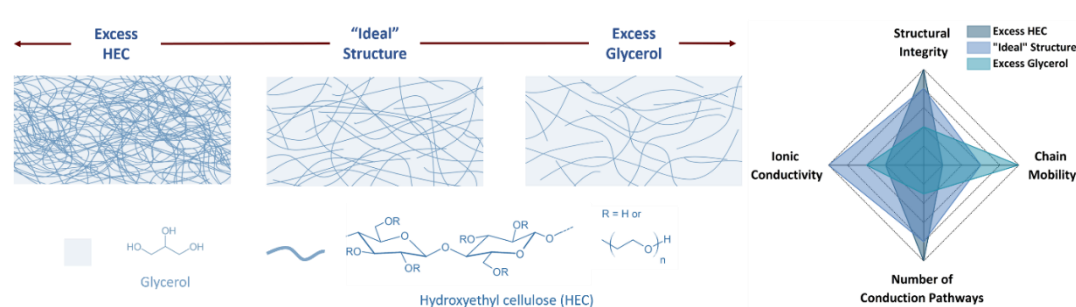
Figure 3.1. Schematic models of the SBPGs based on HEC-glycerol complexation with excess HEC, ideal structure, and excess glycerol. Line fill graph compares their properties in terms of structural integrity, ionic conductivity, number of conduction pathways, and chain mobility.

3.3.1 Characterization of SBPG

The stoichiometry of SBPGs is controlled by keeping the amount of glycerol constant and varying the amounts of HEC and NaCl. Ratios of the gels are provided in Table 3.1. SBPG characterizations are conducted in two parts. Firstly, the ideal HEC and glycerol stoichiometry is determined and then the effects of ion addition is

observed. Complex impedance spectroscopy analysis, the areal capacitance measurements, XRD analysis, FTIR, oscillatory rheometry, and TGA are conducted to understand the structure of the SBPGs.

Table 3.1. Stoichiometric ratios of the SBPGs (For simplicity, amounts of constituents are normalized to the glycerol ratio).

SBPG Notation (HEC-Glycerol-NaCl)	*HEC Ratio*	*Glycerol Ratio*	*NaCl Ratio*
SBPG 1:5	20	100	-
SBPG 1:10	10	100	-
SBPG 1:15	6.67	100	-
SBPG 1:20	5	100	-
SBPG 1:10:0.1	10	100	1
SBPG 1:10:0.2	10	100	2
SBPG 1:10:0.3	10	100	3
SBPG 1:10:0.4	10	100	4
SBPG 1:10:0.5	10	100	5

Electrochemical characterization of SBPGs is crucial in understanding the structure. Two stainless steel electrodes are used throughout the electrochemical characterizations of the SBPGs. Impedance spectroscopy is conducted between 100 Hz-15 MHz, and results are provided in Figures 3.2 (a) and (b). A low-frequency spike corresponds to the electrode polarization formed between SBPG and electrode, and the low-frequency end of the semi-circle indicates the bulk resistance[116]. Indication of the bulk resistance value enables the calculation of ionic conductivity using the Equation (3.1) [117]:

$$\delta = \frac{1}{R_b}\frac{d}{S} \quad (3.1)$$

,where δ is ionic conductivity (S cm^{-1}), R_b is bulk resistance (Ω), d is the thickness of the film (cm), and S is the contact area (cm^2).

Ionic conductivity in polymeric structures highly depends on the mobility of the polymer chains [118,119]. Therefore, it is expected to get higher ionic conductivity from the samples with higher chain mobility. However, in our case, even though the segmental motion of HEC chains continuously increased with the glycerol ratio, ionic conductivity reached its peak (7.72 x 10^{-5} S cm^{-1}) when the stoichiometric HEC:glycerol ratio approached 1:10. It then decreased gradually, as can be observed in Figure 3.2 (c). Therefore, SBPG 1:10 is referred to as an "ideal" structure. This finding demonstrated that the HEC chain forms conduction pathways for the charges. These results support the idea that increasing the HEC ratio increases the number of conduction pathways, while decreasing chain mobility and reducing ionic conductivity. In the case of excess glycerol, the segmental motion of the HEC chains is high; however, the absence of conduction pathways results in moderate ionic conductivity values.

In this context, the effect of ions on the conductivity is investigated over the ideal structure. NaCl is added as an ion source in a controlled manner at the stoichiometric ratios provided in Table 3.1. The ionic conductivity is found to increase gradually from SBPG 1:10:0.1 to 1:10:0.3 and take the value of 9.85x10^{-4} S cm^{-1}. However, after this point, the increase in salt content adversely affected the ionic conductivity and the conductivity decreased to 6.92x10^{-4} S cm^{-1} (Figure 3.2 (d)). The relatively low conductivities at lower salt concentrations can be attributed to the relatively low number of free ions in the structure. Further increase in the salt concentration had a detrimental effect on the ionic conductivity, which can be attributed to three main causes: 1) High salt concentration might hinder complete salt dissociation. XRD measurements showed that SBPGs have an amorphous structure. Two amorphous humps are observed in the XRD patterns at 21° and 36° (Figure 3.3 (a)). Moreover, the addition of NaCl did not change the amorphous nature of the structure. The

absence of NaCl peaks in the XRD pattern demonstrate complete dissolution of the NaCl in the structure (Figure 3.3 (b)). Therefore, this cause is not valid for our case. 2) Strong interaction between ions can cause ion cluster formation and offset the increase in ion density[120]. 3) Consumption of the number of vacancies required for ion transport [121]. Overall, the detrimental effect of the increased NaCl amount needs to be investigated further.
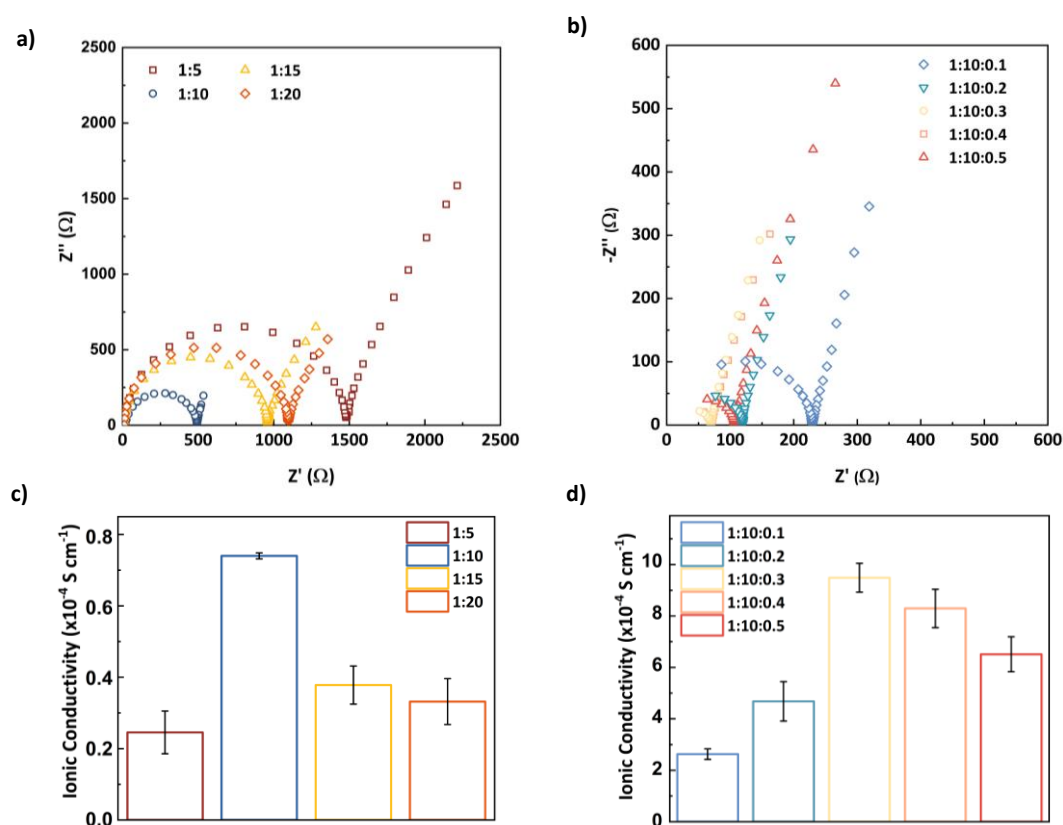
Figure 3.2. Electrochemical characterization of the fabricated SBPGs. Nyquist plots for the SBPGs a) without and b) with NaCl. The frequency range of the measurements was set to 100 Hz – 15 MHz. Ionic conductivities of the fabricated gels c) without and d) with NaCl.
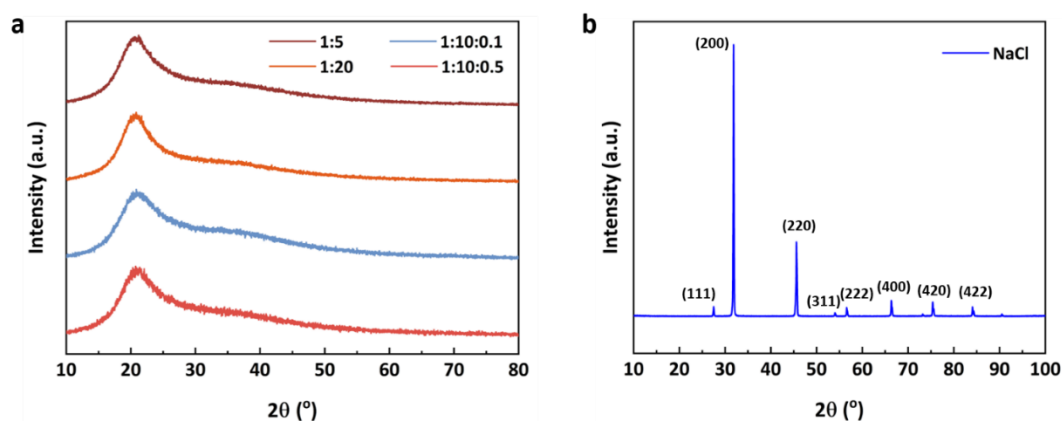
Figure 3.3. a) XRD plots for SBPG-1:5, 1:20, 1:10:0.1 and 1:10:0.5. b) XRD plot for NaCl.

The broadband areal capacitance measurements are conducted for the SBPGs (Figure 3.4 (a) and (b)), and values are found to strictly depend on the stoichiometries of the SBPGs, which are in line with the ionic conductivity measurements. The maximum areal capacitance value of 2 μF cm^{-2} at 100 Hz is obtained for the SBPG 1:10 (Figure 3.4 (a)). Alteration of the HEC ratio from the ideal structure decreases the areal capacitance. NaCl addition, on the other hand, considerably improves the areal capacitance (Figure 3.4 (b)). The highest areal capacitance value is obtained as 12 μF cm^{-2} at 100 Hz for the SBPG 1:10:0.3. A further increase in the NaCl ratio decreases the areal capacitance.
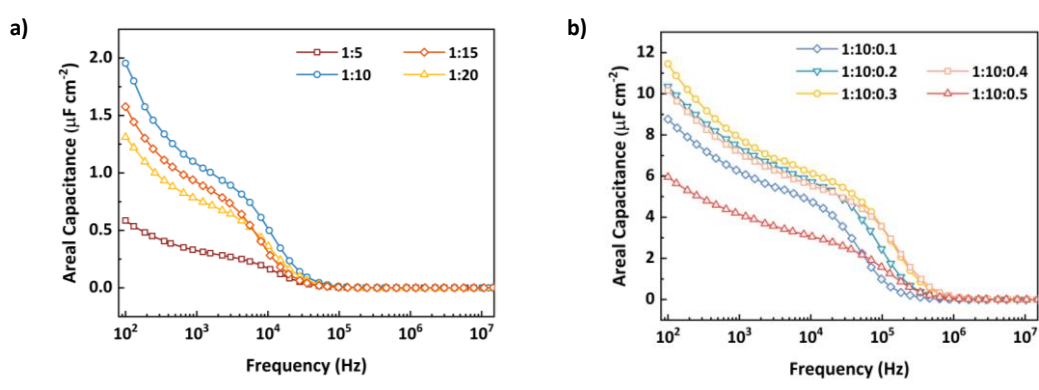
Figure 3.4. Areal capacitance results of the SBPGs a) without and b) with NaCl.

It has been observed that the areal capacitance values of the SBPGs directly depend on the test frequency (100 Hz - 15 MHz). This frequency-dependency can be explained by "electrode polarization" or "Maxwell-Wagner-Sillars interfacial polarization"[122]. HEC moieties, glycerol molecules, and ions are spatially randomly distributed in the structure and are aligned according to the electric field. There is enough time for the alignment and travel of the ions over macroscopic distances at low frequencies[123]. However, they cannot align under the rapidly changing electric field at higher frequencies. So, the only contribution to the areal capacitance comes from the dielectric properties of the material-specific molecules.

FTIR analysis is performed to better understand the chemical structure of SBPGs. Spectra between 2600 and 4000 cm^{-1} are provided in Figure 3.5 (a). Three peaks are observed in this range. The broad peaks around 3280 cm^{-1} belong to the vibration peak of the hydroxyl groups, representing hydrogen bonding in the structure. As shown in the graph, a gradual increase of the HEC ratio brings about a shift of the peak positions through the higher wavenumbers (from 3276 to 3282 cm^{-1}) . Shifts in FTIR peaks upon concentration changes prove the intermolecular interactions between HEC chains and glycerol molecules, supporting supramolecular gel formation. Furthermore, the absence of the sharp, free OH stretching peak in the FTIR spectra at high wavenumbers [124,125] indicates that all the hydroxyl groups of the glycerol and HEC chains physically interact with each other.

Two peaks between wavenumbers of 2800-3000 cm^{-1} are assigned to CH_2 symmetric-asymmetric vibrations of the glycerol[126]. Moreover, three consecutive peaks at 1210, 1325, and 1410 cm^{-1} indicate the glycerol moieties assigned to CH deformation vibrations and CH_2 bending, respectively (Figure B.1) [127,128]. Positions of these peaks remained constant despite the changes in the HEC ratio of the gel. This indicates the formation of a three-dimensional network through self-assembly. H-bonds between the hydroxyl groups of the glycerol molecules and the HEC chains are responsible for this formation.

Effects of NaCl addition are also investigated. The FTIR peaks indicate that CH deformation vibrations, and CH_2 bending (at 1210, 1320, and 1410 cm^{-1}, respectively, Figure B.2 (a) and CH_2 symmetric and asymmetric vibrations (at 2879 and 2933 cm^{-1}, respectively, Figure B.2 (b), remain unchanged following the addition of different amounts of an inorganic salt into the structure. Therefore, it can be suggested that there is no complex formation between the ions and glycerol on methylene end groups. On the other hand, several studies have shown that the cations in the solution disrupt the previously formed hydrogen bonds within the structure by competitive hydrogen bonding[129–131]. The addition of NaCl to the structure causes the OH stretch peaks to shift towards higher wavenumbers, evidencing the disruption of the H-bonds between the HEC chains and glycerol molecules Figure B.2 (b). Competitive H-bonding between Na^+ ions and the HEC chain may replace glycerol molecules.

TGA is conducted to determine the thermal behavior of the SBPGs. Results are provided in Figure 3.5 (b) and (c). The thermal stability of the structure is affected by the HEC: glycerol stoichiometry. The small glycerol molecules fit between HEC chains. They form H-bonds between the HEC chains and decrease the strength of the intermolecular bonds. Thus, SBPG 1:5 show the highest thermal stability among other stoichiometries due to the highest HEC:glycerol ratio.

TGA results can provide further information about the macromolecular structure of the gels. Figure 3.5 (b) shows two distinct weight loss regions for SBPG 1:5 and 1:10. First weight loss, between 90-150 °C, is attributed to the removal of the physically bonded H_2O and other volatile small molecules from the structure. The second loss corresponds to the thermal decomposition of the HEC-glycerol supramolecular structure. These results manifest that a well-developed single-phase HEC-glycerol supramolecular structure can be formed with high homogeneity.

On the other hand, for the SBPG 1:15 and 1:20, one more decomposition step is apparent between 230-270 °C. Glycerol molecules are bonded to hydroxyl moieties of the HEC chain during the 3-D network formation. The number of hydroxyl

moieties of the HEC chain decreases with the HEC: glycerol ratio decreasing below the ideal stoichiometry. In this case, glycerol molecules may start to form glycerol islets independent of the HEC-glycerol complex due to a lack of binding sites. As the HEC: glycerol ratio decreases further, the tendency of the glycerol molecules to form individual islets becomes more favorable, and these islets act as separate glycerol phases. Moreover, the absence of the free hydroxyl peak in the corresponding FTIR spectra supports the notion that the excess glycerol molecules tend to form glycerol islets as a secondary phase rather than remain unbound in the structure Figure B.2 (b). Then, these additional decomposition steps can be attributed to the decomposition of glycerol islets.

The addition of NaCl to the structure also alters the thermal behavior. Three different decomposition steps are observed in Figure 3.5 (c). This three-step thermal decomposition gets started for SBPG 1:10:0.2 and becomes more prominent with the gradual increase of the NaCl ratio. As suggested earlier, Na^+ ions may disrupt intermolecular interactions between the HEC chains and the glycerol molecules through the competitive hydrogen bonding. These results in the replacement of the glycerol molecules, as suggested by the TGA analysis. While the first and the final weight loss are related to the physically bonded H_2O, volatile small molecules, and the HEC-glycerol supramolecular structure, second weight loss starting with SBPG 1:10:0.2 is related to the glycerol islets. These results indicate that the addition of NaCl to the system induces glycerol molecules to form discrete islets as a secondary phase.

Viscoelastic behavior of the gel structures is evaluated with the help of rheometry results of which are provided in Figures 3.5 (d) and (e). As shown in the graphs, in general, G' values are greater than G" values for all the samples within the investigated frequency range. Results indicated a gel-like behavior for all the samples [132]. Initially, SBPGs without NaCl are tested, and the results showed that increasing the glycerol content simultaneously decreased G' and G". In a physically connected 3D network, G' is driven by the difficulty of the segmental motion of the polymer chains. An increase in the HEC concentration in the structure increases the

probability of chain entanglement, increasing the storage modulus. Therefore, it is reasonable to suggest that decreasing HEC: glycerol ratio causes an increase in the mobility of the polymer chains. This behavior can be attributed to the interaction between glycerol molecules and the functional groups of the HEC chains. Glycerol weakens the intermolecular interaction of HEC and increases the inter-chain distance of hydroxyl groups by occupying free spaces between the polymer chains[133]. Therefore, the chain mobility of the polymer increases by the weakening of the intermolecular interaction between HEC chains.

Moreover, a gradual decrease of the storage modulus is observed by adding ions. The presence of inorganic salts is known to increase the segmental motion of the polymeric chain and destabilize the three-dimensional network[134]. As mentioned earlier, Na^+ ions disrupt the intermolecular interactions between glycerol molecules and HEC chains, increasing the separation between them and displacing a portion of the bonded glycerol molecules. The displaced glycerol molecules then form glycerol islets as a secondary phase. These findings also support the TGA results of the SBPGs. Therefore, the dissolution of the NaCl has a plasticizing effect by inhibiting the hydrogen bond induced complexation between glycerol molecules and HEC chains. This inhibition increases the free volume of the structure and segmental motion of the chains.

Structural integrity and shaping capability of the SBPGs are shown in the photographs provided in Figures 3.5 (f) and (g). Thanks to their structural integrity, SBPG 1:5 and 1:10 have successfully preserved their 3-dimensional shapes. However, this does not apply to SBPG 1:15 and 1:20. It is observed that the pawns produced with these gels tend to lean forward as they do not have the necessary mechanical properties to withstand. The addition of NaCl showed detrimental effects on structural integrity and shaping capability. As suggested before, the addition of the NaCl forces glycerol to form small islets. This leads to a release of glycerol molecules from the HEC backbone, and a decrease in the storage and loss modulus (Figure 3.5 (e)). As Figure 3.5 (g) shows, it is no longer possible to shape the gels with an increase in the amount of glycerol released (SBPG 1:10:0.5).
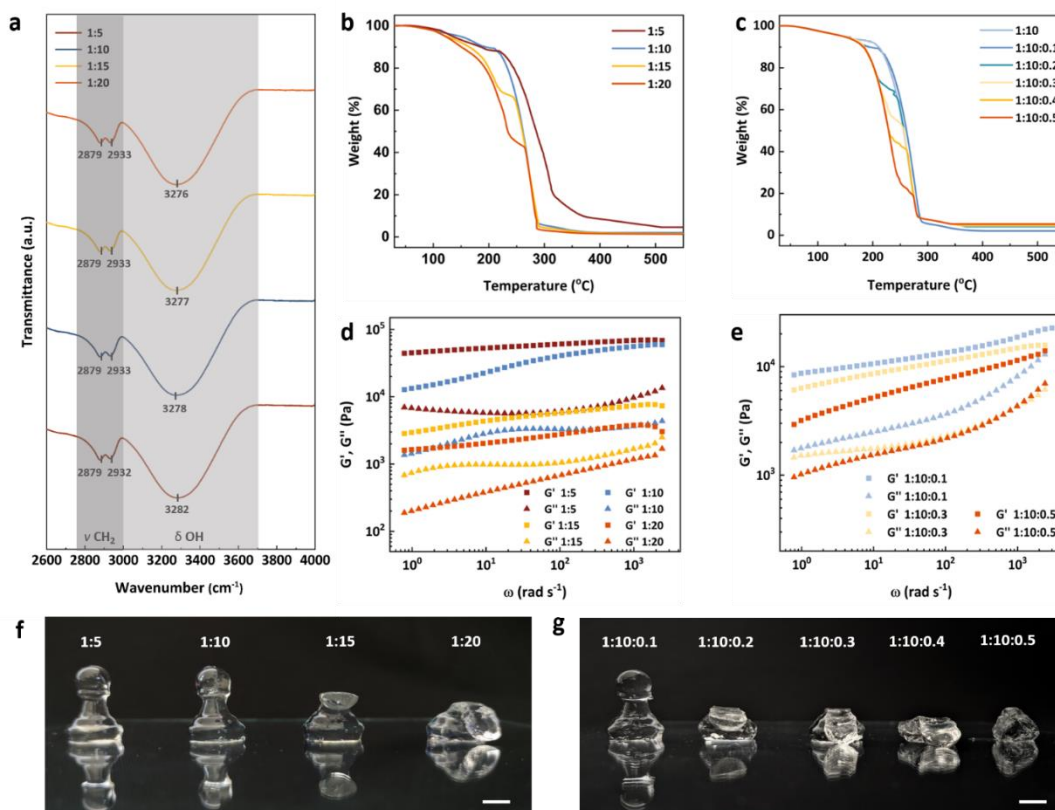
Figure 3.5. Chemical characterization of the developed SBPGs. a) FTIR spectra of the SBPG (1:5, 1:10, 1:15, and 1:20) in the range of 2600-4000 cm^{-1}. The darker region indicates the -CH$_2$ vibration peaks, while the peaks in the lighter region give information about the OH stretching of the structures. TGA results of the structures b) without and c) with NaCl. OR results of the SBPGs d) without and e) with NaCl. f) Photos of 3D-pawn-shaped SBPGs without NaCl (left to right: SBPG 1:5, 1:10, 1:15, and 1:20). g) Photos of 3D-pawn shaped SBPGs with NaCl (left to right: SBPG 1:10:0.1, 1:10:0.2, 1:10:0.3, 1:10:0.4 and 1:10:0.5).

3.3.2   Characterization of Iontronic Pressure Sensor

SBPGs with optimized structural integrity, ionic conductivity, and areal capacitance enabled the production of state-of-art iontronic pressure sensors with record sensitivity. The sensors are operated in touch mode capacitive sensing, which was developed by Ko and co-workers[135,136]. In this architecture, the upper electrode layer

is separated from the dielectric layer of the structure. The hierarchical structure of the pressure sensor is provided in Figure 3.6 (a-i). The schematic shows four main parts of the sensor: substrate, spacer, carbon-based electrode layers, and textured SBPG as the dielectric layer.

Carbon-based electrodes ae composed of carbon black (CB), HEC, and glycerol. Carbon black provides electrical conductivity to the structure; the HEC chains form the backbone of the structure and provide structural integrity to the layer. Glycerol molecules provide flexibility. The effect of the CB composition (HEC:glycerol: CB) on the surface resistance of the electrode layers is provided as a bar chart in Figure B.3. The figure shows that increased CB to HEC ratio from 0.5 to 1.5 decreases the structure's resistance from 680 ± 230 to 95 ± 4 Ω sq^{-1}. However, further increasing the amount of CB deteriorates the electrode's integrity by disrupting the molecular interaction between HEC chains. Therefore, electrode layers with a CB to HEC ratio of 1.5 are used in the experiments. Detailed information about the fabrication process is provided in the Experimental Procedure section. Electrodes with the same composition are used to fabricate the sensors. A laser marking device is used to cut the electrodes into desired shapes.

Carbon-based electrodes are attached to PET substrates with PDMS. SBPG layer is directly placed on the attached electrode layer, and the upper electrode layer is placed on top of the bottom electrode with a spacer in between. A VHB tape is used as a spacer and sealed the structure. Detailed information on the fabrication procedure is provided in the Experimental Procedure section. A photograph of the finalized iontronic pressure sensor is given in Figure 3.6 (a-ii).

Separators provided additional benefits in addition to their intended use in touch-mode capacitive pressure sensors[136]. Firstly, the supramolecular structure of the dielectric layer forms a sticky outer layer due to the presence of dynamic H bonds. Immediately after the touch of these layers, dynamic H-bonds are formed between the upper electrode and the dielectric layers. Therefore, an opposing force is required to separate the two adjacent layers to obtain reproducible responses. Here, the role

of the spacer is to supply this required opposing force to the system by acting as a spring. Second, the sensor achieved record sensitivity using a separator. The sensitivity of the capacitive sensors is calculated using the following equation (3.2):

$$S = \frac{(\delta C/C_0)}{\delta P} \text{ (3.2)}$$

As shown by the formula, initial capacitance (C_0) is very important in determining the sensitivity of the device. Therefore, a low initial capacitance can be considered as the main strategy to achieve high sensitivity values. The separator enabled the system to possess a very low initial capacitance. Initial capacitances of the identically prepared iontronic pressure sensors are measured as 2.30 ± 0.11 pF. Such low initial capacitance values allowed the sensors to reach record sensitivities.

Firstly, iontronic pressure sensors that consist of SBPG-1:5, 1:10, and 1:15 are fabricated using carbon-based electrodes with the following notations C-1:5, C-1:10, and C-1:15, respectively. Un-textured SBPG layers are also used to test the sensitivity without introducing additional parameters. Their sensing behaviors are provided in Figure 3.6 (b). The low structural integrity of SBPG 1:20 prevented it from being used as an iontronic layer for the sensor. Among the sensors tested in the first stage, the C-1:10 had the highest sensitivity in the second and third linear regions. In the first linear region, the sensitivities of the sensors are measured as equal to 0.122 ± 0.0014 kPa^{-1}. All in all, electrochemical measurements of the SBPG and the sensitivity of the fabricated iontronic pressure sensors confirmed the direct relation between ionic conductivity, areal capacitance, and sensitivity. The highest ionic conductivity from the SBPGs without salt is obtained from SBPG-1:10 is complemented with the highest areal capacitance value, ultimately resulting in the best sensitivity for the iontronic pressure sensor (Figure 3.6 (b)).

The effects of adding NaCl to SBPG on sensor performance are also investigated. SBPG 1:10:0.4 and 1:10:0.5 could not be tested because of their low structural integrity. Pressure sensing behaviors of the fabricated sensors are provided in Figure 3.6 (c). As mentioned earlier, sensitivities in the first region for different SBPG

samples are the same and equal to 0.122 ± 0.0014 kPa^{-1}. The highest sensitivity values for second and third linear regions are measured from C-1:10:0.3 as 1 393 997 and 147 959 kPa^{-1}, respectively. The sensitivity values for all the tested SPBG combinations are tabulated in detail and provided in Table 3.2.

Table 3.2. Sensitivities of the fabricated pressure sensors.

Sensor Notations	Region I sensitivity (kPa^{-1})	Region II sensitivity (kPa^{-1})	Region III sensitivity (kPa^{-1})	Region IV sensitivity (kPa^{-1})
C-1:5	0.120	94 593	24 379	-
C-1:10	0.123	281 544	63 229	-
C-1:15	0.122	158 065	49 764	-
C-1:10:0.1	0.121	558 001	119 973	-
C-1:10:0.2	0.120	952 888	136 311	-
C-1:10:0.3	0.123	1 393 997	147 959	-
t-C-1:10:0.1	0.124	565 514	1 475 000	304 017
t-Al-1:10:0.1	0.123	1033	2032	217

The effect of the dielectric layer morphology on the sensitivity is also evaluated. For this purpose, sandpaper is used as a mold to texture the SBPG layer. The detailed procedure is provided in the Experimental Procedure section. Adhesive nature and insufficient structural integrity prevented successful texturing of SBPG 1:10:0.3. The same problem also hindered the texturing of SBPG 1:10:0.2. Successful patterning is only achieved for the SBPG 1:10:0.1. SEM images of the patterned gel and its 3D morphology are shown in Figure B.4. (a) and (c). Iontronic pressure sensor with the textured dielectric layer (t-C-1:10:0.1) showed the highest sensitivity among the other fabricated sensors (Figure 3.6 (d)). Unlike the three distinctive sensing regions of SBPG layers without texturing, t-C-1:10:0.1 had four distinct sensing regions. Capacitance change in the first region is the same as before, related to the closure of the gap between the upper electrode and the dielectric layer. The sensitivities of the

other regions are measured as 565 514, 1 475 000, and 304 017 kPa^{-1}, between 4 to 8 kPa, 8 to 14 kPa, and 18 to 35 kPa, respectively. Although the ionic conductivities of SBPG 1:10:0.2 and 1:10:0.3 are higher than that of SBPG 1:10:0.1, it is observed that the sensor made with textured SBPG 1:10:0.1 has the highest sensitivity. This is due to the significant increase in surface area upon texturing [99]. The detailed sensitivity values for all tested SPBG combinations are provided in Table 3.2.

In order to find out the role of electrode material on the sensitivity, a pressure sensor with the textured SPBG layer (t-C-1:10:0.1) is fabricated using an Al-foil electrode (t-Al-1:10:0.1) rather than the carbon-based electrodes. Plot showing the relative capacitance changes with respect to applied pressure is provided in Figure 3.6 (e). Compared to the iontronic pressure sensor t-C-1:10:0.1, t-Al-1:10:0.1 gives 725 times lower sensitivity (Figure 3.6 (f) and Table 3.2). As shown in Figure 3.7 (a) and (b), the carbon-based electrodes have a rough surface. The roughness of the electrode increased the surface area, which allowed an enhanced EDL formation between electrodes and the SBPG layer, causing an improved areal capacitance and sensitivity (Table 3.2). These results demonstrated that the electrochemical characteristics (ionic conductivity and areal capacitance) of the dielectric layer and the electrode materials are essential in determining the sensor response. At this point, the iontronic pressure sensor is similar to supercapacitors. The performance of the supercapacitors also relies on the electrochemical characteristics of the active layers.
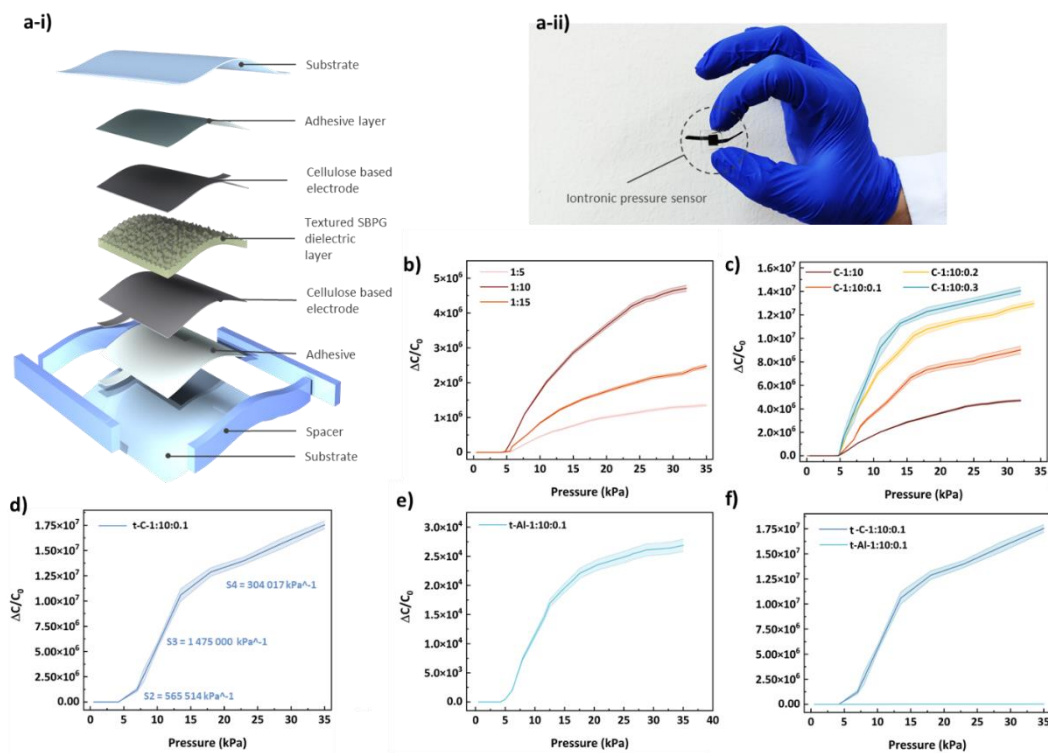
Figure 3.6. Characterization of the fabricated iontronic pressure sensor. a-i) Schematic of a stacked layer of the fabricated iontronic pressure sensor. a-ii) Photograph of the finalized structure of the sensor. Scale bar: 1 cm. b) Relative capacitance changes of the C-1:5, C-1:10, C-1:10:0.2 and C-1:15 with respect to applied pressure. c) Relative capacitance changes of the C-1:10, C-1:10:0.1, C-1:10:0.2 and C-1:10:0.3 with respect to applied pressure. d) Relative capacitance changes of the t-C-1:10:0.1 with respect to applied pressure. Calculated sensitivity values are provided in the figure.
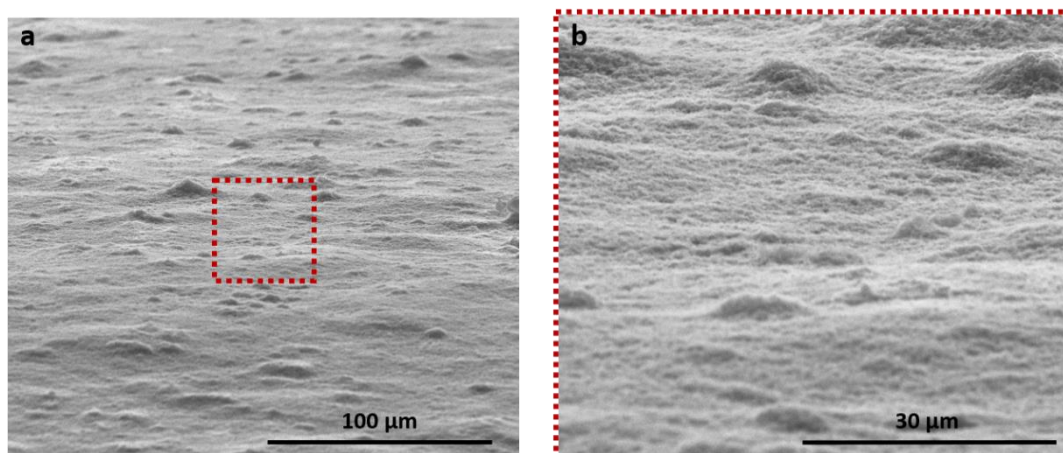
Figure 3.7. SEM images of the C-electrode under a) low and b) high magnifications.

Response and recovery characteristics of the sensor under 7 kPa pressure are provided in Figure 3.8 (a). From this graph, the response and recovery times of the sensor are calculated as 80 and 48 ms, respectively. This indicates that the sensor quickly responds and returns to its original position. Relative capacitance changes of the fabricated sensor under repeated pressures are provided in Figure 3.8 (b). The mechanical stability of the sensor is tested through 5000 compression cycles under a pressure of 12 kPa (Figure 3.8 (c)). As can be seen, highly stable and proportional responses are registered from the fabricated sensors. The inset figures show the sensor's response at the beginning and at the end of the cycles. Indistinguishable responses proved the robustness of the sensor under cyclic compression.
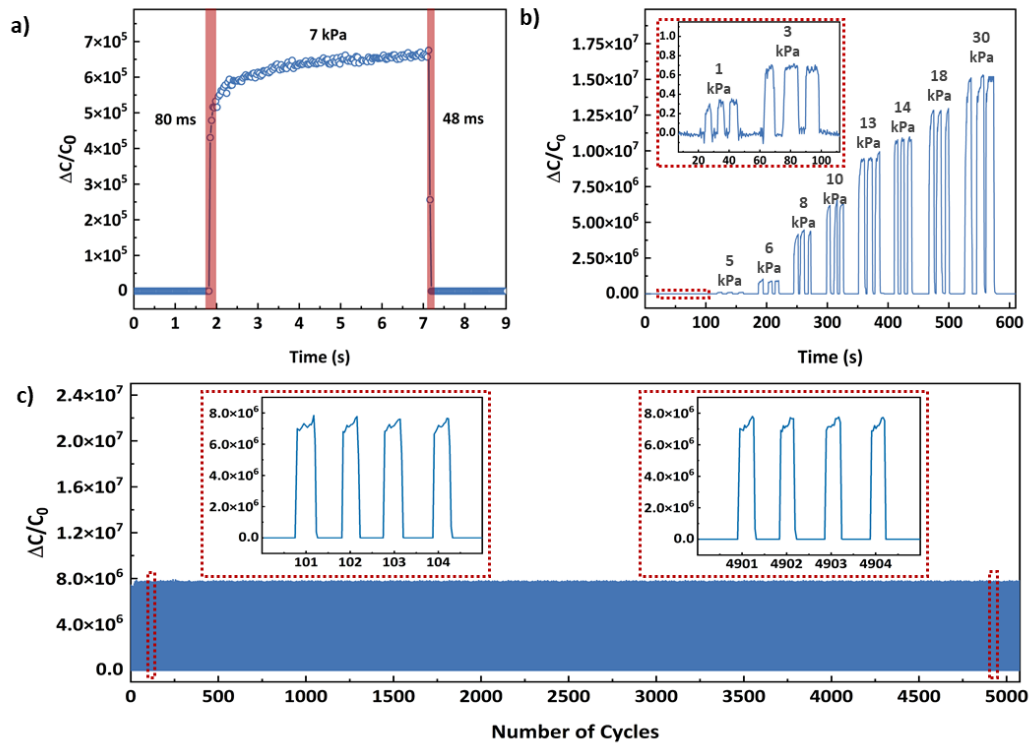
Figure 3.8. a) Response and recovery times of the t-C-1:10:0.1 under 7 kPa of pressure. b) Relative capacitance changes of the t-C-1:10:0.1 under various pressures. c) Capacitance change of the t-C-1:10:0.1 under 12 kPa of cyclic compression.

One of the essential features of the SBPG-based iontronic pressure sensor is its high sensitivity. This record high sensitivity also enabled the sensor to successfully sense very small pressure changes. Responses of the sensor to applied various minimal pressures under 8 kPa are provided in Figures 3.9 (a) and (b). Glass slides are used to apply 8 kPa compression to the sensor. The response of the sensor to three different feathers (that were 10, 20, and 20 mg independently measured by the balance (Axis AGN 220C), with their corresponding pressure values of 1, 2, and 2 Pa) is provided in Figure 3.9 (a). Insets show a photograph from the measurement and zoomed-in sensor response. As shown by the inset, the placement of lightweight materials on the pressure sensor caused a stepwise and steady increment in the

capacitance change. These results showed that the fabricated iontronic pressure sensor can be used to successfully resolve pressures as low as 1 Pa.

Performance of the sensor under relatively high-pressure changes is also recorded. Following the application of 8 kPa pressure with the help of glass slides (Figure 3.9 (b), two equally weighted transistors (0.5 g = 50 Pa), a bigger transistor (1 g = 100 Pa), and a feather (10 mg = 1Pa) are gently placed on the sensor. Response of the sensor is provided both in Figure 3.9 (b) and its inset. A stepwise increase in the capacitance change is observed after placing each object. Moreover, the stable response of the sensor through the test period proved the successful recognition of the low and moderate pressures. These results demonstrated that the fabricated sensor can successfully detect a wide range of pressure changes.
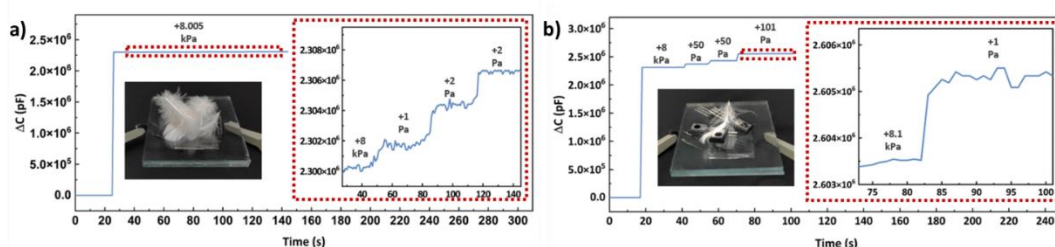
Figure 3.9. a) Response of the sensor to 8.005 kPa. The inset graph shows the variation in the relative capacitance after placing feathers on the sensor. Inset shows a photograph of the sensor when three feathers are placed on the glass slides, applying 8 kPa pressure to the sensor. b) Response of the sensor to 8 kPa, 50, 50 100, and 1 Pa applied pressures. The inset graph shows the variation in the relative capacitance after applying feather weighted 10 mg to the sensor, which was previously under 8.1 kPa of pressure. Inset shows a photograph of the sensor while various weighted objects are placed.

3.3.3 Pressure Sensing Mechanism

For the first time in the literature, 3D Bode and 3D areal capacitance analyses over a broad frequency (100 Hz - 15 MHz) and pressure (0 - 35 kPa) ranges were employed. They provide a comprehensive understanding of the sensing mechanism

and the spatial relation between the active layers (electrode and dielectric layers). It is demonstrated that the iontronic pressure sensor with a textured dielectric layer possesses four different linear sensing regions. These regions are highlighted in Figure 3.10 (a) and can be observed more clearly. Illustrations of the iontronic pressure sensor's conditions in specific regions are provided in Figure 3.10 (b).

In Region I (up to 4 kPa), the spacer forms an air gap between the upper electrode and the textured dielectric layers. The air gap creates an "electrode blocking layer," preventing ion-induced charge accumulation on the electrode-dielectric interface. This means that the electrode polarization is bypassed, resulting in a drastically low initial capacitance. Effects of the electrode blocking layer can be observed in the 3D Bode analysis (Figure 3.10 (c)). The graph shows that up to 4 kPa, negative phase angle of the sensor is almost equal to 90°, implying ideal capacitive behavior. The fabricated sensor in this region operates as a classical capacitive pressure sensor. The capacitance change solely depends on the decrease in the distance between the electrode layers and an increase in the effective dielectric constant of the system due to air squeezed out of the structure [94]. A few pFs of capacitance and relatively low-pressure sensing capability in Region I can be attributed to this behavior. The 3D areal capacitance analysis additionally proves the behavior. The measured areal capacitance value remains stable over a wide frequency range (Figure 4 (d)). However, when the frequency exceeds 4 MHz, the measured areal capacitance value decreases because of the dielectric relaxation.

Region II (between 4 and 8 kPa) is the transition region. This is the region where the operating mechanism of the sensor evolves from classical capacitive to iontronic sensing. The upper electrode and the ionically conductive dielectric layers start to touch each other, meaning that the electrode blocking layer disappears, allowing ion-induced electrode polarization and related EDL to occur. Frequency dependency of the areal capacitance proves EDL formation in this region (Figure 3.10 (d)). Moreover, one can make interpretations about the spatial condition of the upper electrode and the dielectric layer by looking at the low-frequency response of the sensor. At the beginning of Region II, the absolute value of the phase angle is

measured as 6° at 100 Hz, meaning that the system contains both resistive and capacitive elements. The illustration of the spatial position of the layers at 100 Hz is given in Region II. Air gaps remain between the upper electrode and the textured dielectric layer. The remaining air gaps give capacitive characteristics to the system, while the contact points of the upper electrode and the textured dielectric layers make a resistive contribution. As the applied pressure increases, the interfacial area between the textured dielectric and upper electrode layers increase, gradually consuming the air gaps [35,99]. The consumption of the air gaps causes the capacitive contribution to decrease gradually. Change in the absolute value of the phase angle from 6° to 0.2° validates this condition at the low-frequency region (Figure 3.10 (c)). In this region, the capacitive behavior becomes prominent with an increase in the frequency, indicating that the structure is composed of a parallel combination of capacitance and resistance at low frequencies.

Region III begins right after the complete elimination of the air in the structure. A gapless contact between the upper electrode and the dielectric layers forms in this region. Following complete contact between the two consecutive layers, the device shows a resistive behavior that can be understood from 3D Bode analyses. The sensor's phase angle remains almost constant from the beginning of Region III to the end of Region IV, which is 0.2° at low frequencies and increases with the frequency, as shown in Figure 3.10 (c).

In Regions III and IV, a stepwise increase in the pressure causes mechanical deformation of the textured dielectric layer. Therefore, the thickness of the layer decreases, increasing the measured areal capacitance value throughout the test frequency range (Figure 3.10 (d)). The amount of thickness change due to pressure is the main parameter that determines the capacitance change in these regions.
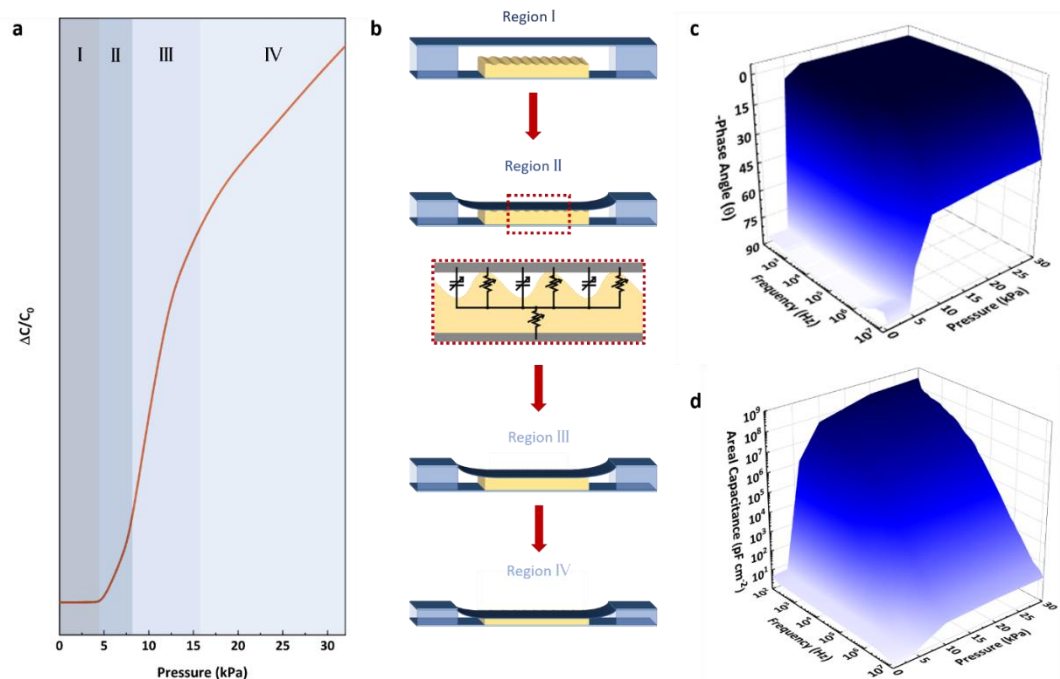
Figure 3.10. The sensing mechanism of the fabricated iontronic pressure sensors. a) A schematic showing the relative capacitance changes with applied pressure on the sensor. b) Illustrations of the sensor and the spatial relation between active layers in Region I, II, III and IV. c) 3D Bode graph in negative phase angle, frequency, and applied pressure on the sensor. d) 3D areal capacitance graph with respect to frequency and the applied pressure on the sensor.

3.3.4 Smart Gloves

Multiple sensing arrays-based smart gloves are fabricated to prove the versatility of the SBPG based iontronic pressure sensors. High capacitive working range, high sensitivity, and rapid response-recovery times of the sensors allow one to acquire real-time and completely noise-free data. In this way, the small differences in grasping objects can be interpreted.

A smart glove-based piano using eight sensing units is fabricated, as shown in Figure 3.11 (a). Sensing units are placed at the fingertips (except the thumbs) with the help of double-sided tape. Each sensing unit had a specified note (e.g., C, D, E, F, G, A,

B, C). Capacitance change is recorded upon pressing the sensing unit, and then the specified note is played, as shown in Figure 3.11 (b). An external speaker is used to play the note, provided that the change in capacitance reaches a predetermined value upon pressing the sensing unit by the thumb of the user.
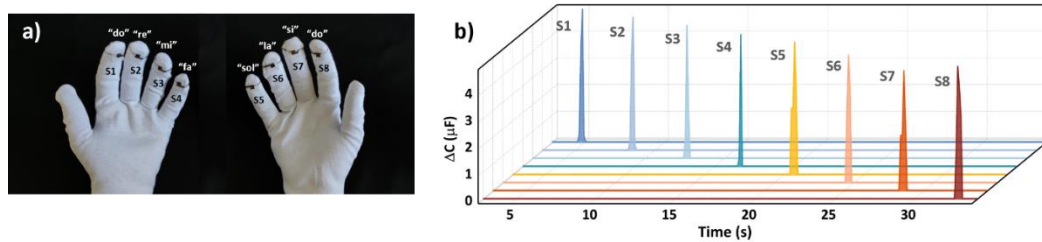
Figure 3.11. SBPG based iontronic pressure sensor for smart gloves. a) Photograph of the smart gloves that enable piano playing. b) Response of the eight different sensor nodes while playing the piano.

The sensitivity of the sensors on the smart glove is further tested in an object recognition experiment conducted with 11 common objects that differed in terms of shape and weight. During each trial, the experimenter grasped each object for a duration of approximately 30 seconds while the pressure readings are obtained at 1.33 Hz. The trials are cut at the onset and the end of each grasp, which produced a recording with average duration of 25.6 seconds (SD=7.19) per object. The final dataset included a total of 376 labeled readings obtained from 8 sensors distributed over the hand. Holding positions and the pressure distribution of the other objects can be observed in Figure 3.12 (a-k).
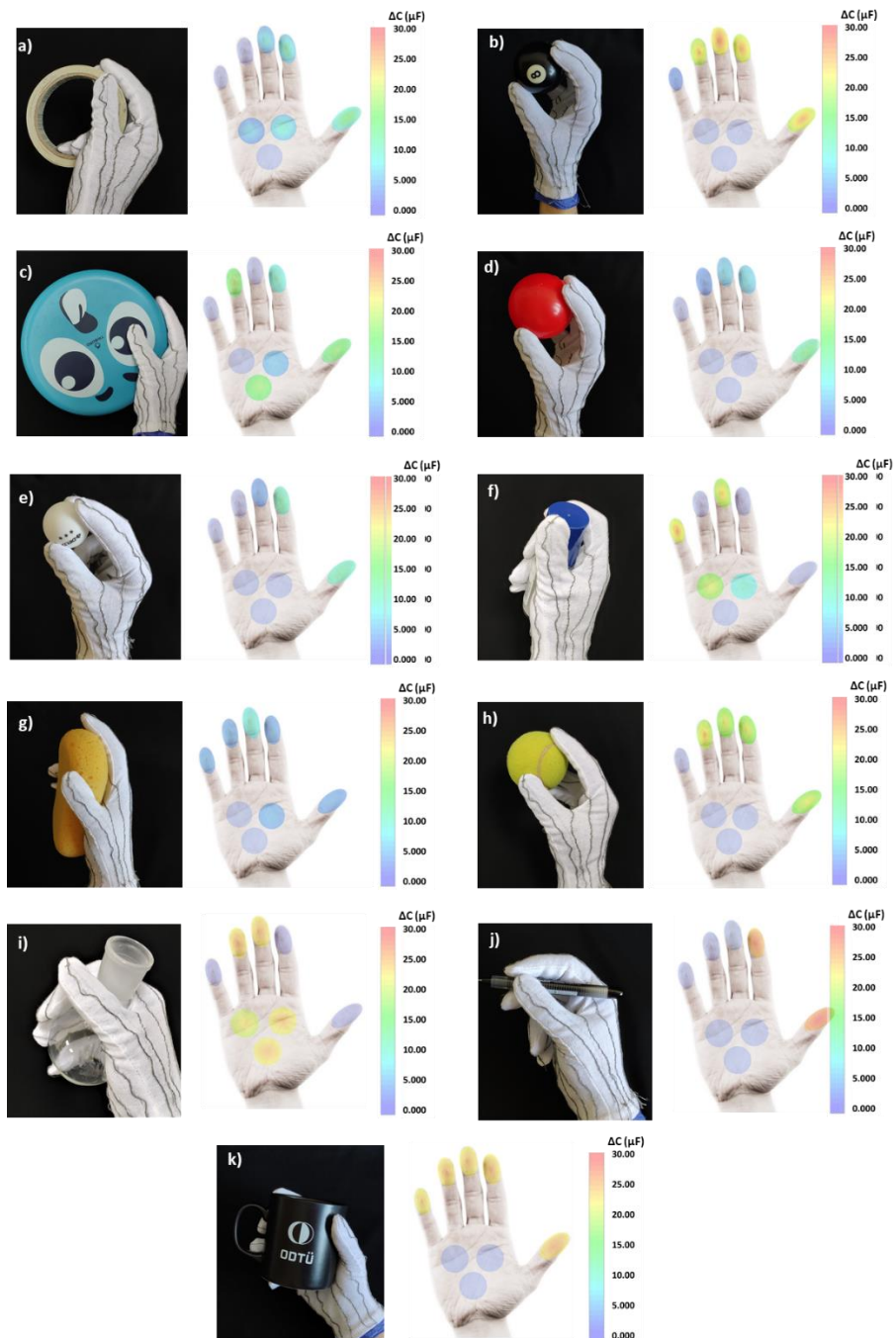
Figure 3.12. Holding positions and the pressure distributions of the measured 11 objects.

Related work on similar object recognition applications with tactile gloves focused on developing a grid of pressure sensors distributed over the hand and treated the pressure distribution obtained for each object as an image. The images are then fed

into deep learning architectures such as Convolutional Neural Nets for classification [59]. In contrast, we developed a tactile glove by using a much smaller grid including only 8 highly sensitive iontronic pressure sensors. Therefore, given the small number of input sources, we opted for training conventional supervised machine learning models, including Naïve Bayes, Support Vector Machines (SVM), k-Nearest Neighbors (kNN), Random Forest, Discriminant Analysis and Decision Tree classifiers. The models are trained by using the MATLAB R2020a Classification Learner toolkit. The data is randomly split into 60%, 20% and 20% chunks for training, testing and validation, respectively. 100 iterations are carried out during hyperparameter optimization with 5-fold cross-validation.

The classification results are summarized in Table B.1 and Table B.2. We obtained around 90% classification accuracy with Random Forest, Decision Tree, SVM and k-NN classifiers. Except for pen and bottle objects, the classifiers could distinguish all 11 objects with high positive prediction values and low false discovery rates (Figure 3.13). This false prediction is related with the contribution of S1 on both bottle and pen predictions of the model. The thin shape of the bottle seemed to cause a similar pressure distribution as compared to the pen, which might have contributed to their mutual confusion. The high sensitivity of the sensors seemed to be especially instrumental in distinguishing four different types of balls (e.g. ping pong, plastic, tennis and billiard balls) that differed in weight. Overall, the high accuracy, precision and recall measures obtained with as little as 8 tactile sensors highlight the potential of this approach for developing tactile sensing applications in human-computer interaction and robotics settings.

Figure 3.13. The confusion matrix for the Decision Forest classifier. The values inside each cell represent the frequency of occurrence of each case (e.g. the column for bottle shows in the 20 instances the model predicted "bottle" as the outcome, 8 of them actually corresponded to a true bottle case, whereas 12 of them were actually pen) during the 5-fold validation phase.

3.4 Conclusions

In this work, the exploration of the dielectric layer of iontronic pressure sensors was under focus. This layer allowed the fabrication of state-of-the-art iontronic pressure sensors. It has been found that the dielectric layers with outstanding electrochemical properties and high stiffness are essential to achieve this high performance. This

improvement provides high-precision accuracy with a limited number of sensors, providing a critical component for object recognition from tactile feedback. SBPG dielectric layers of iontronic pressure sensors are rationally designed using extensive chemical and electrochemical characterization routes. This design strategy can be extended to other electrochemical devices, such as batteries and supercapacitors to achieve unprecedented device performance.

CHAPTER 4

CONCLUSIONS AND FUTURE RECOMENDATIONS

4.1   Conclusions

In this thesis, strategies to enhance sensitivity of capacitive pressure sensors were investigated. Two main different strategies were followed. The first strategy was employing porous dielectric and the electrode layer to get highly sensitive capacitive pressure sensor. The second one was using ionically conductive dielectric layer.

In Chapter 2, a unique 3-D masking technique was proposed for the fabrication of monolithic parallel plate capacitive sensors. Stress distributions under compressive load of the capacitive sensors with monolithic design and the capacitive sensors with classical design were compared using FEA simulations. Owing to the active electrode layers and more homogeneous stress distribution under compressive load, the fabricated capacitive sensors with monolithic design showed 5.3 times higher sensitivity than that of classical design. Moreover, the fabricated monolithic capacitive sensors had very high detection limit, fast response/recovery time, extreme mechanical and washing stability. Thanks to monolithic design, proposed capacitive sensors also possessed high air permeability, which is an important factor in maintaining user comfort during long term use. Benefitting from these features, fabricated sensors can be used for monitoring real-time body motion, detecting voices and proximity of the objects as demonstrated in this work.

In Chapter 3, iontronic pressure sensors with record sensitivity (1 475 000 kPa^{-1}) are fabricated using rationally designed SBPG dielectric layers. Extensive characterizations enabled determination of the ideal HEC: glycerol: NaCl ratio in fabricating SBPGs with an ionic conductivity of 9.85×10^{-4} S cm^{-1}. The working mechanism of the iontronic pressure sensors under dynamic pressures are interpreted with 3D Bode and areal capacitance analyses and their relations are thoroughly

explained. Iontronic pressure sensors are used in smart gloves for object recognition from tactile feedback. Unprecedented sensitivity allowed a prediction accuracy of 90% to be achieved using only eight sensing units.

4.2   Future Recommendations

In this thesis, strategies to increase sensitivity of the capacitive pressure sensors were discussed. In the first part of the thesis, a seamless monolithic design was developed for flexible, lightweight, breathable and highly sensitive capacitive pressure senor. In the second part developed ionically conductive supramolecular gel was used as dielectric layer capacitive pressure sensor with carbon black based electrode and a record-breaking sensitivity was obtained. Addition to the conclusions of the presented works, with the following suggestions scope of the thesis may be extended.

In the first part of the thesis, resistance of the electrodes kept constant to 10 Ω sq^{-1}. It was also shown that increasing applied pressure on the sensor decreases resistivity of the electrodes. It is well known that capacitance of a capacitor is highly dependent on the resistance of the electrodes. Therefore, effect of the electrode resistance alteration on sensitivity should not be disregarded. However, in this case very low surface resistance of the electrodes made this contribution negligible. Therefore, a hybrid sensor design can further enhance sensitivity of the sensor. This hybrid design includes two main sensing units that work mutually and simultaneously. The first sensing unit is the electrodes with considerably high resistance. Under pressure resistance of the electrodes decreases and allow electrodes to carry more charges compared to the un-pressed condition. The second sensing unit changes its capacitance under pressure based on effective dielectric constant and dielectric thickness change. Therefore, the alteration of the capacitance of the whole unit based on both change in electrode resistance and dielectric property change. These combined effects should further enhance the sensitivity.

In the first part of the thesis, the capacitive pressure sensor was designed with a non-ionic conductive dielectric layer. In the literature, it is well-studied that using

ionically conductive dielectric layer increases sensitivity excessively. Therefore, instead of covering the sensor structure with a thin layer of PDMS, using a thin layer of ionic conductive polymer can further increase the sensitivity of the capacitive pressure sensor because of the EDL formation. Under this circumstances, effect of the electrode material on the sensitivity can be reconsidered. As it was done in the second part of the thesis, instead of using Al electrode, carbon-based electrodes enhance sensitivity. If carbon-based electrodes (or electrodes made of pseudocapacitive material) are used, similar behavior in sensitivity improvement can be expected for a seamless monolithic capacitive pressure sensor with an ionically conductive dielectric layer.

In the third part of the thesis, the effect of the electrode materials on the sensitivity was demonstrated. On this topic, there are limited number of articles are presented in the literature. Therefore, a comprehensive study of the effects of electrode materials on sensitivity could help to develop capacitive pressure sensors with higher sensitivity than their today's counterparts.

In the case of using pseudocapacitive electrode material for capacitive pressure sensors, measurement voltage of the sensor should be clarified. Pseudocapacitive effect depends on measurement voltage. Therefore, applying AC voltage with different amplitudes can change the snesitivity of the capacitive pressure sensors. Also, these systems should be tested under different frequencies in order to allow faradaic reactions to take place.

REFERENCES

1. Xu, F. *et al.* Recent developments for flexible pressure sensors: A review. *Micromachines* vol. 9 (2018).

2. Zang, Y., Zhang, F., Di, C. A. & Zhu, D. Advances of flexible pressure sensors toward artificial intelligence and health care applications. *Materials Horizons* vol. 2 140–156 (2015).

3. Vatani, M., Lu, Y., Engeberg, E. D. & Choi, J. W. Combined 3D printing technologies and material for fabrication of tactile sensors. *International Journal of Precision Engineering and Manufacturing* vol. 16 1375–1383 (2015).

4. Kim, K. H. *et al.* Wearable Resistive Pressure Sensor Based on Highly Flexible Carbon Composite Conductors with Irregular Surface Morphology. *ACS Appl. Mater. Interfaces* **9**, 17499–17507 (2017).

5. Lo, L. W. *et al.* Inkjet-Printed Soft Resistive Pressure Sensor Patch for Wearable Electronics Applications. *Advanced Materials Technologies* vol. 5 (2020).

6. Persano, L. *et al.* High performance piezoelectric devices based on aligned arrays of nanofibers of poly(vinylidenefluoride-co-trifluoroethylen. *Nature Communications* vol. 4 1610–1633 (2013).

7. Tan, Y. *et al.* High-performance textile piezoelectric pressure sensor with novel structural hierarchy based on ZnO nanorods array for wearable application. *Nano Research* vol. 14 3969–3976 (2021).

8. McCarty, L. S. & Whitesides, G. M. Electrostatic charging due to separation of ions at interfaces: Contact electrification of ionic electrets. *Angew. Chemie - Int. Ed.* **47**, 2188–2207 (2008).

9. Fan, F. R., Tian, Z. Q. & Lin Wang, Z. Flexible triboelectric generator. *Nano*

Energy **1**, 328–334 (2012).

10. Lee, K. Y. *et al.* Fully Packaged Self-Powered Triboelectric Pressure Sensor Using Hemispheres-Array. *Adv. Energy Mater.* **6**, 1–5 (2016).

11. Lei, H., Chen, Y., Gao, Z., Wen, Z. & Sun, X. Advances in self-powered triboelectric pressure sensors. *Journal of Materials Chemistry A* vol. 9 20100–20130 (2021).

12. Wang, Z. L. & Wang, A. C. On the origin of contact-electrification. *Mater. Today* **30**, 34–51 (2019).

13. Yang, P. *et al.* Monitoring the Degree of Comfort of Shoes In-Motion Using Triboelectric Pressure Sensors with an Ultrawide Detection Range. *ACS Nano* **16**, 4654–4665 (2022).

14. Lin, L. *et al.* Triboelectric active sensor array for self-powered static and dynamic pressure detection and tactile imaging. *ACS Nano* **7**, 8266–8274 (2013).

15. Shi, Q., Wang, H., Wang, T. & Lee, C. Self-powered liquid triboelectric microfluidic sensor for pressure sensing and finger motion monitoring applications. *Nano Energy* **30**, 450–459 (2016).

16. Garcia, C., Trendafilova, I., Guzman de Villoria, R. & Sanchez del Rio, J. Self-powered pressure sensor based on the triboelectric effect and its analysis using dynamic mechanical analysis. *Nano Energy* **50**, 401–409 (2018).

17. Fan, F. R. *et al.* Transparent Triboelectric Nanogenerators and Self-Powered.pdf. *Nano Letters* vol. 12 3109–3114 (2012).

18. Vivekananthan, V., Chandrasekhar, A., Alluri, N. R., Purusothaman, Y. & Kim, S. J. A highly reliable, impervious and sustainable triboelectric nanogenerator as a zero-power consuming active pressure sensor. *Nanoscale Advances* vol. 2 746–754 (2020).

19. Liu, Z., Zhao, Z., Zeng, X., Fu, X. & Hu, Y. Expandable microsphere-based triboelectric nanogenerators as ultrasensitive pressure sensors for respiratory and pulse monitoring. *Nano Energy* **59**, 295–301 (2019).

20. Zou, J. *et al.* Coupled Supercapacitor and Triboelectric Nanogenerator Boost Biomimetic Pressure Sensor. *Adv. Energy Mater.* **8**, (2018).

21. Pu, X. *et al.* Flexible triboelectric 3D touch pad with unit subdivision structure for effective XY positioning and pressure sensing. *Nano Energy* **76**, (2020).

22. Zhao, Z. *et al.* Machine-washable and breathable pressure sensors based on triboelectric nanogenerators enabled by textile technologies. *Nano Energy* **70**, (2020).

23. Bard, A. J. & Faulkner, R. L. *Electrochemical methods : fundamentals and applications*. *John Wiley & Sons, Inc* (2001). doi:10.1038/s41929-019-0277-8.

24. Helmholtz, H. Der phpsik und chemie. *Ann. der Phys. und Chemie* **7**, 22 (1879).

25. Kang, S. *et al.* Highly Sensitive Pressure Sensor Based on Bioinspired Porous Structure for Real-Time Tactile Sensing. *Adv. Electron. Mater.* **2**, (2016).

26. Kwon, D. *et al.* Highly Sensitive, Flexible, and Wearable Pressure Sensor Based on a Giant Piezocapacitive Effect of Three-Dimensional Microporous Elastomeric Dielectric Layer. *ACS Appl. Mater. Interfaces* **8**, 16922–16931 (2016).

27. Tay, R. Y. *et al.* Lightweight, Superelastic Boron Nitride/Polydimethylsiloxane Foam as Air Dielectric Substitute for Multifunctional Capacitive Sensor Applications. *Adv. Funct. Mater.* **30**, (2020).

28. Ruth, S. R. A., Feig, V. R., Tran, H. & Bao, Z. Microengineering Pressure Sensor Active Layers for Improved Performance. *Advanced Functional Materials* vol. 30 (2020).

29. Mishra, R. B., El-Atab, N., Hussain, A. M. & Hussain, M. M. Recent Progress on Flexible Capacitive Pressure Sensors: From Design and Materials to Applications. *Advanced Materials Technologies* vol. 6 (2021).

30. Niu, H. *et al.* Highly Morphology-Controllable and Highly Sensitive Capacitive Tactile Sensor Based on Epidermis-Dermis-Inspired Interlocked Asymmetric-Nanocone Arrays for Detection of Tiny Pressure. *Small* **16**, 1–12 (2020).

31. Yang, J. C. *et al.* Microstructured Porous Pyramid-Based Ultrahigh Sensitive Pressure Sensor Insensitive to Strain and Temperature. *ACS Applied Materials and Interfaces* vol. 11 19472–19480 (2019).

32. Baek, S. *et al.* Flexible piezocapacitive sensors based on wrinkled microstructures: Toward low-cost fabrication of pressure sensors over large areas. *RSC Adv.* **7**, 39420–39426 (2017).

33. Zeng, X. *et al.* Tunable, Ultrasensitive, and Flexible Pressure Sensors Based on Wrinkled Microstructures for Electronic Skins. *ACS Applied Materials and Interfaces* vol. 11 21218–21226 (2019).

34. Ma, L. *et al.* A highly sensitive and flexible capacitive pressure sensor based on a micro-arrayed polydimethylsiloxane dielectric layer. *Journal of Materials Chemistry C* vol. 6 13232–13240 (2018).

35. Chang, Y. *et al.* First Decade of Interfacial Iontronic Sensing: From Droplet Sensors to Artificial Skins. *Advanced Materials* vol. 33 (2021).

36. Pan, T., Nie, B., Xing, S. & Brandt, J. D. Droplet-Based Interfacial Capacitive Sensing. *Lab Chip* (2011).

37. Li, R. *et al.* Supercapacitive Iontronic Nanofabric Sensing. *Adv. Mater.* **29**,

(2017).

38. Liu, Q. *et al.* High-Porosity Foam-Based Iontronic Pressure Sensor with Superhigh Sensitivity of 9280 kPa−1. *Nano-Micro Letters* vol. 14 (2022).

39. Wan, Y. *et al.* A Highly Sensitive Flexible Capacitive Tactile Sensor with Sparse and High-Aspect-Ratio Microstructures. *Advanced Electronic Materials* vol. 4 (2018).

40. Wang, P., Li, G., Yu, W., Meng, C. & Guo, S. Flexible Pseudocapacitive Iontronic Tactile Sensor Based on Microsphere-Decorated Electrode and Microporous Polymer Electrolyte for Ultrasensitive Pressure Detection. *Advanced Electronic Materials* (2022) doi:10.1002/aelm.202101269.

41. Cui, J., Zhang, B., Duan, J., Guo, H. & Tang, J. Flexible pressure sensor with Ag wrinkled electrodes based on PDMS substrate. *Sensors (Switzerland)* vol. 16 (2016).

42. Joo, Y. *et al.* Silver nanowire-embedded PDMS with a multiscale structure for a highly sensitive and robust flexible pressure sensor. *Nanoscale* vol. 7 6208–6215 (2015).

43. Qiu, J. *et al.* Rapid-Response, Low Detection Limit, and High-Sensitivity Capacitive Flexible Tactile Sensor Based on Three-Dimensional Porous Dielectric Layer for Wearable Electronic Skin. *ACS Appl. Mater. Interfaces* **11**, 40716–40725 (2019).

44. Gao, L. *et al.* Highly Sensitive Pseudocapacitive Iontronic Pressure Sensor with Broad Sensing Range. *Nano-Micro Letters* vol. 13 (2021).

45. Yang, J. *et al.* Flexible, Tunable, and Ultrasensitive Capacitive Pressure Sensor with Microconformal Graphene Electrodes. *ACS Applied Materials and Interfaces* vol. 11 14997–15006 (2019).

46. Lin, Q. *et al.* Highly Sensitive Flexible Iontronic Pressure Sensor for Fingertip Pulse Monitoring. *Adv. Healthc. Mater.* **9**, 1–11 (2020).

47. Chen, R. *et al.* Blink-sensing glasses: A flexible iontronic sensing wearable for continuous blink monitoring. *iScience* **24**, 102399 (2021).

48. Xu, H. *et al.* Stretchable and anti-impact iontronic pressure sensor with an ultrabroad linear range for biophysical monitoring and deep learning-aided knee rehabilitation. *Microsystems Nanoeng.* **7**, (2021).

49. Kim, H. *et al.* Transparent, Flexible, Conformal Capacitive Pressure Sensors with Nanoparticles. *Small* **14**, 1–10 (2018).

50. Lu, P. *et al.* Iontronic pressure sensor with high sensitivity and linear response over a wide pressure range based on soft micropillared electrodes. *Sci. Bull.* **66**, 1091–1100 (2021).

51. Hua, Q. *et al.* Skin-inspired highly stretchable and conformable matrix networks for multifunctional sensing. *Nat. Commun.* **9**, 1–11 (2018).

52. Wan, C. *et al.* An Artificial Sensory Neuron with Tactile Perceptual Learning. *Adv. Mater.* **30**, 1–7 (2018).

53. Boutry, C. M. *et al.* A hierarchically patterned, bioinspired e-skin able to detect the direction of applied pressure for robotics. *Sci. Robot.* **3**, 1–10 (2018).

54. Kaltenbrunner, M. *et al.* An ultra-lightweight design for imperceptible plastic electronics. *Nature* **499**, 458–463 (2013).

55. Wang, S. *et al.* Skin electronics from scalable fabrication of an intrinsically stretchable transistor array. *Nature* **555**, 83–88 (2018).

56. Jin, T. *et al.* Ultrathin Nanofibrous Membranes Containing Insulating Microbeads for Highly Sensitive Flexible Pressure Sensors. *ACS Appl. Mater. Interfaces* (2020) doi:10.1021/acsami.0c00448.

57. Yokotaa, T. *et al.* Ultraflexible, large-area, physiological temperature sensors for multipoint measurements. *Proc. Natl. Acad. Sci. U. S. A.* **112**,

14533–14538 (2015).

58.   Niu, S. *et al.* A wireless body area sensor network based on stretchable passive tags. *Nat. Electron.* **2**, 361–368 (2019).

59.   Sundaram, S. *et al.* Learning the signatures of the human grasp using a scalable tactile glove. *Nature* **569**, 698–702 (2019).

60.   Mannsfeld, S. C. B. *et al.* Highly sensitive flexible pressure sensors with microstructured rubber dielectric layers. *Nat. Mater.* **9**, 859–864 (2010).

61.   Kim, Y. *et al.* A bioinspired flexible organic artificial afferent nerve. *Science (80-.).* **360**, 998–1003 (2018).

62.   Shuai, X. *et al.* Highly Sensitive Flexible Pressure Sensor Based on Silver Nanowires-Embedded Polydimethylsiloxane Electrode with Microarray Structure. *ACS Appl. Mater. Interfaces* **9**, 26314–26324 (2017).

63.   Atalay, O., Atalay, A., Gafford, J. & Walsh, C. A Highly Sensitive Capacitive-Based Soft Pressure Sensor Based on a Conductive Fabric and a Microporous Dielectric Layer. *Adv. Mater. Technol.* **3**, 1–8 (2018).

64.   Eom, J. *et al.* Highly sensitive textile-based strain sensors using poly(3,4-ethylenedioxythiophene):polystyrene sulfonate/silver nanowire-coated nylon threads with poly-l-lysine surface modification. *RSC Adv.* **7**, 53373–53378 (2017).

65.   Kulkarni, M. R. *et al.* Transparent Flexible Multifunctional Nanostructured Architectures for Non-optical Readout, Proximity, and Pressure Sensing. *ACS Appl. Mater. Interfaces* **9**, 15015–15021 (2017).

66.   Tien, N. T. *et al.* A flexible bimodal sensor array for simultaneous sensing of pressure and temperature. *Adv. Mater.* **26**, 796–804 (2014).

67.   Chen, Z. *et al.* Flexible Piezoelectric-Induced Pressure Sensors for Static Measurements Based on Nanowires/Graphene Heterostructures. *ACS Nano*

11, 4507–4513 (2017).

68. Kim, K. N. *et al.* Highly Stretchable 2D Fabrics for Wearable Triboelectric Nanogenerator under Harsh Environments. *ACS Nano* **9**, 6394–6400 (2015).

69. Shi, M. *et al.* Self-powered wireless smart patch for healthcare monitoring. *Nano Energy* **32**, 479–487 (2017).

70. Sun, J. G., Yang, T. N., Wang, C. Y. & Chen, L. J. A flexible transparent one-structure tribo-piezo-pyroelectric hybrid energy generator based on bio-inspired silver nanowires network for biomechanical energy harvesting and physiological monitoring. *Nano Energy* **48**, 383–390 (2018).

71. Zhang, L. *et al.* A self-protective, reproducible textile sensor with high performance towards human-machine interactions. *J. Mater. Chem. A* **7**, 26631–26640 (2019).

72. Zhou, J., Xu, X., Xin, Y. & Lubineau, G. Coaxial Thermoplastic Elastomer-Wrapped Carbon Nanotube Fibers for Deformable and Wearable Strain Sensors. *Adv. Funct. Mater.* **28**, 1–8 (2018).

73. Ma, Z. *et al.* Lightweight, compressible and electrically conductive polyurethane sponges coated with synergistic multiwalled carbon nanotubes and graphene for piezoresistive sensors. *Nanoscale* **10**, 7116–7126 (2018).

74. Shao, T. *et al.* Highly Sensitive Conformal Pressure Sensing Coatings Based on Thermally Expandable Microspheres. *Adv. Mater. Technol.* **2000032**, 1–8 (2020).

75. Li, T. *et al.* Flexible Capacitive Tactile Sensor Based on Micropatterned Dielectric Layer. *Small* **12**, 5042–5048 (2016).

76. Yang, J. *et al.* Ionic liquid–activated wearable electronics. *Mater. Today Phys.* **8**, 78–85 (2019).

77. Yang, X., Wang, Y. & Qing, X. Electrospun Ionic Nanofiber Membrane-

Based Fast and Highly Sensitive Capacitive Pressure Sensor. *IEEE Access* **7**, 139984–139993 (2019).

78.   Choi, D. *et al.* A Highly Sensitive Tactile Sensor Using a Pyramid-Plug Structure for Detecting Pressure, Shear Force, and Torsion. *Adv. Mater. Technol.* **4**, 1–10 (2019).

79.   Metzger, C. *et al.* Flexible-foam-based capacitive sensor arrays for object detection at low cost. *Appl. Phys. Lett.* **92**, 2006–2009 (2008).

80.   Vandeparre, H., Watson, D. & Lacour, S. P. Extremely robust and conformable capacitive pressure sensors based on flexible polyurethane foams and stretchable metallization. *Appl. Phys. Lett.* **103**, (2013).

81.   Tay, R. Y. *et al.* Lightweight, Superelastic Boron Nitride/Polydimethylsiloxane Foam as Air Dielectric Substitute for Multifunctional Capacitive Sensor Applications. *Adv. Funct. Mater.* **30**, 1–8 (2020).

82.   Carrera, E. Single- vs multilayer plate modelings on the basis of Reissner's mixed theorem. *AIAA J.* **38**, 342–352 (2000).

83.   Doganay, D., Coskun, S., Genlik, S. P. & Unalan, H. E. Silver nanowire decorated heatable textiles. *Nanotechnology* **27**, (2016).

84.   Coskun, S., Aksoy, B. & Unalan, H. E. Polyol synthesis of silver nanowires: An extensive parametric study. *Cryst. Growth Des.* **11**, 4963–4969 (2011).

85.   Carrera, E. *Theories and finite elements for multilayered, anisotropic, composite plates and shells*. *Archives of Computational Methods in Engineering* vol. 9 (2002).

86.   Thai, H. T. & Kim, S. E. A review of theories for the modeling and analysis of functionally graded plates and shells. *Compos. Struct.* **128**, 70 (2015).

87.   Chortos, A. & Bao, Z. Skin-inspired electronic devices. *Mater. Today* **17**,

321–331 (2014).

88. Peng, J. *et al.* Superhydrophobic Melamine Sponge Coated with Striped Polydimethylsiloxane by Thiol-Ene Click Reaction for Efficient Oil/Water Separation. *ACS Omega* **3**, 5222–5228 (2018).

89. Zhang, B. *et al.* Dual functional transparent film for proximity and pressure sensing. *Nano Research* vol. 7 1488–1496 (2014).

90. Grosse-Puppendahl, T. *et al.* Finding common ground: A survey of capacitive sensing in human-computer interaction. *Conference on Human Factors in Computing Systems - Proceedings* vols 2017-May 3293–3316 (2017).

91. Khalid, M. A. U. *et al.* A highly sensitive biodegradable pressure sensor based on nanofibrous dielectric. *Sensors Actuators, A Phys.* **294**, 140–147 (2019).

92. Huang, J. *et al.* A Dual-Mode Wearable Sensor Based on Bacterial Cellulose Reinforced Hydrogels for Highly Sensitive Strain/Pressure Sensing. *Adv. Electron. Mater.* **6**, 1–10 (2020).

93. Doganay, D. *et al.* Fabric based wearable triboelectric nanogenerators for human machine interface. *Nano Energy* **89**, 106412 (2021).

94. Cicek, M. O., Doganay, D., Durukan, M. B., Gorur, M. C. & Unalan, H. E. Seamless Monolithic Design for Foam Based, Flexible, Parallel Plate Capacitive Sensors. *Advanced Materials Technologies* vol. 6 (2021).

95. Pan, L. *et al.* An ultra-sensitive resistive pressure sensor based on hollow-sphere microstructure induced elasticity in conducting polymer film. *Nat. Commun.* **5**, 3002 (2014).

96. Li, R. *et al.* Supercapacitive Iontronic Nanofabric Sensing. *Adv. Mater.* **29**, 1700253 (2017).

97.   Durukan, M. B. *et al.* Multifunctional and Physically Transient Supercapacitors, Triboelectric Nanogenerators, and Capacitive Sensors. *Adv. Funct. Mater.* **2106066**, 2106066 (2021).

98.   Xiao, Y. *et al.* Multilayer Double-Sided Microstructured Flexible Iontronic Pressure Sensor with a Record-wide Linear Working Range. *ACS Sensors* **6**, 1785–1795 (2021).

99.   Bai, N. *et al.* Graded intrafillable architecture-based iontronic pressure sensor with ultra-broad-range high sensitivity. *Nature Communications* vol. 11 (2020).

100. Lu, P. *et al.* Iontronic pressure sensor with high sensitivity and linear response over a wide pressure range based on soft micropillared electrodes. *Science Bulletin* vol. 66 1091–1100 (2021).

101. Kim, J. S. *et al.* Enhanced Sensitivity of Iontronic Graphene Tactile Sensors Facilitated by Spreading of Ionic Liquid Pinned on Graphene Grid. *Advanced Functional Materials* vol. 30 (2020).

102. Niu, H. *et al.* Highly Morphology-Controllable and Highly Sensitive Capacitive Tactile Sensor Based on Epidermis-Dermis- Inspired Interlocked Asymmetric-Nanocone Arrays for Detection of Tiny Pressure. **1904774**, 1–12 (2020).

103. Sharma, S. *et al.* Hydrogen-Bond-Triggered Hybrid Nanofibrous Membrane-Based Wearable Pressure Sensor with Ultrahigh Sensitivity over a Broad Pressure Range. *ACS Nano* vol. 15 4380–4393 (2021).

104. Amoli, V. *et al.* A bioinspired hydrogen bond-triggered ultrasensitive ionic mechanoreceptor skin. *Nature Communications* vol. 10 (2019).

105. Nie, B., Xing, S., Brandt, J. D. & Pan, T. Droplet-based interfacial capacitive sensing. *Lab Chip* **12**, 1110 (2012).

106. Simon, P., Gogotsi, Y. & Dunn, B. and Supercapacitors Begin ? *Science (80-*

.). **343**, 1210–1211 (2014).

107. Béguin, F., Presser, V., Balducci, A. & Frackowiak, E. Carbons and electrolytes for advanced supercapacitors. *Adv. Mater.* **26**, 2219–2251 (2014).

108. Qin, G. *et al.* Multifunctional supramolecular gel polymer electrolyte for self-healable and cold-resistant supercapacitor. *J. Power Sources* **474**, 228602 (2020).

109. Shi, Y., Zhang, Y., Jia, L., Zhang, Q. & Xu, X. Stretchable and Self-Healing Integrated All-Gel-State Supercapacitors Enabled by a Notch-Insensitive Supramolecular Hydrogel Electrolyte. *ACS Appl. Mater. Interfaces* **10**, 36028–36036 (2018).

110. Guo, Y., Bae, J., Zhao, F. & Yu, G. Functional Hydrogels for Next-Generation Batteries and Supercapacitors. *Trends Chem.* **1**, 335–348 (2019).

111. Mackanic, D. G. *et al.* Decoupling of mechanical properties and ionic conductivity in supramolecular lithium ion conductors. *Nat. Commun.* **10**, 1–11 (2019).

112. Chivers, P. R. A. & Smith, D. K. Shaping and structuring supramolecular gels. *Nat. Rev. Mater.* **4**, 463–478 (2019).

113. Zhang, S., Wang, F., Peng, H., Yan, J. & Pan, G. Flexible Highly Sensitive Pressure Sensor Based on Ionic Liquid Gel Film. *ACS Omega* vol. 3 3014–3021 (2018).

114. Zhang, X. *et al.* Supramolecular nanofibrillar hydrogels as highly stretchable, elastic and sensitive ionic sensors. *Materials Horizons* vol. 6 326–333 (2019).

115. Khan, A., Kisannagar, R. R., Gouda, C., Gupta, D. & Lin, H. C. Highly stretchable supramolecular conductive self-healable gels for injectable adhesive and flexible sensor applications. *Journal of Materials Chemistry A*

vol. 8 19954–19964 (2020).

116. Liu, W., Lin, D., Sun, J., Zhou, G. & Cui, Y. Improved Lithium Ionic Conductivity in Composite Polymer Electrolytes with Oxide-Ion Conducting Nanowires. *ACS Nano* **10**, 11407–11413 (2016).

117. Qian, X. *et al.* Methods to study the ionic conductivity of polymeric electrolytes using a.c. impedance spectroscopy. *J. Solid State Electrochem.* **6**, 8–15 (2001).

118. Pradhan, D. K., Choudhary, R. N. P. & Samantaray, B. K. Studies of dielectric and electrical properties of plasticized polymer nanocomposite electrolytes. *Mater. Chem. Phys.* **115**, 557–561 (2009).

119. Wang, B., Li, S. & Wang, S. Correlation between the segmental motion and ionic conductivity of poly(ether urethane) complex studied by positron spectroscopy. *Phys. Rev. B - Condens. Matter Mater. Phys.* **56**, 11503–11507 (1997).

120. Köhler, M., Lunkenheimer, P. & Loidl, A. Dielectric and conductivity relaxation in mixtures of glycerol with LiCl. *Eur. Phys. J. E* **27**, 115–122 (2008).

121. Sequeira, C. A. C. & Hooper, A. The study of lithium electrode reversibility against (PEO)xLiF3CSO3 polymeric electrolytes. *Solid State Ionics* **9–10**, 1131–1138 (1983).

122. Mohanty, P. S. *et al.* Dielectric spectroscopy of ionic microgel suspensions. *Soft Matter* vol. 12 9705–9727 (2016).

123. Agrebi, F., Ghorbel, N., Ladhar, A., Bresson, S. & Kallel, A. Enhanced dielectric properties induced by loading cellulosic nanowhiskers in natural rubber: Modeling and analysis of electrode polarization. *Mater. Chem. Phys.* **200**, 155–163 (2017).

124. Pretsch, E., Bühlmann, P. & Badertscher, M. *Structure determination of*

organic compounds: Tables of spectral data. Structure Determination of Organic Compounds: Tables of Spectral Data (2009). doi:10.1007/978-3-540-93810-1.

125. Dumitriu, S. *Polysaccharides: Structural Diversity and Functional Versatility*.

126. Guo, Y. C., Cai, C. & Zhang, Y. H. Observation of conformational changes in ethylene glycol-water complexes by FTIR-ATR spectroscopy and computational studies. *AIP Adv.* **8**, 1–13 (2018).

127. Zhuang, J., Li, M., Pu, Y., Ragauskas, A. J. & Yoo, C. G. Observation of potential contaminants in processed biomass using fourier transform infrared spectroscopy. *Appl. Sci.* **10**, 1–13 (2020).

128. Ahmed, K. M., McLeod, M. P., Nézivar, J. & Giuliani, A. W. Fourier transform infrared and near-infrared spectroscopic methods for the detection of toxic Diethylene Glycol (DEG) contaminant in glycerin based cough syrup. *Spectroscopy* **24**, 601–608 (2010).

129. Remsing, R. C., Swatloski, R. P., Rogers, R. D. & Moyna, G. Mechanism of cellulose dissolution in the ionic liquid 1-n-butyl-3- methylimidazolium chloride: A 13C and 35/37Cl NMR relaxation study on model systems. *Chem. Commun.* 1271–1273 (2006) doi:10.1039/b600586c.

130. Lindman, B. *et al.* The relevance of structural features of cellulose and its interactions to dissolution, regeneration, gelation and plasticization phenomena. *Phys. Chem. Chem. Phys.* **19**, 23704–23718 (2017).

131. Zhang, J. *et al.* NMR spectroscopic studies of cellobiose solvation in EmimAc aimed to understand the dissolution mechanism of cellulose in ionic liquids. *Phys. Chem. Chem. Phys.* **12**, 1941 (2010).

132. Holten-Andersen, N. *et al.* pH-induced metal-ligand cross-links inspired by mussel yield self-healing polymer networks with near-covalent elastic

moduli. *Proc. Natl. Acad. Sci. U. S. A.* **108**, 2651–2655 (2011).

133.   Costanza, V. *et al.* Effect of glycerol on the mechanical and temperature-sensing properties of pectin films. *Appl. Phys. Lett.* **115**, (2019).

134.   Saminatha Kumaran, V. *et al.* The conductivity and dielectric studies of solid polymer electrolytes based on poly (acrylamide-co-acrylic acid) doped with sodium iodide. *Ionics (Kiel).* **24**, 1947–1953 (2018).

135.   Meng, G. & Ko, W. H. Modeling of circular diaphragm and spreadsheet solution programming for touch mode capacitive sensors. *Sensors and Actuators, A: Physical* vol. 75 45–52 (1999).

136.   Ko, W. H. & Wang, Q. Touch mode capacitive pressure sensors. *Sensors and Actuators, A: Physical* vol. 75 242–251 (1999).

APPENDICES

A. Supporting information for Chapter 2.
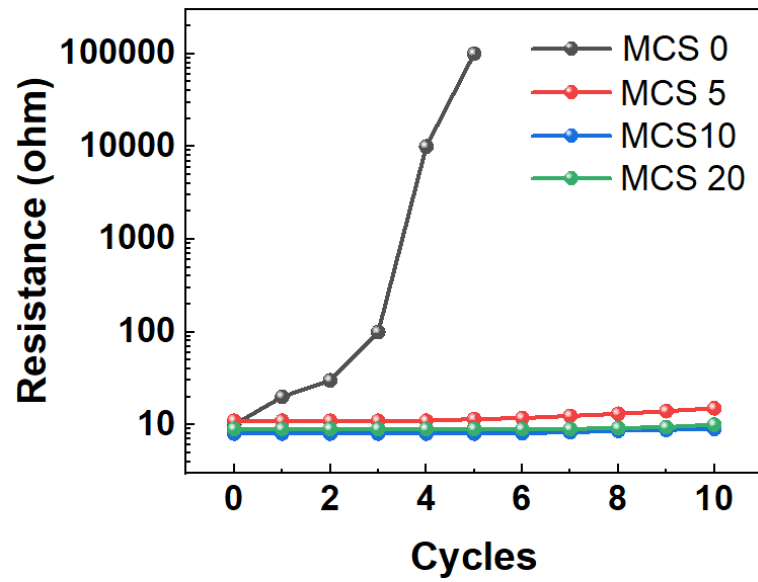
Figure A.1. Resistance changes of the MCSs after each washing cycles.

B. Supporting information for Chapter 3.
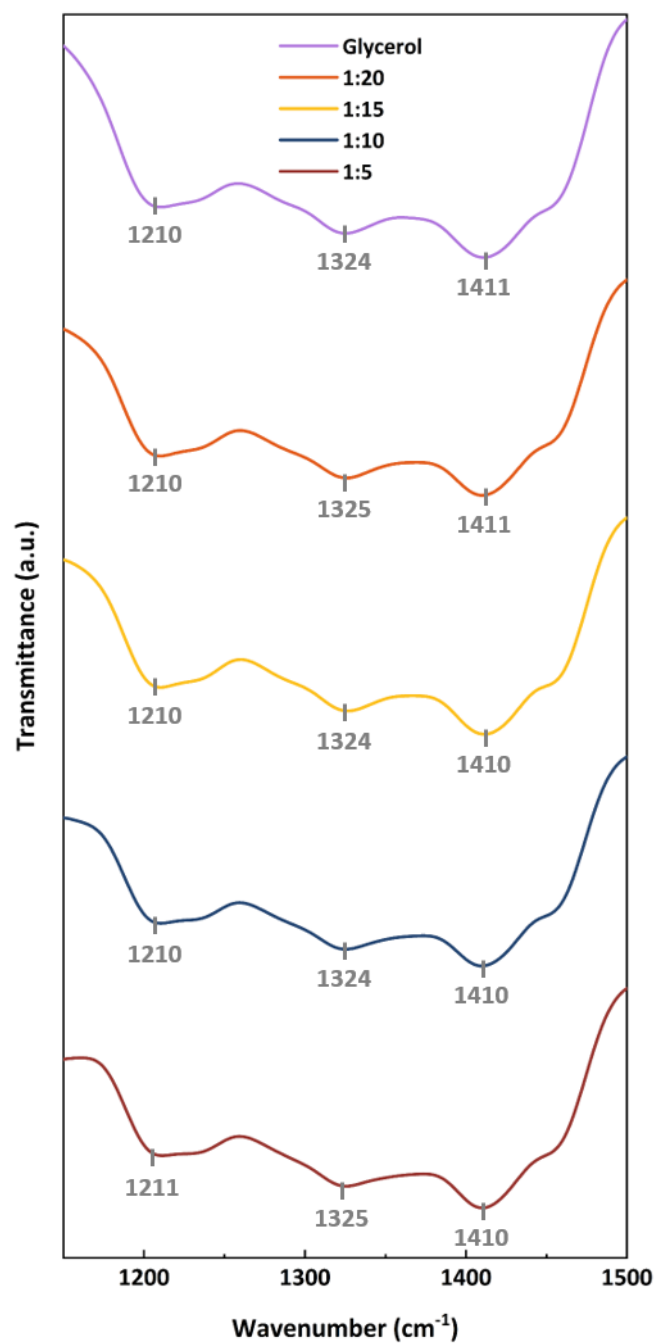
Figure B.1. FTIR spectra for glycerol and SBPG 1:5, 1:10, 1:15 and 1:20 within 1150-1500 cm-1.
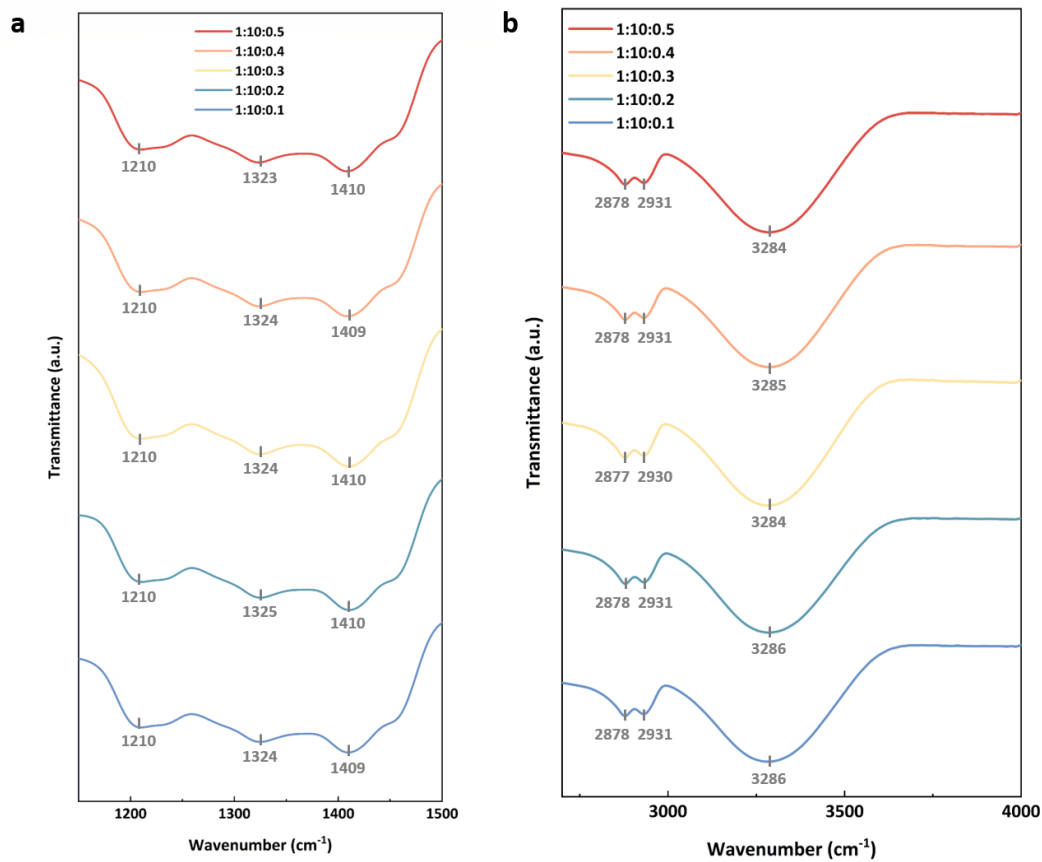
Figure B.2. FTIR spectra for SBPG 1:10:0.1, 1:10:0.2, 1:10:0.3, 1:10:0.4 and 1:10:0.5. Spectral range is a) 1150-1500 cm^{-1} and b) 2600-4000 cm^{-1}.
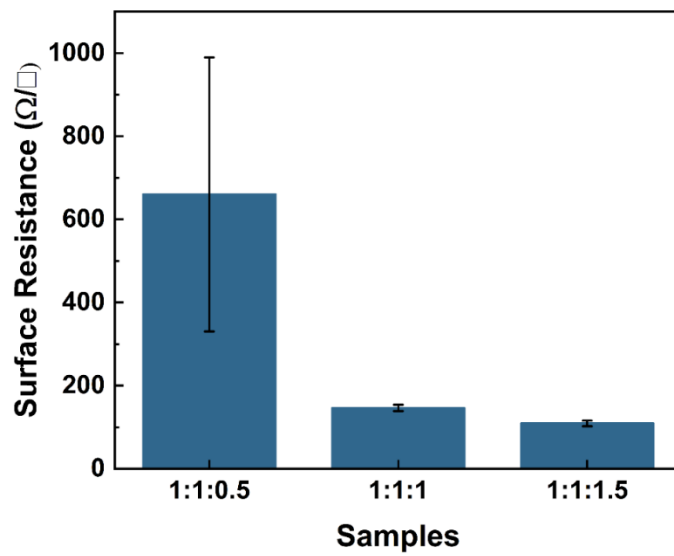
Figure B.3. Effect of carbon black ratio (HEC: glycerol: carbon black) on the surface resistance of the electrodes. Lowest surface resistance of 95 ± 4 Ω/sq is obtained with the 1:1:1.5 ratio.
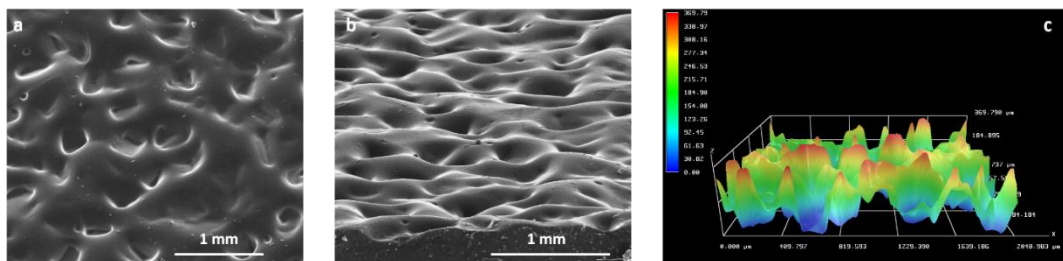
Figure B.4. SEM images of the patterned gel and its 3D morphology. a) Top and, b) angled-view SEM images of p-1:10:0.1. c) Topographical image of the p-1:10:0.1.

Table B.1. The hyperparameters and the accuracy values obtained for each type of classifier.

Classifier	Hyperparameters	Accuracy
Random Forest	Ensemble method: Bag Max Splits: 5 Max Learners: 35 # of Predictors to Sample: 4	90.4%
Decision Tree	Max # of Splits: 11 Split criterion: Twoing rule	90.2%
SVM	Kernel function: Gaussian Kernel scale: 11 Box constraint level: 1 Multiclass method: one-vs-one Standardization: True	89.9%
k-NN	# of Neighbors: 5 Distance metric: Spearman Distance weight: Squared Inverse Standardization: False	89.9%
Naïve Bayes	Distribution Names: Kernel Kernel type: Gaussian	89.1%
Discriminant Analysis	Discriminant type: Diagonal Quadratic	72.9%

Table B.2. True Positive Rates (TPR), False Negative Rates (FNR), Positive Predictive Values (PPV) and False Discovery Rates (FDR) values observed for each object for each classifier.

Classifier	Object	TPR	FNR	PPV	FDR
Decision Forest	Beaker	94.4%	5.6%	100.0%	0.0%
	Billiards Ball	100.0%	0.0%	97.9%	2.1%
	Bottle	38.1%	61.9%	40.0%	60.0%
	Cup	86.4%	13.6%	100.0%	0.0%
	Frizbee	100.0%	0.0%	90.6%	9.4%
	Pen	42.9%	57.1%	39.1%	60.9%
	PingPong Ball	100.0%	0.0%	88.9%	11.1%
	Plastic Ball	95.0%	5.0%	100.0%	0.0%
	Sponge	94.4%	5.6%	100.0%	0.0%
	Tape	95.7%	4.3%	97.8%	2.2%
	Tennis Ball	100.0%	0.0%	97.9%	2.1%
Decision Tree	Beaker	94.4%	5.6%	91.9%	8.1%
	Billiards Ball	100.0%	0.0%	95.8%	4.2%
	Bottle	76.2%	23.8%	48.5%	51.5%
	Cup	95.5%	4.5%	100.0%	0.0%
	Frizbee	93.1%	6.9%	90.0%	10.0%
	Pen	19.0%	81.0%	44.4%	55.6%
	PingPong Ball	93.8%	6.2%	93.8%	6.2%
	Plastic Ball	95.0%	5.0%	97.4%	2.6%
	Sponge	94.4%	5.6%	94.4%	5.6%
	Tape	95.7%	4.3%	95.7%	4.3%
	Tennis Ball	95.7%	4.3%	100.0%	0.0%
SVM	Beaker	97.2%	2.8%	100.0%	0.0%
	Billiards Ball	95.7%	4.3%	100.0%	0.0%
	Bottle	33.3%	66.7%	41.2%	58.8%
	Cup	90.9%	9.1%	100.0%	0.0%
	Frizbee	93.1%	6.9%	100.0%	0.0%
	Pen	47.6%	52.4%	45.5%	54.5%
	PingPong Ball	100.0%	0.0%	86.5%	13.5%
	Plastic Ball	97.5%	2.5%	97.5%	2.5%
	Sponge	97.2%	2.8%	85.4%	14.6%
	Tape	95.7%	4.3%	95.7%	4.3%
	Tennis Ball	95.7%	4.3%	95.7%	4.3%

k-NN	Beaker	94.4%	5.6%	100.0%	0.0%
	Billiards Ball	100.0%	0.0%	97.9%	2.1%
	Bottle	0.0%	100.0%	0.0%	100.0%
	Cup	90.9%	9.1%	100.0%	0.0%
	Frizbee	96.6%	3.4%	100.0%	0.0%
	Pen	85.7%	14.3%	43.9%	56.1%
	PingPong Ball	93.8%	6.2%	85.7%	14.3%
	Plastic Ball	97.5%	2.5%	90.7%	9.3%
	Sponge	97.2%	2.8%	100.0%	0.0%
	Tape	95.7%	4.3%	97.8%	2.2%
	Tennis Ball	93.5%	6.5%	100.0%	0.0%
Naïve Bayes	Beaker	97.2%	2.8%	100.0%	0.0%
	Billiards Ball	97.8%	2.2%	91.8%	8.2%
	Bottle	33.3%	66.7%	35.0%	65.0%
	Cup	90.9%	9.1%	100.0%	0.0%
	Frizbee	93.1%	6.9%	100.0%	0.0%
	Pen	38.1%	61.9%	36.4%	63.6%
	PingPong Ball	93.8%	6.2%	100.0%	0.0%
	Plastic Ball	100.0%	0.0%	100.0%	0.0%
	Sponge	97.2%	2.8%	87.5%	12.5%
	Tape	93.6%	6.4%	89.8%	10.2%
	Tennis Ball	95.7%	4.3%	100.0%	0.0%
Discriminant Analysis	Beaker	77.8%	22.2%	100.0%	0.0%
	Billiards Ball	0.0%	100.0%	0.0%	100.0%
	Bottle	19.0%	81.0%	25.0%	75.0%
	Cup	90.9%	9.1%	100.0%	0.0%
	Frizbee	93.1%	6.9%	93.1%	6.9%
	Pen	42.9%	57.1%	34.6%	65.4%
	PingPong Ball	90.6%	9.4%	100.0%	0.0%
	Plastic Ball	100.0%	0.0%	71.4%	28.6%
	Sponge	97.2%	2.8%	79.5%	20.5%
	Tape	95.7%	4.3%	90.0%	10.0%
	Tennis Ball	80.4%	19.6%	51.4%	48.6%

C. Permission Licence

Institution name	METU

Expected presentation date	Aug 2022

Order reference number	1

Requestor Location	METU

dumlupınar bulvarı, ODTÜ,

metalurji ve malzeme müh., D-308,

ankara, çankaya 06800

Turkey

Attn: METU

Publisher Tax ID	EU826007151

Total	0.00 USD

Terms and Conditions

license. The first instance of republication or reuse granted by this license must be completed within two years of the date of the grant of this license (although copies prepared before the end date may be distributed thereafter). The Wiley Materials shall not be used in any other manner or for any other purpose, beyond what is granted in the license. Permission is granted subject to an appropriate acknowledgement given to the author, title of the material/book/journal and the publisher. You shall also duplicate the copyright notice that appears in the Wiley publication in your use of the Wiley Material. Permission is also granted on the understanding that nowhere in the text is a previously published source acknowledged for all or part of this Wiley Material. Any third party content is expressly excluded from this permission.

• With respect to the Wiley Materials, all rights are reserved. Except as expressly granted by the terms of the license, no part of the Wiley Materials may be copied, modified, adapted (except for minor reformatting required by the new Publication), translated, reproduced, transferred or distributed, in any form or by any means, and no derivative works may be made based on the Wiley Materials without the prior permission of the respective copyright owner.For STM Signatory Publishers clearing permission under the terms of the STM Permissions Guidelines only, the terms of the license are extended to include subsequent editions and for editions in other languages, provided such editions are for the work as a whole in situ and does not involve the separate exploitation of the permitted figures or extracts, You may not alter, remove or suppress in any manner any copyright, trademark or other notices displayed by the Wiley Materials. You may not license, rent, sell, loan, lease, pledge, offer as security, transfer or assign the Wiley Materials on a stand-alone basis, or any of the rights granted to you hereunder to any other person.

• The Wiley Materials and all of the intellectual property rights therein shall at all times remain the exclusive property of John Wiley & Sons Inc, the Wiley Companies, or their respective licensors, and your interest therein is only that of having possession of and the right to reproduce the Wiley Materials pursuant to Section 2 herein during the continuance of this Agreement. You agree that you own no right, title or interest in or to the Wiley Materials or any of the intellectual property rights therein. You shall have no rights hereunder other than the license as provided for above in Section 2. No right, license or interest to any trademark, trade name, service mark or other branding ("Marks") of WILEY or its licensors is granted hereunder, and you agree that you shall not assert any such right, license or interest with respect thereto

• NEITHER WILEY NOR ITS LICENSORS MAKES ANY WARRANTY OR REPRESENTATION OF ANY KIND TO YOU OR ANY THIRD PARTY, EXPRESS, IMPLIED OR STATUTORY, WITH RESPECT TO THE

MATERIALS OR THE ACCURACY OF ANY INFORMATION CONTAINED IN THE MATERIALS, INCLUDING, WITHOUT LIMITATION, ANY IMPLIED WARRANTY OF MERCHANTABILITY, ACCURACY, SATISFACTORY QUALITY, FITNESS FOR A PARTICULAR PURPOSE, USABILITY, INTEGRATION OR NON-INFRINGEMENT AND ALL SUCH WARRANTIES ARE HEREBY EXCLUDED BY WILEY AND ITS LICENSORS AND WAIVED BY YOU.

• WILEY shall have the right to terminate this Agreement immediately upon breach of this Agreement by you.

• You shall indemnify, defend and hold harmless WILEY, its Licensors and their respective directors, officers, agents and employees, from and against any actual or threatened claims, demands, causes of action or proceedings arising from any breach of this Agreement by you.

• IN NO EVENT SHALL WILEY OR ITS LICENSORS BE LIABLE TO YOU OR ANY OTHER PARTY OR ANY OTHER PERSON OR ENTITY FOR ANY SPECIAL, CONSEQUENTIAL, INCIDENTAL, INDIRECT, EXEMPLARY OR PUNITIVE DAMAGES, HOWEVER CAUSED, ARISING OUT OF OR IN CONNECTION WITH THE DOWNLOADING, PROVISIONING, VIEWING OR USE OF THE MATERIALS REGARDLESS OF THE FORM OF ACTION, WHETHER FOR BREACH OF CONTRACT, BREACH OF WARRANTY, TORT, NEGLIGENCE, INFRINGEMENT OR OTHERWISE (INCLUDING, WITHOUT LIMITATION, DAMAGES BASED ON LOSS OF PROFITS, DATA, FILES, USE, BUSINESS OPPORTUNITY OR CLAIMS OF THIRD PARTIES), AND WHETHER OR NOT THE PARTY HAS BEEN ADVISED OF THE POSSIBILITY OF SUCH DAMAGES. THIS LIMITATION SHALL APPLY NOTWITHSTANDING ANY FAILURE OF ESSENTIAL PURPOSE OF ANY LIMITED REMEDY PROVIDED HEREIN.

• Should any provision of this Agreement be held by a court of competent jurisdiction to be illegal, invalid, or unenforceable, that provision shall be deemed amended to achieve as nearly as possible the same economic effect as the original provision, and the legality, validity and enforceability of the remaining provisions of this Agreement shall not be affected or impaired thereby.

• The failure of either party to enforce any term or condition of this Agreement shall not constitute a waiver of either party's right to enforce each and every term and condition of this Agreement. No breach under this agreement shall be deemed waived or excused by either party unless such waiver or consent is in writing signed by the party granting such waiver or consent. The waiver by or consent of a party to a breach of any provision of this Agreement shall not operate or be construed as a waiver of or consent to any other or subsequent breach by such other party.

• This Agreement may not be assigned (including by operation of law or otherwise) by you without WILEY's prior written consent.

• Any fee required for this permission shall be non-refundable after thirty (30) days from receipt by the CCC.

• These terms and conditions together with CCC's Billing and Payment terms and conditions (which are incorporated herein) form the entire agreement between you and WILEY concerning this licensing transaction and (in the absence of fraud) supersedes all prior agreements and representations of the parties, oral or written. This Agreement may not be amended except in writing signed by both parties. This Agreement shall be binding upon and inure to the benefit of the parties' successors, legal representatives, and authorized assigns.

• In the event of any conflict between your obligations established by these terms and conditions and those established by CCC's Billing and Payment terms and conditions, these terms and conditions shall prevail.

• WILEY expressly reserves all rights not specifically granted in the combination of (i) the license details provided by you and accepted in the course of this licensing transaction, (ii) these terms and conditions and (iii) CCC's Billing and Payment terms and conditions.

• This Agreement will be void if the Type of Use, Format, Circulation, or Requestor Type was misrepresented during the licensing process.

• This Agreement shall be governed by and construed in accordance with the laws of the State of New York, USA, without regards to such state's conflict of law rules. Any legal action, suit or proceeding arising out of or relating to these Terms and Conditions or the breach thereof shall be instituted in a court of competent jurisdiction in New York County in the State of New York in the United States of America and each party hereby consents and submits to the personal jurisdiction of such court, waives any objection to venue in such court and consents to service of process by registered or certified mail, return receipt requested, at the last known address of such party.

WILEY OPEN ACCESS TERMS AND CONDITIONS

Wiley Publishes Open Access Articles in fully Open Access Journals and in Subscription journals offering Online Open. Although most of the fully Open Access journals publish open access articles under the terms of the Creative Commons Attribution (CC BY) License only, the subscription journals and a few of the Open Access Journals offer a choice of Creative Commons Licenses. The license type is clearly identified on the article.

The Creative Commons Attribution License

108